An Investigation of Hydrogen Impacts on the Ductile-Brittle Transition by
Nanoindentation

A DISSERTATION
SUBMITTED TO THE FACULTY OF
UNIVERSITY OF MINNESOTA
BY

Claire Stafford Morgan

IN PARTIAL FULFILLMENT OF THE REQUIREMENTS
FOR THE DEGREE OF
DOCTOR OF PHILOSOPHY

Advisers: W.W. Gerberich and K.A. Mkhoyan

September 2017

Acknowledgements

Special thanks to my advisers, Bill Gerberich and Andre Mkhoyan. Bill's guidance and knowledge was invaluable throughout this process. I am lucky to be his last graduate student in such a well-respected career. Andre ignited my interest in research as an undergraduate and was also a great support throughout graduate school.

Thanks to my family who has been supportive for the emotional aspects of graduate school, especially my mom and dad, Carolyn and Gym Teresi. My surrogate parents, Amy Stafford and Marc Skaug have also been excellent supporters. To my Grammy, thank you for making education so important in your life, your children's lives, and your grandchildren's lives. You are why I am here.

Thanks to all the people at Clemson University who inspired me to become a Materials Science major, particularly Molly Kennedy who helped me through unimaginable hurdles and kept me in school and to my classmates. Go Tigers!

There are a multitude of people to give thanks to in my groups throughout my career at the University of Minnesota. First, to Eric Hintsala, who taught me how to use a nanoindenter and helped so much with the ins and outs of research, graduate school, and all the snags along the way. Eric also helped significantly with much of the work presented in this thesis. Andrew Wagner, who helped with hydrogen charging, and moving labs. Anudha 'Millie' Mittal, who was my first research mentor and a big part of me coming back to the University of Minnesota. Mike Lund, who also taught me a lot about research and some of the tricky techniques to help collect experimental results. Ryan Wu and Prashant Kumar, both amazing scientists which I had the pleasure of starting graduate school with, who helped with experiments, making presentations and talks better, and most of all made the office enjoyable. Jake Held, who fixed the triboindenter with a little soldering genius and was a constant help and conversationalist. Hwanhui Yun, my lab sister and friend, who helped me learn English better. To Michael Odlyzko and Danielle Hickey – wonderful people with patience and knowledge to keep pushing others towards success.

To the graduate school at the University of Minnesota – Russ Holmes has been a great Director of Graduate Studies as questions have arisen and even stepped up to the challenge of being a minister for my marriage. Thanks to Julie Prince and Teresa Bredahl for making sure that things get done. To the rest of my class – a wonderful set of people that have been a joy to get to know and a joy to continue to know in the future. The support we have given one another is something none of us will forget. To the rest of the graduate students – you know who you are, thank you for everything.

To the staff at the Characterization Facility and the Minnesota Nano Center, particularly Nick Seaton and Kevin Roberts, thank you for teaching people how to use the instruments necessary for so many students.

Dedication

To Nathan Morgan, who beat me to the chase, again

To my family, the best teachers for getting worthwhile things done

Abstract

Understanding mechanical properties is essential for material reliability in almost all industrial applications. While materials have been mechanically investigated and standards exist at the bulk scale, this is not the case when relevant material dimensions change to the order of microns to nanometers. The material property trends observed at the bulk scale do not necessarily apply at the small-scale. As industries and laboratories develop products with small components, the need for small scale testing and property mapping has increased drastically.

Throughout this work, the impact of hydrogen on the mechanical properties was investigated in three systems: Sc, Si, and Ni. First, Sc films were deuterium charged and the resulting scandium deuteride (ScD_2) films, used in applications for neutron generation, are examined. Fracture, elastic, and plastic properties are defined for films and micropillars milled into the films. Size, impurity, and substrate effects are discussed. The subsequent sections examine the mechanical properties and dislocation dynamics of single crystal Ni and Si specimens. Hardness, elastic modulus, fracture toughness, and activation volumes for dislocation motion are determined and discussed for samples with and without thermal gas-hydrogen charging. Hydrogen is shown to decrease fracture toughness as well as effect stresses and activation volumes measured in strain rate jump tests, particularly in Si samples. Together, these results indicate hydrogen charging causes a decrease in dislocation velocity, supporting a hydrogen enhanced decohesion mechanism in Si at this small scale.

Table of Contents

List of Tables

List of Figures

List of Common Abbreviations and Acronyms

DBT	Ductile Brittle Transition
EBSD	Electron BackScatter Diffraction
FIB	Focused Ion Beam
Ga	Gallium
HEDE	Hydrogen Enhanced DEcohesion
HELP	Hydrogen Enhanced Local Plasticity
MEMS	MicroElectroMechanical Systems
Mo	Molybdenum
Ni	Nickel
REDG	Radiation Enhanced Dislocation Glide
Sc	Scandium
ScD_2	Scandium Deuteride
SEM	Scanning Transmission Microscopy
Si	Silicon
SPM	Scanning Probe Microscopy
TEM	Transmission Electron Microscopy
UMN	University of Minnesota
XRD	X-Ray Diffraction

List of Common Symbols with Common Units

A	Area (m^2)
b	Burgers Vector (nm)
E	Youngs Modulus (GPa)
F	Force (Pa)
G	Strain Energy Release Rate (J/m^2)
H	Hardness (GPa)
h	Contact Depth (nm)
H_0	Activation Energy (J)
K	Fracture Toughness ($MPa \cdot m^{1/2}$)
k	Boltzmann Constant, $1.38*10^{-23}$ J/K
l	Length (m)
P	Load (N)
Q	Latent heat of formation (J)
T	Temperature (K or °C)
V*	Apparent Activation Volume (m^3)
ε	Strain (m/m)
Ө	Angle (°)
μ	Shear Modulus (GPa)
σ	Stress (Pa)
υ	Velocity (m/s) or Poissons Ratio (m/m)
τ*	Effective Shear Stress (GPa)

Chapter 1 : Introduction

Engineering design is essential to reliable products in every industry. Materials science and engineering is particularly significant when considering the design of materials, and can be visualized through a common tetrahedron where materials structure, processing, properties, and performance are all directly linked, as shown in Figure 1.1. This highlights that to fully understand the behavior of a material, one must understand the entire system responsible for manufacturing, characterizing and using the material. This is not always straightforward and the complexities of these systems will feed research interests seemingly indefinitely.
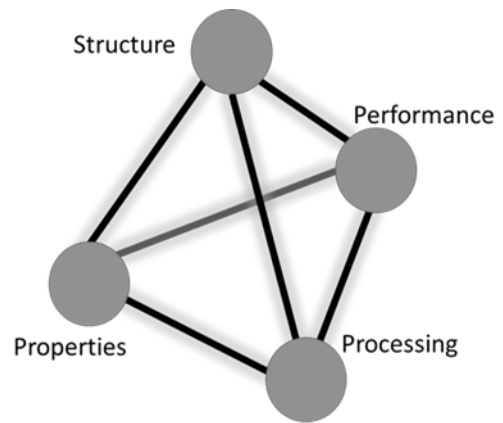
Figure 1.1: Materials science tetrahedron. Adapted from Reference **[254]**.

With technology constantly improving, materials processing is also drastically changing – where relevant size parameters for materials in electronic devices and microelectromechanical systems (MEMS) are changing from length scales on the order of millimeters to microns and nanometers. As the size of the materials gets this small, or in other words as the processing of the material changes, the properties are also affected, particularly considering mechanical responses. Mechanical behavior is the study of how a material responds to stress, and is essential to understand and predict the deformation, fracture, and more generally how the stress state of a material affects these properties. Without properly defining these parameters, the reliability of the components under stress

is in question. This is why mechanical properties have been studied extensively at the large, bulk scale for hundreds of years. As a result, there are extensive lists of testing standards so the mechanical behavior of bulk materials can be determined and accurately compared. Additionally, there are a variety of mechanism maps that predict mechanical behavior that are particularly helpful for material selection for a given application. These include Ashby plots [1], which help predict material performance by directly comparing multiple materials by plotting two material properties, such as Young's modulus versus density, and mechanism maps [2, 3], which predict how a material will deform or fracture at a given stress and temperature.

The Ashby plot is also the basis of a 3D plot that could be used to predict the behavior of material, though, these plots only consider bulk-scale materials. However, with the addition of a size parameter, described in Chapter 2, this could be a useful engineering tool for small-scale components, as new phenomena are being observed that cannot be explained with the current understanding of bulk materials [4]. These new mechanical phenomena and trends are being observed and quantified thanks to developments in instrumentation. The technology to fabricate, test, and observe small-scale volumes is new relative to the mechanical properties field with most advances occurring within the past 50 years. Now, atoms can be directly observed during testing, an insightful development that enables researchers to isolate, characterize, and explain behavior that could only be theoretically modeled before.

As the science of studying small scale volumes of material is becoming more widespread, understanding is rapidly advancing. However, research is still needed, and the

applications for this research extend beyond the hunger for knowledge and basic science investigations. Manufacturers that are fabricating small scale device components have an innate need to predict the behavior of these products to ensure reliability. For example, several industries and laboratories have and continue to develop MEMS, microelectronics, protective coatings, and thin film devices that have components with sub-micron dimensions and the applicable list is growing [5, 6, 7, 8, 9]. In the past, studies of small volumes have proven essential to solving industrial problems, particularly in thin film and micromechanical structure adhesion applications [10, 11]. This work can be applied to help solve or understand plasticity and fracture at this scale for other applications.

This work will focus on understanding the mechanical properties of materials at small scales as well as alterations in the processing of those materials to determine how properties and performance are impacted. Three materials will be studied: Sc, Si, and Ni. Together, these materials represent relatively ductile metals and brittle semiconductors, though the addition of hydrogen to the two metal systems enables the study of hydrides in the case of ScD_2 and interstitially diffused hydrogen effects in Ni. While the work here is material specific, the observed phenomena can apply to other material systems. The work can also be used to begin the mapping of mechanical behavior at small scales as is done in Chapter 2, where the explanation for the ductile-brittle transition (DBT) in Si is given and the relevant parameters to measure these transitions are discussed. This chapter also gives the background material necessary to understand much of the terminology and methods behind the experiments and analysis used here. This begins with an explanation of mechanical behavior, crystal structures, and dislocations and ends with the description of

3

the instrumentation and methods of experimentation for the research performed. Once a background is provided, Chapter 3 delves into the properties of ScD_2 films. First, Sc films are produced, then deuterium charged. This process not only changes the structure of the films into a hydride structure, but also causes fracture in the films, prompting this extensive mechanical property investigation. Fracture, plasticity, and elastic parameters of the deuteride films are calculated and a size effect, relevant to micropillar diameter, is determined. These values are pertinent to modelling efforts by others to understand, predict, and improve production to increase reliability of the films for neutron generation applications.

Chapter 4 is a description of single crystal Si and Ni. First, activation parameters associated with dislocation motion are defined. Then, the material is hydrogen charged and activation parameters are measured again to determine hydrogen effects. New phenomena observed in nanoindentation and micropillar compression are shown and discussed. Lastly, Chapters 5 and 6 summarize, conclude, and present future directions for the work in this dissertation.

Chapter 2 Background:

Mechanical properties describe the response of a material to a force or applied load. Defining these properties is essential for the design of mechanically reliable materials. In order to measure these properties, materials are tested systematically, usually with a known, controlled force and the responses are measured. Typical forces are applied in tension, compression, or shear, where samples are pulled or pushed in the perpendicular direction or force is placed parallel to a surface, respectively [12, 13]. The relevant parameters of interest for most mechanical testing are stresses and strains.

2.1 Stress and Strain

Stresses are dependent on force as well as a geometry over which the force is applied. Engineering stresses are defined by [13]:

$$\sigma = \frac{F}{A_0},$$
2.1

where A_0 is an initial area, and F is the instantaneous applied force. Stresses are typically reported in values of megapascals (MPa) or pounds per square inch. Strain is a unit-less value that relates to geometry changes in a specimen due to an applied stress. Engineering strain values are given by [13]:

$$\varepsilon = \frac{l_i - l_0}{l_0},$$
2.2

where l_0 is an initial length, and l_i is the instantaneous change in length as a force is applied. Since many mechanical tests result in nonuniform permanent deformation such as necking in tension testing or barreling in compression testing, the stresses can be measured using true stresses and strains where the forces and geometry changes are incrementally

determined throughout testing. The values of stress and strain in this case are called true values. True strain is the natural logarithm of unity plus engineering strain, and true stress and strain can be related to engineering stress and strain through some simple conversions, assuming that the material volume does not change during testing.

The basic mechanical property information that can be determined from a standard tensile stress-strain curve of a bulk material is the elastic modulus, yield strength, and toughness. The elastic modulus, E, can be determined from the initial, linear, reversible portion of a stress strain curve. This property is indicative of how strong the atomic bonds in a material are relative to other materials. The elastic modulus values for metals and ceramics are typically very high while modulus values for polymers are typically lower. The yield strength, σ_y, is the stress at which permanent, plastic deformation occurs. Usually, this is defined by the intersection of the stress-strain data with a line parallel to the elastic portion of the curve with 0.2% strain offset. The toughness of a material is the amount of energy a material can withstand before fracture – this is defined by the area underneath a stress strain curve. Typically, the toughness values for metals is much higher than ceramics, which tend to fracture shortly after yield.

Additional material property data that can be easily collected from a tension test are fracture strength as well as Poisson's ratio. Fracture strength is determined from the final stress a material can withstand before failure. Poisson's ratio, υ, can also be determined through a stress-strain experiment as long as the dimensions of the material are known in all directions throughout the test. This property is defined by the negative of the change in

strain in a transverse direction divided by the strain in the normal direction of the force applied or [13]:

$$v = -\frac{d\varepsilon_x}{d\varepsilon_z} = -\frac{d\varepsilon_y}{d\varepsilon_z}. \qquad\qquad 2.3$$

Most of the aforementioned mechanical properties above are orientation-dependent. In other words, differently oriented single crystals will have different mechanical properties. Most of the materials manufactured are polycrystalline, or have multiple grains with varied orientation and bulk mechanical properties are impacted by grain size and orientation [13]. This means that bulk scale properties are typically a large average of properties from grains of varying size and orientation; however, at the small scale where only one to a few grains are investigated, the properties can change drastically based on the crystal orientation of the material investigated.

2.2 Crystalline Materials

The materials that are discussed throughout this work are crystalline. This means that the atoms that make up these materials are periodically bonded with long and short range order, meaning that the local bonding of the atoms are known and that this order repeats by translational periodicity. The order of these atoms can be defined by a lattice and a basis, where a lattice is an imaginary three-dimensional periodic spacing of points, and a basis is the repeating unit of the crystal structure that is placed in lattice points. There are seven distinct crystal systems that are typically described with unit cells, or the smallest repeating unit that can be propagated to form a crystal that reflects the symmetry of the crystal system. In this work, discussions will focus on cubic and hexagonal crystal systems.

7

Crystallographic directions are defined by integer vectors that describe the magnitude and direction between two points in a crystal system. This direction is denoted by three terms enclosed in square brackets with negative indices represented by bars over the respective axes projection, i.e. [100] or [32$\bar{1}$]. If a crystal system has symmetry, some directions will be geometrically equivalent and will be grouped into family of directions in angle brackets. The orientations of crystal planes are described using Miller-Bravais indices enclosed by parentheses, where parallel planes will have equivalent indices, i.e. (110) or (11$\bar{2}$1). Hexagonal crystal systems have a four-index designation, but all other crystal systems use a coordinate system with three-indices. Depending on the crystal system, there can be geometrically equivalent planes which are described using respective indices enclosed by braces.

Crystalline structures can be investigated for lattice spacing in a variety of ways, but the primary way is by x-ray diffraction (XRD). In this instrument, an x-ray beam is directed at a crystal, and by tilting the beam in various incident angles with the sample, a diffraction pattern forms. The diffraction of the x-ray beam in a coherent manner relative to diffraction patterns is a result of Bragg's law [13]:

$$n\lambda = 2dsin\theta \hspace{4cm} 2.4$$

In Bragg's law, *n* is a positive integer, λ is the wavelength of the x-ray, *d* is the lattice interplanar spacing, and θ is the scattering angle. If the conditions for Bragg's law are not met, then the x-ray will incoherently scatter off the crystal lattice. Resulting diffraction patterns provide intensity versus diffraction angle plots that are characterized to determine crystal structure. XRD is generally used as a global analysis technique, and though grain

8

texture analysis is generally effective with XRD, spatial resolution is poor due to the beam size in a typical instrument [14]. In the experiments listed here, it is essential to have site specific orientation information about the materials study to properly analyze mechanical responses. Now that crystalline materials and the techniques used to characterize them have been described, the deformation of crystals can be discussed.

2.3 Crystal Strength and Defects

If a crystalline material has a perfect lattice, the theoretical yield strength of the material can be estimated from the shear modulus, μ, a material dependent property that describes the elastic response of a material by the change in strain over change in stress due to a shear stress. The stress for a material to move from one lattice point to another is theoretically modelled as about $\mu/30$ by carefully determining the elastic deformation limit of a perfectly ordered material [15]. However, all materials yield and deform at much lower stresses, usually by a difference of several orders of magnitude, than theoretically predicted [15, 13]. This discrepancy is known to be a result of preexisting defects called dislocations that require lower stresses to move in a crystal than the corresponding perfect lattice. Initially, the concept of a dislocation, a specific type of crystal imperfection, was published by Tempe in 1905 [16], but three scientists simultaneously reported that these dislocations are the likely cause of most plastic material deformation at lower stresses [17, 18, 19]. G.I. Taylor is given the credit for solidifying the idea of a dislocation in 1934 [19], and since then dislocations have been the focus of many mechanical property studies.

Crystalline materials have four categories of defects: point, line, and planar defects. Point defects are the smallest type of defect – where an individual atom is either vacant,

added, or altered in a crystal lattice. Line defects, or dislocations, are groups of atoms out of place relative to the periodic structure. Planar defects are the larger scale defects where typically two volumes of material meet, including grain boundaries, external surfaces, twin boundaries, and stacking faults. Lastly, bulk defects can be thought of as the macroscopic coalescence of smaller defects and include things such as precipitates, voids, and cracks [20].

2.4 Dislocations
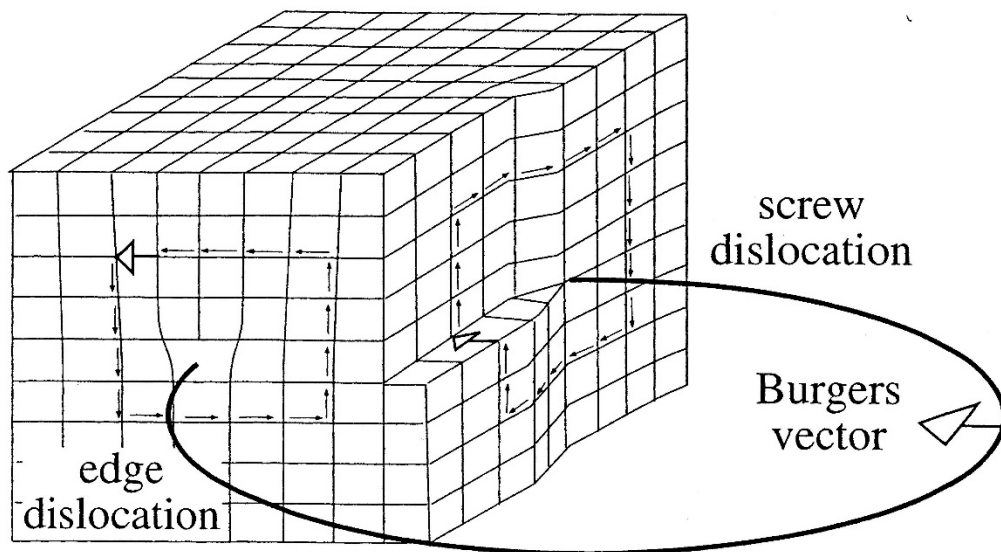
Figure 2.1: A mixed dislocation where the circle drawn is the dislocation line. Surfaces of the crystal shown are the pure edge and pure screw components of the mixed dislocation. Taken from Reference **[255]**.

While all defects will impact the mechanical properties of a material, dislocations are the most important in the majority of circumstances because they act as carriers of plastic deformation throughout a material [15]. However, other defects play a role with the motion, pinning, and multiplication of dislocations as dislocations become activated thermally or mechanically. Dislocations are defined by their line direction and the Burgers vector. A line direction runs along the dislocation core, the area where the crystal is most

distorted, and the Burgers vector, *b*. This vector is heavily dependent on crystal structure, and represents the magnitude and direction of the lattice distortion.

There are three main types of dislocations: edge, screw, and mixed. The distortion in the crystal for pure edge and screw dislocations can be seen on the side surfaces of Figure 2.1. The dark circle drawn in this figure represents the line direction of the dislocation and is denoted by the three unfilled arrows on the diagram. It is also important to notice that a mixed dislocation on a single slip plane will have a variety of line directions, but the Burgers vector will remain constant, also apparent in Figure 2.1. Edge dislocations are simply described as an extra half plane of atoms inserted into a crystal structure where the line direction and Burgers vector are perpendicular. Screw dislocations have line directions and Burgers vectors that are parallel, but these dislocations are more difficult to describe. Screw dislocations can be visualized from a perfect three-dimensional lattice that is distorted by a shear stress moves half of plane of atoms by one unit cell in one direction. Mixed dislocations are the more prevalent type of dislocation and have both screw and edge character where the Burgers vector varies in relation to the dislocation line. Each has different mobility through a crystal lattice depending on structure, atom types in the structure, temperature, dislocation density, other defects, etc.

Dislocations also define the displacement of atoms through dislocation motion. However, it is possible that a dislocation can dissociate into partial dislocations if this is energetically favorable. This is only the case when $b_{perfect}^2 > b_{partial\_1}^2 + b_{partial\_2}^2$ [20]. These reactions take place in many materials, for example, partial dislocations are the primary dislocations in nanoindentation experiments of silicon [21].

Although dislocations require less energy to distort a crystal lattice than a dislocation-free equivalent crystal, the energy barrier associated with dislocation formation must be discussed. This barrier exists due to the atomic bonds that must be broken to form a dislocation and the resulting stress field that a dislocation generates. The stresses of a stationary edge dislocation are given by Equations 2.5 a-e [15]:

$$\sigma_{xx} = \frac{\mu b}{2\pi(1-v)} \frac{y(3x^2+y^2)}{(x^2+y^2)^2}, \qquad \text{2.5 a}$$

$$\sigma_{yy} = \frac{\mu b}{2\pi(1-v)} \frac{y(x^2-y^2)}{(x^2+y^2)^2}, \qquad \text{2.5 b}$$

$$\sigma_{zz} = v(\sigma_{xx}+\sigma_{yy}), \qquad \text{2.5 c}$$

$$\sigma_{xx} = \frac{\mu b}{2\pi(1-v)} \frac{x(x^2-y^2)}{(x^2+y^2)^2}, \qquad \text{2.5 d}$$

$$\text{and } \sigma_{xz} = \sigma_{yz} = 0. \qquad \text{2.5 e}$$

Stresses of a stationary screw dislocation are given by Equations 2.6 a-c [15]:

$$\sigma_{xz} = \frac{\mu b}{2\pi} \frac{y}{x^2+y^2}, \qquad \text{2.6 a}$$

$$\sigma_{yz} = \frac{\mu b}{2\pi} \frac{x}{x^2+y^2}, \qquad \text{2.6 b}$$

$$\text{and } \sigma_{xx} = \sigma_{yy} = \sigma_{zz} = \sigma_{xy} = 0. \qquad \text{2.6 c}$$

In the two sets of above equations, the subscripts of the stresses given indicate what surface a stress is acting upon. The elastic stress field of a dislocation is strongest at the dislocation core and these equations do not apply as the distortions are larger than what can be

predicted through elastic theory. All dislocation stresses decrease radially away from the dislocation core.

The stress fields of dislocations result in a variety of interactions as they move throughout a material. Dislocations are attracted by free surfaces where dislocations can be eliminated, as image forces of a dislocation can remove dislocations from near-surface areas in a homogeneous material [15, 20]. This occurs because the dislocation self-energy decreases at surfaces where materials are relatively more compliant than in the internal bulk, though dislocations will be repelled by relatively hard layers for similar reasoning [15, 20]. Dislocation-dislocation reactions can also occur; dislocations of the same sign tend to repel one another while dislocations of opposite sign tend to attract one another to annihilate. In the case where dislocations repel one another, a dislocation pile up often occurs. Usually, these arrays form when a dislocation source is activated and generates several dislocations along the same slip plane. Dislocations will periodically be emitted from the source, as long as sufficient stress is applied, and travel through the material until reaching a boundary, for example a grain boundary or sessile dislocation configuration. Since the energy barrier for continual dislocation motion will be far too high due to large crystal misfits, dislocations will not move past these boundaries. This results in the leading dislocation, close to the boundary, repelling the other dislocations generated at the source, creating a back-stress on the source until the back stress exceeds the stress for source operation. The back-stress for an array of edge dislocations is given by [20]:

$$\tau_{BS} = \frac{n\mu b}{L\pi(1-v)},$$

2.7

where n is the number of dislocations in the pile up, and L is the distance between the source and the leading dislocation.

It is also important to recognize the barrier for a dislocation to move in a crystal structure. The most basic barrier imposed on a dislocation is by the crystal lattice itself. This energy was first described by Peierls [22] and quantified by Nabarro [23], and quantifies the resistance of the crystal lattice as a dislocation moves through it. This can be visualized by an edge dislocation moving one lattice dimension, a, where there is a positional variation in resistance as
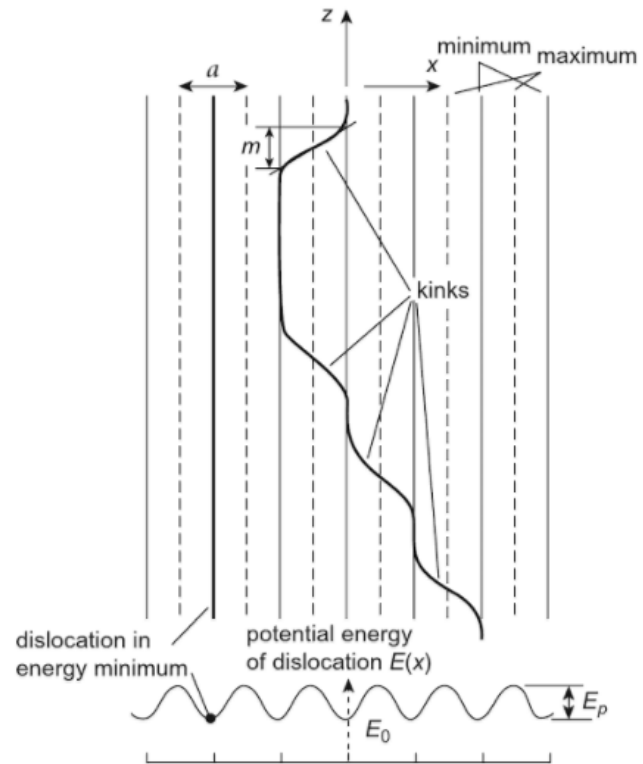
Figure 2.2: Periodic energy barrier to dislocation motion due to the Peierls stress. Dislocation kinks are also shown as dislocations move from one slip plane to another. Taken from Reference [20].

shown in Figure 2.2. This figure simply models that energy minima exist with minimal atom disregistry as a dislocation moves on a slip plane. While not all portions of the dislocation will exist on positions of energy minima, they will preferentially move towards these locations, forming kinks as dislocations proceed throughout the material. Kinks are simply described as steps that displace dislocations on the same slip plane, these are also shown in Figure 2.2. Kink width, m, is dependent on the Peierls energy. The maximum

energy barrier for dislocation motion due to the crystal lattice is the Peierls energy, given by [20, 22, 23]:

$$E_{PN} = \frac{\mu b^2}{\pi(1-v)} \exp\left(\frac{-2\pi w}{b}\right), \qquad 2.8$$

where w is the dislocation width, defined by the distance where the magnitude of atom disregistry due to the dislocation is greater than $b/4$. The maximum Peierls-Nabarro stress per unit length in a crystal is given by [20, 22, 23]:

$$\tau_P = \frac{2\pi}{b^2} E_{PN}. \qquad 2.9$$

As previously stated, if dislocations are given enough energy, mechanically or thermally, to activate, the dislocations will operate in slip systems. A slip system is the combination of the plane of atoms and the direction of which the slip, or dislocation motion, occurs. This usually occurs on the highest density planes and in the densest direction because the cohesive energy between atoms is the strongest here. This means that a dislocation moving along the surfaces of these atoms has the least amount of resistance. Different slip systems can be activated depending on crystal orientation, crystal structure, the magnitude of stress applied, temperature, and other factors. Cross-slip, or the activation of multiple slip systems, also occurs given enough energy for activation [20].

The orientation of a crystal affects the resolved shear stress applied to a material that causes large numbers of dislocations to move and results in permanent deformation; this is best described by Schmid's law [20]:

$$\tau = \sigma \cos\varphi \cos\lambda, \qquad 2.10$$

where τ is the resolved shear stress, σ is the normal applied stress, λ is the angle between applied force and a crystallographic direction, and φ is the angle between applied force and a crystallographic plane, as shown in Figure 2.3. The smallest τ needed for dislocation motion is called the critical resolved shear stress or τ_{crss} as this is the smallest stress that will induce plasticity and these combinations of crystal planes and directions will operate first. For close packed homogeneous crystals, the τ_{crss} will occur on the slip plane and slip direction. Particularly in this work, micropillar orientation will be important in determining expected and observed slip or cleavage planes.
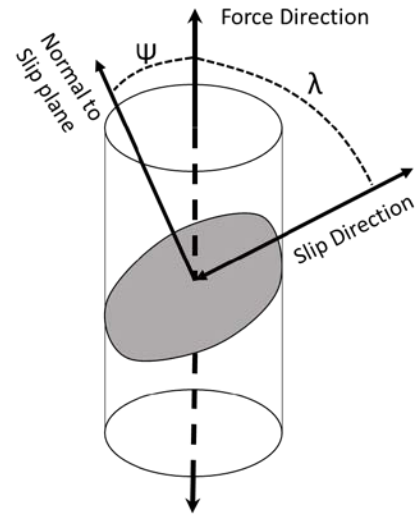
Figure 2.3: Schematic showing the parameters relevant to Schmid's law. Adapted from Reference **[13]***.*

2.5 Fracture and Fracture Toughness

Fracture is the separation of a volume of a solid material into two or more free surfaces. Usually brittle fracture will occur upon a cleavage plane, the crystallographic plane where fracture occurs. These planes are more typical in crystals with limited number of slip systems. In this section, fracture in brittle materials, where linear elastic fracture mechanics can best model the material fracture [12], will be defined.

Theoretical fracture strengths are dependent on the cohesive strength of a material, in simplest terms, this depends on the atomic bond strength or in material property terms, the elastic modulus of the material. The general derivation for cohesive strength can be found in [12], but is approximately equal to $E/2\pi$. As in the case with theoretical yield strengths,

16

the actual fracture strengths are multiple orders of magnitude smaller than the derived values due to preexisting flaws in materials. While there were earlier qualitative observations on this subject, Griffith is credited with the quantitative description of internal preexisting flaws causing lower fracture stresses in glass, using arguments developed by Inglis [24, 25]:

$$\sigma_f = \sqrt{\frac{2E\gamma_s}{\pi a}}. \qquad 2.11$$

In the above equation, a is half the crack length and γ_s is the surface energy per unit area of the crack faces. Equation 2.11 models the energy required for fracture by determining the energy cost of the increase in surface energy of the material as a sharp, internal crack grows from an external stress and represents a critical stress for failure. However, these observations and equations did not apply in ductile materials because some plastic deformation, not accounted for in Griffith's analysis, also occurs. Equation 2.11 was modified to account for some plastic deformation decades later by Irwin [26] and Orowan [27]. This modification added a term for the plastic energy dissipation in a material, γ_p, which is usually much larger than γ_s [12]. While these above approaches are useful, in engineering applications, it is more convenient to model the crack growth process to predict failure. Irwin was the first to propose the idea of a strain energy release rate, G, or the energy required to incrementally increase the length of a crack for plane stress as [28]:

$$G = \frac{\pi \sigma^2 a}{E}. \qquad 2.12$$

If a material reaches a critical value, G_c, then this represents a fracture energy of a material. While G_c can quantify the global energy required to fracture a material, one may be

interested in the local stress state of a crack tip. This can be determined by the stress intensity factor, K. The critical value of K, K_c, is the fracture toughness of the material that
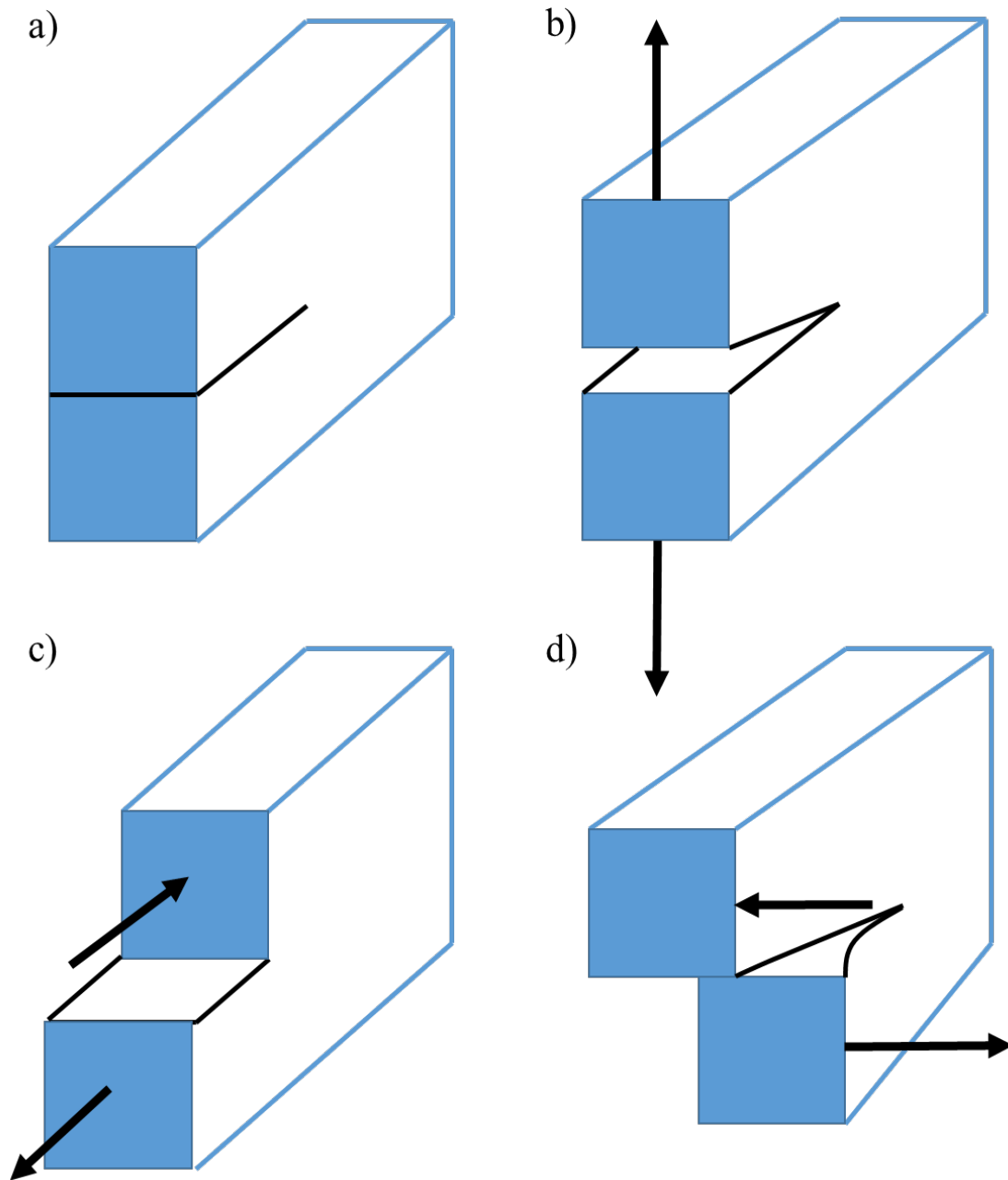
Figure 2.4: Crack loading modes (a) crack with no load (b) Mode I (c) Mode II (d) Mode III. Adapted from References **[12, 13]**.

describes the local stress and strain of a material to fail. The general equation to define K

is [12]:

$$K_x = Y\sigma\sqrt{\pi a},$$
2.13

where x denotes the loading mode, I, II, or III, and Y is a dimensionless constant that

depends on the sample geometry and loading mode. A model with a crack and the three

loading modes are shown in Figure 2.4. Modes I, II, and III can be described as crack

opening, in-plane shearing, and out-of-plane shearing. G and K can be related, for example

in the case of a through-crack in an infinite plane material subject to uniform tension [12]:

$$G_c = \frac{K_I^2}{E},$$
2.14

where K_I is the fracture toughness of a material in mode I. Mixed mode loading is also

possible, where each mode are additive terms that can be used to find the strain energy

release rate. However, this work will focus on determining differences in behavior, from

fracture dominated to plasticity dominated material behavior.

2.6 Ductile Brittle Transition (DBT)

For these investigations, mechanical behavior can be broadly put into two categories:

brittle and ductile. All materials are composed of atoms that are bonded together. If a stress

is applied to materials, the bonds between atoms can elastically, or reversibly, distort to

accommodate this stress. However, once an elastic limit is reached, permanent changes

will occur. If the mechanical response is ductile in nature, energy will be dissipated in a

step-wise process where materials deform and change shape. Brittle behavior, on the other

hand, results in formation of new surfaces by permanent bond breaking. Brittle failure

generally occurs suddenly and is often associated with minimal dislocation activity,

resulting in relatively smooth fracture surfaces. Brittle fracture is more difficult to predict than ductile fracture as typically little to no indication or pre-deformation occurs before catastrophic failure. Ductile failure is accompanied by much more plastic deformation and dislocation activity; in tension, samples typically fail by necking then microvoid coalescence [29, 30, 20]. However, there is a transition between these two behaviors in many systems that is affected by strain rate, size effects, temperature, and impurities [31, 32, 33, 30, 34]. Each of these parameters modifies the energetics of dislocation nucleation and propagation in a material.

One of the ways to define the ductile and brittle nature of a material is by looking at the thermodynamics and kinetics of dislocation motion and changes associated as material processing or environment is altered. Assuming an isothermal process, there is an activation energy, also denoted H_0, for dislocation motion given by [20]:

$$\Delta G^* = \Delta F^* - \tau^* V^* \qquad 2.15$$

where ΔF^* is the Helmholtz free energy change, sometimes referred to as a thermal contribution also denoted as H_σ. Here, τ^* is the effective shear stress, and V^* is the activation volume. ΔF^* is a function of lattice resistance force and the distance over which a dislocation moves. In addition, the energy for dislocation motion can also be related to the macroscopic plastic strain rate, $\dot{\varepsilon}$, of a system as [20]:

$$\dot{\varepsilon} = \rho_m A exp\left(\frac{-\Delta G^*}{kT}\right), \qquad 2.16$$

where ρ_m is the mobile dislocation density and A is the product of the Burgers vector, distance moved for each obstacle such as other dislocations or defects overcome, and the dislocation vibration frequency [20].

Equations 2.15 and 2.16 demonstrate that dislocation motion can be altered by a variety of parameters. One of the most apparent is strain rate; as strain rate increases, there is less time for thermally activated dislocation processes to operate and relieve strain energy in the system. Increasing the strain rate, holding all other parameters constant, has been shown to result in a DBT in some material systems such as single crystal iron [35] and tungsten [36]. Temperature also has a large effect that has been well studied in metals [20, 37, 38]. Most metals have a DBT temperature which has traditionally been determined experimentally by performing tensile tests or through impact testing of notched bars at various temperatures [29, 38]. Varying the temperature respectively increases or decreases the mechanical contribution to the energy needed for dislocation motion and can also give a quantitative way to measure activation volumes. Activation volumes, when multiplied by the effective stress, determine the mechanical energy necessary for dislocation motion at a given temperature in a given material system [39].

Changing the dislocation density in a material also affects dislocation motion because the stress fields of dislocations can interact and limit each other's motion [20, 15]. One way to investigate this is to limit the macroscopic volume of the specimen tested. If the volume of a material is small enough, there are a minimal number of dislocations and in the extreme case, dislocation free [40]. In addition, small volumes can modify the nucleation and motion processes of dislocations due to the increase of free surfaces. This

has been used in a variety of loading modes, especially with nanoindenters [41, 42, 43, 44, 45]. Experiments testing small volumes of material have also shown a DBT when the tested volume is increased [45, 46, 47]. Lastly, the effect of hydrogen content on dislocation behavior, with impacts on the DBT, is another factor that will be discussed in this dissertation.

2.6.1 DBT in Si

Considerable ranges of opinions about the DBT in single crystal Si have arisen over the last few decades [48, 49, 50, 51, 52, 53, 54, 55, 56]. This has continued recently due to a number of findings of room temperature plasticity in Si at the nanoscale [51, 54, 52, 48, 49, 50, 55, 56]. In compression, this can lead to plastic strains of over 50% at 300 K [57], which might be expected due to suppression of fracture from the stress state. Additionally, some tension [58, 59] and bending experiments [59, 60, 61, 62, 63] for nanoscale Si have demonstrated increases in plastic deformation and fracture toughness compared to the bulk. At the nanoscale, dislocation nucleation and mobility are enhanced due to the increased stresses for superseding the Peierls barrier [63]. It has become generally accepted that this allows dislocation shielding to provide an increase in the fracture toughness [52, 64, 65, 66]. However, an accurate model for predicting the DBT has not yet been achieved due to many complicating variables which require extensive data to evaluate. To give some sense of the problem, seven variables are known to affect dislocation nucleation and mobility in Si. These include: temperature [67]; stress state and magnitude [63]; strain rate [67]; doping effects [68, 48, 63, 56]; radiation enhanced dislocation glide (REDG) effects [69], phase transformation effects [70]; and length scale effects [52, 64, 65, 67, 66].

22

The required data to evaluate each of these variables does not exist yet, which will become a task of increasing importance as nanotechnology continues to mature. Thermal and stress assistance are generally well understood in terms of the energetic competition between plasticity and fracture at the bulk scale, but coupling with length scale effects requires further study. For example, at low temperatures (<600 K (327°C)), sub-100 nm Si spheres under compression have shown K_{IC} values in the range of 1- 10 MPa-m$^{1/2}$ [52, 65] while 1 and 4 µm bending beams have published values of 1-4 MPa-m$^{1/2}$ [71]. It is reasonable to attribute the large degree of scatter in these measurements to the effects of the seven above listed variables.

The external variables of strain rate, temperature and applied stress could combine with three input parameters based on internal variables for a fracture toughness model to predict the DBT in Si: the effective stress, σ^* or τ^*, V^*, and H_0. Length scale effects on the DBT in Si are complex and can produce dramatic shifts of the DBT, requiring length scale as an additional variable. Utilizing these parameters allows for changes in plasticity mechanisms as dictated by a unique combination of length scale, strain rate, applied stress and temperature. This is similar to Ashby-type mechanism maps but the latter almost exclusively are oriented toward creep processes [1] or toward geological materials such as ice [2]. It is suggested that there should be a DBT mechanism map for relevant materials using normal stress, strain rate, and temperature as variables, but with an additional axis depending on length scale. An artistic rendition of such a map as imagined for Si is shown in Figure 2.5. Here, the x-y plane at the back is the normal temperature-stress axes with the z-axis being the length scale. This accommodates the length scale effect of increasing flow

23

stress with decreasing size. For yielding, it suggests a transition near 100 nm where the strength might increase more rapidly, but as ~4 nm is approached, the strength could decrease due to a fully shearing mode, as suggested by simulations in Reference [72]. This would shift in 3-D space as strain rate either increases or decreases. This is depicted on the back plane where bulk behavior might be experienced for length scales of 10 μm or greater. Note that Figure 2.5 has dimensions on it for discussion, while realistically one would use a normalized stress and temperature based on modulus and melting point.
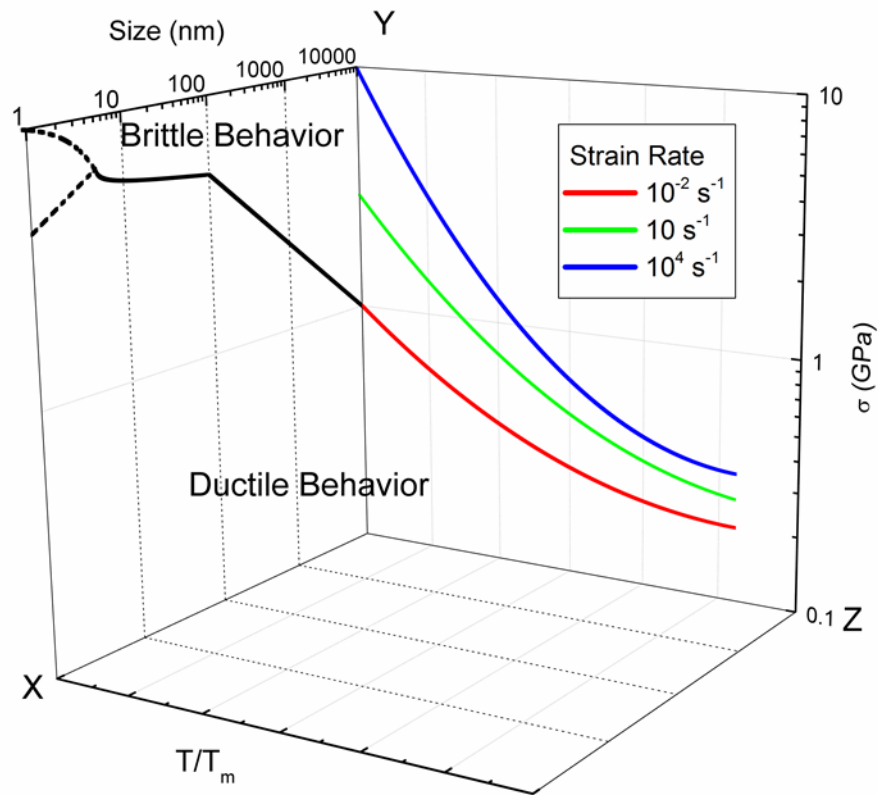
Figure 2.5: Three-dimensional depiction of normalized temperature and strength with roughly perceived size effect. Lines indicate likely mechanism transitions, though specific mechanisms cannot be provided as experimental and theoretical data is limited. The dotted lines below ~4nm in size indicate either a decrease due to shearing or reach near theoretical fracture stresses.

2.6.1.1 Modelling

To produce a mechanism map for the DBT in Si as described in the previous section, a model for predicting the fracture toughness based on dislocation emission and subsequent shielding of the crack tip is necessary. One possibility that could include all the variables outlined in the previous section is an approach was previously proposed by the Gerberich group [64, 73] which included τ^*V^*, in an equation similar to what has been used for thermally activated creep mechanisms [74] and explicitly used in a brittleness investigation of Fe-Si single crystals [64]:

$$G_{IC} = \left\{ \frac{V^*\psi_0\tau^*}{b^2\dot{\varepsilon}} \right\} exp \left\{ -\frac{H_0 - \beta\tau^*V^*}{kT} \right\}$$

2.17

Here, Ψ_0 is a function including Poisson's ratio, the pre-exponential dislocation velocity, the mobile dislocation density and the plastic strain, $\Psi_0 = f(v, v_0, \rho_m, \varepsilon_p)$. G_{IC} is a strain energy release rate associated with fracture instability and can be related to fracture toughness, K_{IC}, through Equation 2.14. Using previous investigations, this leaves β, a geometrical constant describing the back stress of dislocations on the crack tip. Both Ψ_0 and β are adjustable parameters, but work in Chapter 4 will show that at least one can be at or near unity. As is, this K_{IC} for crack propagation would need to consider orientation effects for cleavage or possible mixed mode crack growth. This model arises from Cottrell's thermally activated dislocation velocity [75]:

$$v = v_0 exp \left\{ -\frac{H_\sigma}{kT} \right\}$$

2.18

where the activation energy is made stress free by the subtraction of internal stresses through Equation 2.15. This approach can be considered a thermally activated dislocation "mobility", which allows for an apparent energy to be measured based upon a stress-free activation enthalpy, H_o, and the τ^*V^*, term. All of these quantities can be simulated atomistically if the time disconnect is resolved. Until data are available, it is impossible to evaluate the applicability of such a model to Si. Regardless, this section should provide context for why it is thought that the three parameters of effective stress, activation volume, and activation energy are important. With this established, each of these parameters will be discussed in greater detail.

2.6.1.2 Activation Energy, H_0

Activation energy is typically utilized to characterize changes in dislocation mobility as a function of temperature. In Si and other semiconductors, H_o plays arguably a more important role compared to metals since it is larger, as the electronically active dislocations are strongly affected by dopants, impurities and electron irradiation. As previously stated, n-type and p-type doping have been observed to increase, and occasionally decrease, dislocation velocities [48, 49, 68, 69, 56] and can result in activation energy decreases from 2.2 eV to 1.6 eV [69]. Also, n-type doping was observed to have a stronger effect at similar dopant concentrations compared to p-type, but in both cases the velocity increase will diminish with higher temperature as one might expect from the thermal activation law. At low temperatures and high p-doping concentrations, velocities were observed to remain the same, or even decrease slightly [68, 69]. It has been proposed that dopants increase the dislocation velocities through promotion of double kink nucleation, which will affect screw

26

and 60° dislocations differently [68]. Impurities, such as hydrogen, have also been observed to increase dislocation velocities even more dramatically, producing activation energy shifts from 2.2 eV to 1.2 eV [76]. Similarly, it has been observed that with increasing electron radiation, e.g. 300 keV vs. 100 keV, that dislocation velocities can increase [77], and activation energy can decrease by 0.68 eV [78]. Such large changes in dislocation velocity as induced by doping, electron irradiation or impurities would have a large effect on plastic energy dissipation from a crack and dislocation shielding processes, which emphasizes the need for careful experimentation.

2.6.1.3 Flow stress, σ, and the Effective Stress, σ* or τ*
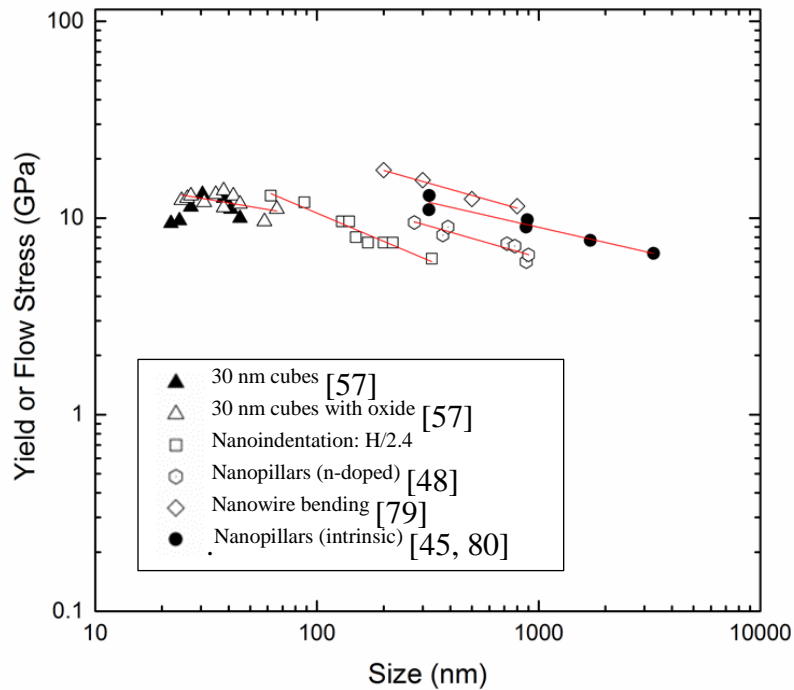
Figure 2.6: Effect of stress state, specimen shape, impurity levels and slip character on the strength of Si. All trends show a dependence on flow stress with size, the smallest nanocube samples may even support a change in mechanical behavior at extremely small sizes.

The variability in flow stress measurements of nanoscale Si is shown in Figure 2.6.

From five different studies [48, 57, 79, 45, 80] it is shown that at the given length scale, five different relationships evolve. In the 20-100 nm scale regime, near theoretical strengths are observed which then decrease as size increases. The slopes of the five studies in Figure 2.6 are similar but at a given length scale, the flow strengths can decrease by more than a factor of two. As previously discussed, the influence of variables such as intrinsic versus doped Si [68] (n- or p-), contact geometry associated with specimen type or *in-situ* observations in electron microscopes (REDG) [69] must contribute. Specimen types ranged from nanoindentation, nanopillars [48, 45, 80], and nanocubes [57]. Clearly, there is a need for systematic studies of flow stresses to properly determine the effects of these variables.

Though measurements of flow stress are essential, it is not necessarily the actual stress responsible for overcoming the Peierls barrier or inducing fracture. Here, the state of stress and the length scale play a critical role. For dislocations, after appropriate resolution of applied stress into a shear stress acting on the slip plane, internal resistances need to be subtracted. The flow stress reduced by internal stress, which results from defects including previously emitted dislocations, can be described as an effective stress. Generally, internal stresses are higher for nanoscale materials due to dislocation confinement, as illustrated by numerous researchers [81, 82]. Recently, *in-situ* TEM compression of Si nanocubes (25-40 nm) as well as post-mortem imaging [57] were used to guide predictions of the back stress contribution to hardening, which reached values up to ~4 GPa by Equation 2.7. In the case of the Si nanocubes, significant effort was required to adapt the back stress approach to the correct geometry. This presents a challenge moving forward, as the variety

28

of stress states and specimen geometries will require computation or more extensive TEM characterization.

An additional factor impacting flow stress in Si is phase transformations, one of the least well understood phenomena in terms of its effect on the DBT. These can involve the most commonly discussed transition of the Si diamond cubic structure to the β-tin structure under hydrostatic pressure [49, 83, 56], but several other possibilities have been discussed in the literature and observed in computational studies [84]. Experimentally, phase transformations have been observed in both nanoindentation [83] and confining pressure experiments [49, 56]. In all cases, a phase transformation would result in fundamental changes to the plasticity-fracture energetic competition and would affect both the effective stresses and the activation volumes.

2.6.1.4 Activation Volumes, V*

Activation volumes are useful parameters to quantify the mechanical energy required for dislocation nucleation and mobility. As demonstrated in the previous sections, it is most appropriate to use an effective stress to assess activation volume. This is not so essential for either dislocation free or relatively free single crystals, which is typical for Si. It is noted that this assumption for strain rate jump tests becomes less accurate the further deformation has been applied due to the increasing dislocation density. Nanowires or nanopillars have typically been used to measure activation volumes in tension or compression as defined by [85]:

$$V^* = k_B T(\frac{\partial ln\dot{\gamma}}{\partial \tau})_T$$

Using this to determine V*, literature data [1, 16, 21] for both high temperature bulk single

crystal studies [63, 68] and low temperature, high stress nanopillar studies [48] gives the
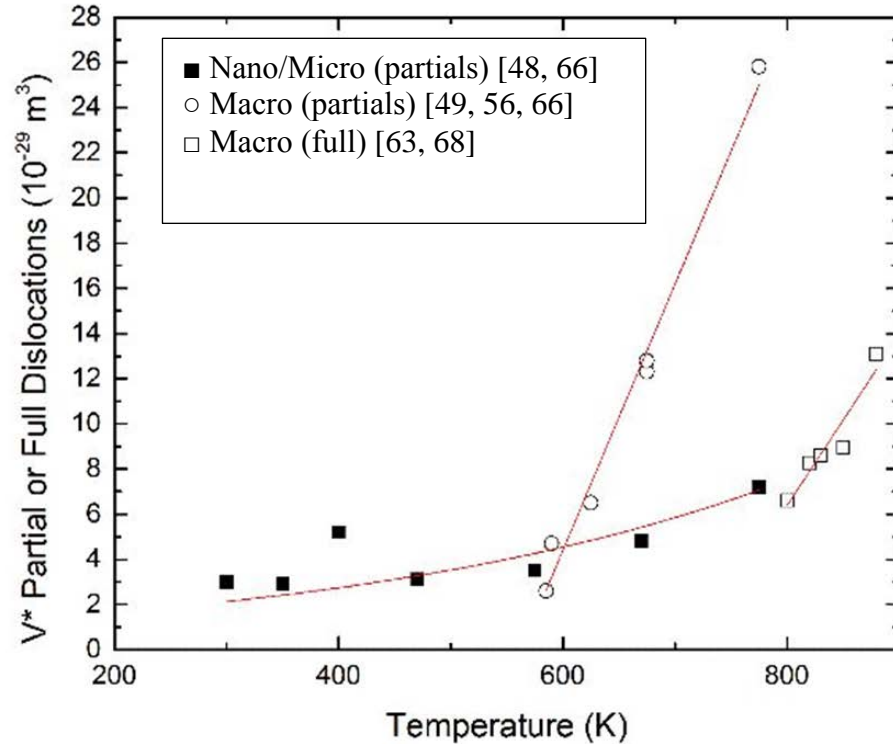
Figure 2.7: Activation volumes for partial dislocations at high stress, low T (■) and for lower stress, higher temperature partial dislocations (○) and full dislocations (□).

relationship in Figure 2.7. It can be seen that the macro-scale data has a fairly steep rise

above 600 K (327°C). On the other hand, the micro/nano-scale data depends more

gradually on temperature above 600 K and below are nearly independent of temperature.

The activation volumes below 600 K are near 1 b^3 and therefore it would be difficult to

conceptualize a further decrease without dislocation core changes. Additionally, there may

be a secondary transition below 800K (527°C) if full rather than partial dislocations are

involved as suggested in Figure 2.7. If the atomic core structure is involved, this may be relevant. This activation volume data strongly suggests there is a mechanism change below 600 K as others [48, 67, 72] have discussed. The result of this activation volume scaling below 600 K is that with τ^* increasing with decreasing temperature and V^* being relatively constant, the product of the two increases. This has a strong effect on the DBT as originally formulated.

A possible explanation for the activation volume transition seen in Figure 2.7 is a switch to dislocation nucleation control rather than dislocation velocity control, the conclusion reached by the simulations of Kang and Cai [72]. Using a modified embedded atom method, Kang and Cai [72] simulated [110]-oriented Si nanowires with diameters of 2 to 7 nm deformed under tension using strain rates of 5 x 10^8 sec^{-1} and temperatures of 100 K (-173°C) to 1200 K (927°C) [27]. They demonstrated nanowires could undergo a DBT with temperature at d > 4 nm but at smaller dimensions fail under shear. This size could be shifted to much larger length scales than 4 nm at slower strain rates more realistic for experimental conditions. In future simulation investigations, this would represent an additional avenue to explore.

In the original formulation of the brittleness transition for Si by Gerberich et al. [45], the previous explanation was applied to length scale effects assuming the stress-strain effect is a linear function. This resulted in an exponential relationship between fracture resistance and the zero stress activation energy for dislocation velocity. Later, others considered that thermal activation alone was not sufficient and the brittleness transition temperature necessarily required a stress-work function in the exponential leading to

Equation 2.17 [64]. However, this implies that the normal strain rate sensitivity parameter in Equation 2.19 is inconsistent with Equation 2.17. One might address this with transition state modeling implied by Figure 2.7 or simply express V^* differently above and below about T= 600K (327°C). The latter could be accomplished by either using a separate functional form for strain rate in Equation 2.19 below the transition or requiring the exponential term to be unity with $H \sim \beta\tau^* V^*$. While this was found to be the case at low temperatures, further development is beyond the scope of this section without more consistent measurements of all thermally activated parameters.

2.6.1.5 Si DBT Summary

Above, a view of a pathway towards a fundamental description of the DBT temperature across stress levels and small length scales is described. It is an analytical method utilizing experimental parameters which, as proposed, can be precisely measured eventually. These include internal variables (V^*, H_0 and b), external variables ($\dot{\gamma}$ and T) and mixed variables (τ^*) containing an external variable, τ, and an internal one, τ_{BS}. It is potentially significant that these same variables appear in low temperature dislocation creep models as DBT mechanism maps, similar to creep mechanism maps, which were proposed as the future goal for modelling efforts. It is also believed that these variables can eventually be simulated using atomistic and discretized dislocation models.

2.7 Hydrogen Embrittlement

The previous sections describe many of the parameters associated with a DBT of Si which are also implied to be relevant to other hard materials. However, there is an

32

additional factor that can impact dislocation behavior drastically: the embrittlement by hydrogen, where some materials can fail at much lower stresses than anticipated as hydrogen diffuses into and reacts with the atoms in a material. However, the mechanisms to describe this behavior are highly contested. Here the basics of hydrogen incorporation into material and a short description of the potential mechanisms are given.

2.7.1 Mechanisms of Hydrogen Embrittlement

Hydrogen embrittlement mechanisms require the ingress of hydrogen species into the host material lattice. While this can happen by a few mechanisms [86, 87], and does occur in Sc [88], Ni [88], and Si [89, 90], it will not be discussed here. Generally, hydrogen species will be transported to a material surface, be absorbed into that surface, and eventually diffuse throughout the bulk material. Some experimental methods for hydrogen charging are discussed in the subsequent section. Once hydrogen has entered the system, hydrogen can react with a host material in three main ways: by forming hydrides, as interstitials, and by forming gas bubbles [91]. Particularly, in this work, Sc and the corresponding hydride counterpart ScD_2 will be discussed as well as the gaseous hydrogen charging or interstitial hydrogen incorporation of Si and Ni. The addition of hydrogen to metals and other hard materials that causes failure at much lower stresses than expected is called hydrogen embrittlement. This observation was first reported in 1874 by Johnson by placing metals in acid solutions [92]. Zappe and Sims proved these changes were caused by hydrogen in 1941 [93].

Several mechanisms of hydrogen interaction have been developed over the years, but no consensus has been reached over which mechanism is most prevalent. However,

there are three main mechanisms that will be discussed here: hydride formation and local cleavage, hydrogen-enhanced decohesion (HEDE), and hydrogen-enhanced local plasticity (HELP).

Hydride formation is different than the other forms of hydrogen embrittlement listed here in that the hydrogen species in hydrides are trapped in a material through relatively permanent bonding to the host material [94]. This results in a phase change of the material, where the material is homogenous and has different chemical and physical properties than the original material [88, 91]. This type of embrittlement is limited to metal systems, and only the systems where hydrides are stable at the conditions of the test [95]. Hydrides are generally considered more brittle than their metal counterparts [96], though plasticity, generally limited by the slip systems and twinning in metal hydrides, has been observed [95]. Hydride formation and subsequent local cleavage is a relatively straightforward mechanism at high hydrogen concentrations just considering the differences in mechanical properties from phase changes, but is operational only in systems that readily form hydrides like titanium [97, 98]. This mechanism can be much more complex at dilute concentrations of hydrogen when delayed hydrogen cracking occurs and the diffusion of hydrogen species throughout a host lattice can result in higher hydrogen concentration near crack tips and other defects [99, 100]. Hydrogen atoms have a higher solubility near tensile strength fields, this includes crack tips and dislocations. Higher hydrogen concentrations can lead to hydride formation around crack tips or other areas of stress concentration leading to local embrittlement [91].

The other two mechanisms also consider the higher hydrogen concentration near defects in a crystal structure. The HELP mechanism, first published by Birnbaum in 1990, also focuses on the effects of hydrogen interstitials [101]. These hydrogen interstitials are thought to form Cottrell atmospheres around dislocations in a material, and the mechanism focuses on these dislocations located at or near the crack tip. Relatively low concentrations of hydrogen lower the local stress around a dislocation, thus shields dislocation-dislocation interactions which increases the local plasticity near a crack tip eventually causing ductile failure [102, 103, 104]. However, others have also shown that high concentrations of hydrogen will impede dislocation motion, providing resistance to plastic deformation [105]. Troiano first proposed the HEDE mechanism in 1960 [106] though this further matured with Oriani's work in 1978 [107]. The HEDE mechanism proposes that interstitial hydrogen lowers the local cohesive strength in the lattice due to the expansion that results from the interstitial atoms. This results in lowering the energy required for brittle fracture [108, 107]. The HEDE mechanism depends on hydrogen concentration at crack tips exceeding a critical amount, though this can be aided by stress driven diffusion of hydrogen as well as hydrogen being trapped at sites such as crack tips where local lattice distortion can be energy minima for hydrogen interstitials [109].

There still remains a large debate whether HELP or HEDE mechanisms dominate and others have suggested that a combination of these mechanisms may contribute to hydrogen embrittlement of a material [110, 111, 112, 113, 114]. The two mechanisms are contradictory, but may apply to different materials in various conditions as described elsewhere [110, 111, 112, 113, 114]. Regardless, evidence exists for both mechanisms and

the small concentrations and high diffusivity of hydrogen, particularly in metals, makes conclusive confirmation of one definitive mechanism difficult to obtain [115, 116, 117]. To further complicate this debate, other researchers are suggesting alternative explanations for hydrogen impacts [118, 119]. It is a goal of this work to create more experimental evidence of hydrogen impacts on mechanical properties through nanoindentation and micropillar compression. Dislocation activation parameters will be calculated in attempt to analyze what mechanism is more realistic in the materials of interest and whether ductility or fracture is enhanced.

It should also be noted that all of these mechanisms apply for hydrogen's isotopes, mainly deuterium (D) and tritium (T). These species have one or two additional neutrons in the atom nucleus respectively, causing them to have slightly lower relative diffusivities than the typical hydrogen atom [90]. However, the hydrogen typically used in gas charging is the standard hydrogen species.

2.7.2   Hydrogen Charging Methods

Hydrogen charging, or the incorporation of hydrogen into a host lattice, is how most study hydrogen effects in materials. There are several methods to hydrogen charge a sample that includes electrolytic, aqueous, plasma, and gas charging. Electrolytic hydrogen charging works by using the desired sample as a cathode with an anode, typically platinum, placed in an acidic solution under an applied voltage. The voltage results in the formation of hydrogen gas on the surface of the cathode that is also introduced into the sample itself through various mechanisms described elsewhere [120]. While this method is effective, it is not suitable for the current testing methods as severe surface damage can occur due to

36

high fugacity of hydrogen at surfaces and defects within the materials being charged [121, 122]. Attempts made for hydrogen charging in Ni via a cathodic reaction in this work also provided a surface too rough for nanoindentation, see Chapter 4.

Aqueous charging of hydrogen is also possible, particularly in metal samples where metal surfaces can dissociate hydrogen atoms from water or readily incorporate hydrogen ions into the crystal lattice [123, 124]. This process involves placing a material in an aqueous, acidic environment and waiting some time to allow charging or diffusion to occur. This process often takes a long time and does not result in large hydrogen concentrations, so was not considered for testing. Plasma hydrogen charging can also be used, where a sample is placed in a chamber and a high-energy hydrogen plasma is produced; however this also has the potential of causing surface damage to the sample in similar ways to electrolytic charging [125]. Plasma charging was used for a portion of this project in a one-of-a-kind reactor built by Andrew Wagner in the Kortshagen labs at the University of Minnesota. While the charging seemed to not impact the sample surfaces much, the reactor was shut down before additional experiments could be completed.

The last method for hydrogen charging is gas-phase charging. In this method, a sample is placed in a vacuum chamber, purged with argon or nitrogen, then hydrogen gas is added. These chambers work best at high hydrogen pressure and elevated temperature to facilitate diffusion of hydrogen into a lattice. Usually this sort of charging takes place for several days to several weeks to ensure uniform hydrogen distribution in the samples. This method seems to be the preferred method of hydrogen charging because this method is the most easily controlled to predict hydrogen diffusion and minimal sample damage [126, 96],

37

though requires a significant degree of skill and safety precautions to operate successfully. Hydrogen charging facilities are limited, but there is a facility currently operating at Sandia National Laboratories for such work, as described in Chapter 4. Gaseous hydrogen charging does not seem to affect the surface of the materials being charged, which is useful for testing with nanoindentation and for maintaining small features of interest.

Knowing the concentration of hydrogen in a system is ideal for the future modeling and explanation of the mechanisms behind the mechanical behavior of a material. However, this is incredibly difficult to determine as hydrogen content will constantly change throughout testing if a material is not constantly charged with an *in-situ* method. In this work, attempts will be made to estimate hydrogen levels, but actual hydrogen content in the samples was not measured.

2.8 Nanoindentation

Nanoindentation is similar to many other indentation techniques, however, nanoindentation has a displacement resolution on the order of nanometers, nm. instead of micrometers, μm, such as in many industrial indentation techniques like Vickers, Knoop, and Rockwell indentation. In addition, the indentation imprints for nanoindentation are often too small to be measured through optical microscopy, so assumptions must be made about the geometry of the tip for mechanical property measurements.

2.8.1   Data Analysis

The raw data from nanoindentation is a load (P) versus displacement (h) curve. Due to the elastic-plastic nature of materials, this also results in a terminology associated with the definition of displacement for testing. The total displacement, h_{max}, measured by the

indenter includes the elastic displacement, h_e, and the residual or permanent displacement, h_r. Instead h_{max} can also be composed of h_a, the distance from the original sample surface and where the indenter is in contact with the sample, and the contact depth, h_c, or the remaining displacement where the indenter tip and sample are in contact. Here, h_c is the most important displacement as this is used to determine the area between the tip and the sample, and should be less than h_{max} unless material flows around the indenter as in very ductile materials [127, 43]. All the varying displacement definitions can be seen in Figure
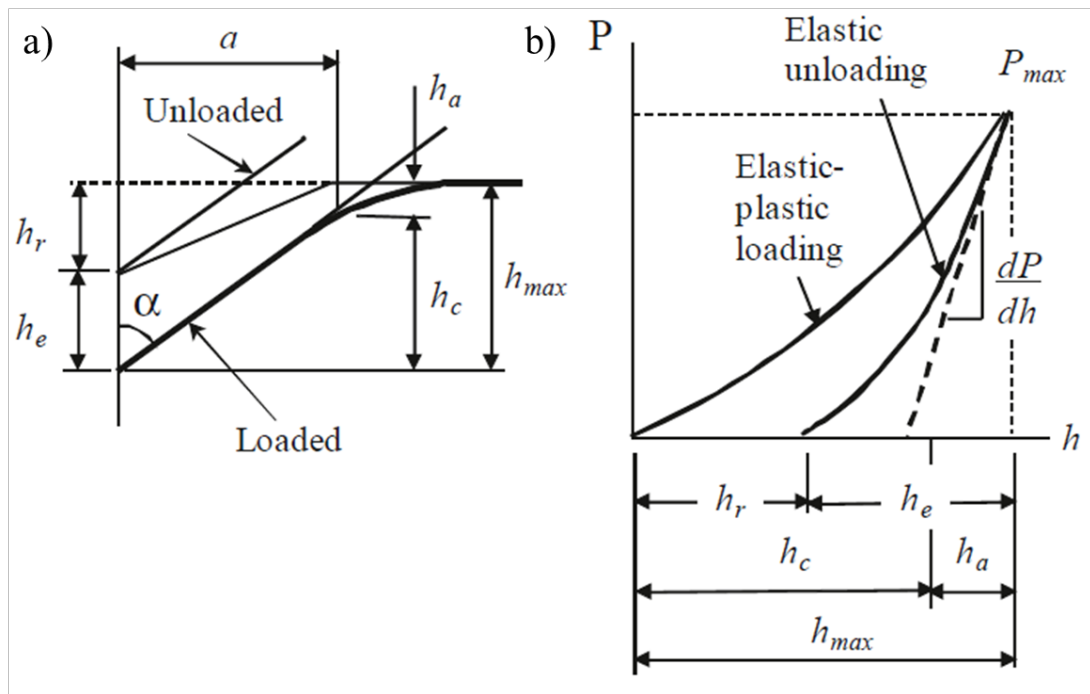
Figure 2.8: a) The indenter and sample configuration showing a loaded and unloaded condition and the terminology for different displacements b) a typical load-displacement curve for a conical indenter tip. Both images taken from Reference [127].

2.8.

Indentation testing is slightly different than many other mechanical testing techniques because the unloading curve is used to determine the elastic modulus of the material being tested. This is because during loading, the material elastically and plastically deforms

39

simultaneously, but the unloading response is ideally only an elastic response. The unloading portion of the load displacement curve, *dP/dh*, is called the stiffness. This parameter is shown in Figure 2.8b. The stiffness of a material can be used to determine the reduced elastic modulus of a material through the following relationship [127, 128]:

$$E_r = \frac{\sqrt{\pi}}{2\sqrt{A(h_c)}} \frac{dP}{dh}.$$

2.20

E_r is called the reduced modulus because the modulus does not take account for the deformation of the indenter tip. However, for diamond tips, with large elastic modulus and small Poisson's ratio, the reduced modulus is usually a good estimate for the elastic modulus. The following equation is used to determine the elastic modulus from the reduced modulus [128, 127, 43]:

$$\frac{1}{E_r} = \frac{(1 - v^2)}{E} + \frac{(1 - v_i^2)}{E_i},$$

2.21

where subscript '*i*' indicates indenter tip properties. Diamond has a Poisson's ratio of 0.07 and an elastic modulus of 1140 GPa [128].

Another property commonly measured using nanoindentation is hardness, *H*. Hardness is defined by *Pmax/A(hc)* [127, 43], where *A(hc)* is the contact area between the material and indenter tip. The indentation hardness is a quantitative number and is more useful for material comparison than other hardness values, such as the Mohs hardness, where hardness is only a relative measurement. The indentation hardness can also be related to the yield stress of bulk materials through an empirical relation that was first reported by Tabor [129, 130]. In general, the yield stress of a material is one-third the

hardness of the material, though other empirical relations, particularly when considering brittle materials, have a yield stress is a factor of 1.5-3 less than the hardness [130, 131].

Hardness values have an indentation size effect that must be considered during data analysis and interpretation [132, 133, 134]. This phenomenon comes from local dislocation hardening, particularly with low displacements and sharp indenter tips. However, there are also apparent indentation size effects that are present in nanoindentation data, particularly at low displacements where the interactions between the indenter tip and sample are not accurately represented through the tip area function [127]. The latter effect will result in higher modulus and hardness values at the lower contact depths using sharp indenters.

The last very important aspect of nanoindentation is discontinuity in the nanoindentation curve. Normally, nanoindentation curves are smooth on loading and unloading. However, if displacement excursions or load drops are observed upon loading, this is typically indicative of dislocation avalanches or crack nucleation. Additionally, load excursions or pop-ins, large decreases in displacement, on unloading can indicate phase transformations [127]. It is important to note in all such cases that cracking, slip, and phase transformations can have impacts on the material properties determined through nanoindentation data.

2.8.2 Equipment

Nanoindentation experiments were conducted with a variety of nanoindentation equipment from Hysitron, Inc now a subsidiary of Bruker Corporation. The primary instrument utilized in this work is a Hysitron TI-900 Triboindenter in the Characterization Facility at the University of Minnesota, shown in Figure 2.9. This instrument uses a
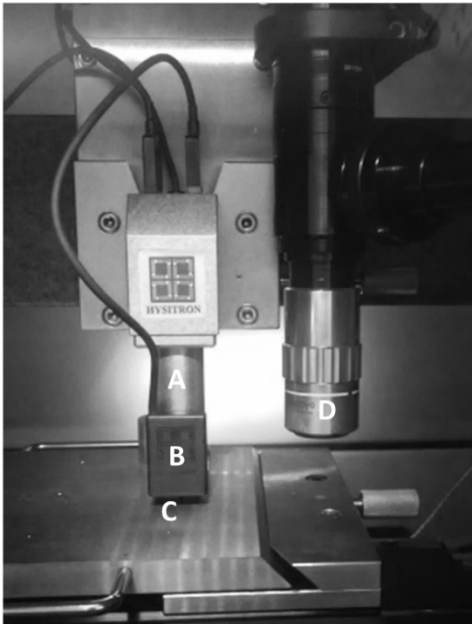
Figure 2.9: Inside the vibration isolation chamber of the UMN characterization facility's Hysitron TI-900 Triboindenter with (A) piezo tube, (B) transducer, (C) indenter tip and (D) optical lens.

sensitive three plate capacitive load-displacement transducer to simultaneously record load and displacement data during testing. The three plates are placed in parallel, with the bottom and top plates fixed and the middle plate is attached to the assembly with springs enabling it to move between the upper and lower plates. Alternating current is applied to the upper and lower plates that are 180° out of phase, and the electric potential is measured at the middle, floating plate. In the middle floating position, there is no electric potential and no displacement. Loads are applied by adding a DC offset to the lower plate, creating an electrostatic attraction that brings the floating plate downwards. The load is determined from the amount of additional DC voltage applied. The corresponding change in electric potential, or the addition of the AC signals from the upper and lower plates, linearly corresponds to the displacement of the center plate after calibrations are completed [135]. A simple schematic of the tip showing the three plates, tip, and springs for the tip is shown in Figure 2.10.

In addition, the triboindenter has a piezo-tube that can be used for very fine positioning of the testing tip and to scan the surface of samples in a method similar to scanning probe microscopy
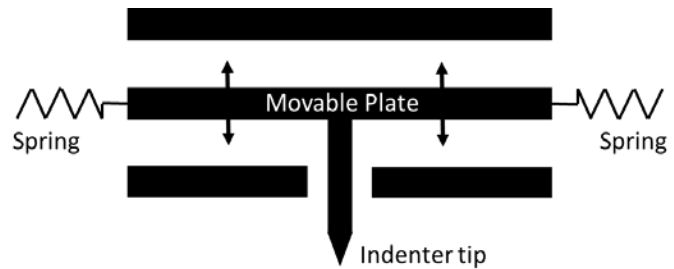
Figure 2.10: Simple schematic of Hysitron's three-plate capacitive transducer adapted from Reference **[128]**.

(SPM). Nevertheless, scanning in the triboindenter has much lower sensitivity and resolution than a typical SPM due to the much larger, rigid diamond indenter tips instead of the smaller, flexible Si cantilevers. There are four basic geometries for an indenter tip in the triboindenter: cube corner, Berkovich, flat punch, and conical. Berkovich and cube corner tips are relatively sharp pyramidal sharp tips which are suitable for activating flow and inducing fracture [127]. This makes them well suited to indentation into two dimensional surfaces. Blunt conical and flat tips have applications for indentation as well, particularly for amorphous materials [127], but here are utilized for small volume compression testing as they can provide full contact with the pillar and are easy to analyze. Conical, Berkovich, flat and cube corner tips are used throughout this work.

The most important aspect of indenter tips for facilitated analysis is a known tip geometry. The projected area of the tip on the sample is relevant to the stresses that are applied to the material. The tip area function, which describes the projected tip area on the sample at a given contact depth, is calibrated for each tip before all testing and as the tip geometry changes from wear, etc. This is done by indenting a known sample, here fused quartz, with a range of loads that include all the relevant contact depths on a sample of

43

interest. The hardness and modulus data generated from each of these test is calibrated to the known parameters of the sample by changing the contact area of the tip. A function is fit to the contact depth versus contact area for each tip using the standard sample that then can be applied to unknown samples. This applies for all materials where the tip is much smaller than the sample being tested. When testing sample geometries that are smaller than the relative tip geometry, such as in micropillar compression, the stresses calculated are relevant to the geometry of the pillars if the pillar and tip centers are well aligned.

Other important calibrations to consider during nanoindentation testing are proper determinations of instrument or frame compliance, C_f, electrostatic force constants, ESF, and lastly drift corrections. When done correctly, the compliance of the instrument, in other words the elastic response of the instrument parts, can be found and subtracted from all nanoindentation data. This is done by performing several high load indents into a known material, like fused quartz, and finding the y-intercept of measured compliance versus $1/\sqrt{P_{max}}$ [127, 128, 43]. The ESF is a spring constant that subtracts the spring resistance as the center plate moves and is found by doing an indent in air, where the spring constant can be determined from the load that is generated from the spring as the tip displaces. Drift corrections are applied before each individual test and account for linear displacement changes in the instrument, usually from creep from the piezotube and thermal drift, by measuring displacement changes when the tip is in contact with a sample at a constant load.

The nanoindentation data collected are further bolstered by vibration minimization with a vibration isolation unit and a high mass, stiff frame. The last important thing to consider from a practical standpoint in mechanical testing is sample mounting. Samples in this work

are all placed on a magnetic stage to minimize vibration and sample drift. This means that the material used to mount samples on magnetic media, in this case SPM pucks, needs to be non-compliant and stable. The materials used here is usually Crystalbond, a vacuum compatible wax; it is melted to adhere a sample to a mount. This does take some time and heats the sample to approximate 100°C. The benefit of using Crystalbond is that it can be re-melted or dissolved with acetone if samples need to be remounted. If samples are sensitive to time or temperature, samples can be permanently mounted with superglue. It is also important for samples to be properly prepared for indentation to obtain the most representative data. This means that samples should be free of residue, flat, and whenever possible well-polished.

To ensure proper testing or measurement of parameters needed for mechanical property determinations, either *in-situ* nanoindentation or *ex-situ* scanning electron microcopy is also done. *In-situ* testing is where nanoindentation or micropillar compression is visually monitored. Whereas *ex-situ* nanoindentation is where samples are not imaged during testing, but are examined in pre- and post-test condition. This is particularly important in micropillars to ensure no obvious instrument error and the further support data analysis and interpretation.

2.9 Scanning Electron Microscopy (SEM)

Scanning electron microscopy (SEM) is one of the primary methods used to image features below the resolvable limit of optical microscopy. The resolution limit of any microscope is dependent on the wavelength of the beam impinging on the sample. With light, the wavelength ranges from 400 to 700 nm but electrons have wavelengths much

shorter than this. The wavelength of an electron is dependent on its energy, or in this case, the accelerating voltage. As an example, a typical imaging uses a 5 kV electron beam, which results in an electron wavelength of around 0.02 nm [136]. However, this resolution is impacted by a variety of factors that must be balanced to get the best image. These factors include but are not limited to accelerating voltage, working distance, detector location, probe current, charging, and aperture size [136].

While optical microscopy requires light and optical lenses to focus that light, electron microscopy requires an electron beam and magnetic lenses. SEM also requires a vacuum system so that electrons can be extracted and travel sample without being scattered as well as a detector, typically a scintillator, to collect the imaging electrons to produce an image. Two main SEMs are used in this work – JEOL 6500 and JEOL 6700 (Figure 2.11), both have field emission gun (FEG) electron sources. FEG sources use a sharp metal tip, typically made of tungsten, and a set of
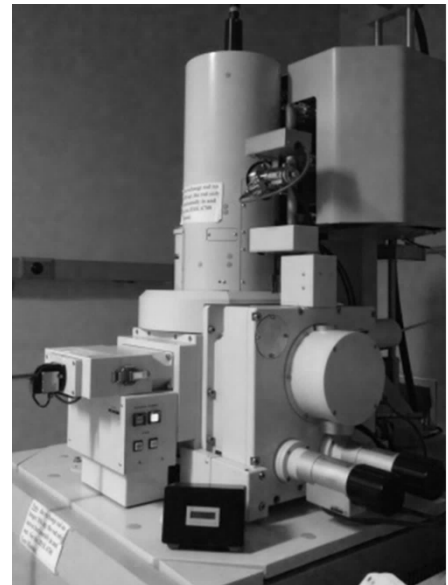
Figure 2.11: UMN Characterization Facility's JEOL 6700 SEM.

anodes. For the tip to produce electrons, an electric potential is created between the tip and the anode closest to it. The potential difference, or extraction voltage, generates an electric field that is concentrated at the tip and aids in electron emission. The second anode is used to accelerate the generated electrons out of the gun, the voltage difference between the tip

and this anode is called the accelerating voltage. Higher accelerating voltages mean faster electrons and larger penetrating depths.

In addition to imaging techniques, with additional instrumentation, one can use electron backscatter diffraction (EBSD) attached to an SEM to create maps of crystallographic orientation that also provide information about phase, strain, and grain size directly. Examples of these maps, used to determine crystal orientation and effective shear stresses can be found in Chapter 4. Instead of using x-rays to investigate materials as in XRD, EBSD uses the same beam used to create SEM images. EBSD also requires a significant amount of sample preparation – the sample must be extremely flat for a strong enough diffraction intensity for orientation identification. To generate an EBSD map, the electron beam is rastered over small areas of the sample. The small areas correspond to pixels in a final EBSD map, the smaller the pixel, the higher the resolution of the map and in general the longer time it takes to collect if examining the same surface area. The EBSD patterns generated through this method are also a result of coherent scattering through Bragg's law, but each pixel is indexed from a backscatter diffraction pattern [14, 136]. EBSD patterns are often colored, where a stereographic projection of a crystal lattice is color map for orientation of a given area. Usually the colored areas of EBSD maps are separated through a misorientation angle, a user input. Defining misorientation angles will elucidate grains in a material if the resolution of the EBSD image is appropriate. EBSD maps can also be visualized as pole figures, which are also stereographic projections of the material, but are shown in black and white, where intensity corresponds to the number of grains oriented at a given angle. These pole figures can be useful as an average of EBSD maps, where texture,

or overall orientation trends, can be better visualized. EBSD is used here as a method to determine grain orientation for stress calculations as well as to determine grain size in Sc and ScD_2 films.

In this work, SEM is primarily used to examine the geometry of micropillars made by focused ion beam (FIB) milling before and after testing micropillars. This is done to best estimate stresses for the testing as well as to observe any features that are created as a result of testing including cracks, slip bands, and bending.

2.10   Focused Ion Beam (FIB)

A FIB is typically a dual beam instrument, one beam is an electron beam that functions exactly like an SEM, and the other is an ion beam, typically composed of gallium ions though helium and other elements are also used. The FIB used in this work is an FEI Quanta 200 3D in the Nano Center at the University of Minnesota, shown in Figure 2.12. In this instrument, the electron and ion beam are situated 52° apart to enable imaging during ion milling. The ion beam in a FIB generally comes from a liquid metal ion source, where a metal is

Figure 2.12: Minnesota Nano Center FEI Quanta 200 3D with (A) GIS system, (B) ion beam, (C) electron beam, and (D) omniprobe.

melted and a small amount flows down a needle of a higher melting point metal, typically tungsten. An electric field is generated between the needle and an anode to extract ions

from the liquid metal via field emission and these ions are further accelerated down the instrument.

Gallium beams can be considered destructive, as the additional mass of the particles making up the ion beam will mill away whatever material encounters the beam. However, to protect and maintain the structure of a material of interest, coatings are used. Most FIBs are equipped with a gas injection system, typically a heater attached to a reservoir of low-temperature sublimating organometallic compounds with platinum components. This system heats up large organic molecules that contain metallic atoms into a gas, injects this gas near a sample, and uses either the electron beam or gallium ion beam to sputter the metal atoms onto an area of interest by breaking the organic material away. Platinum is of particular interest as a protective layer because of its large atomic mass. This makes it more difficult for gallium ions to sputter off these atoms. FIBs also usually have a probe that can be used to take small pieces out of a sample for TEM, cross section SEM work, etc.

In this work, the FIB is used to generate micropillars through progressive milling. This process has been done by a variety of others [137, 138], but will be summarized here.
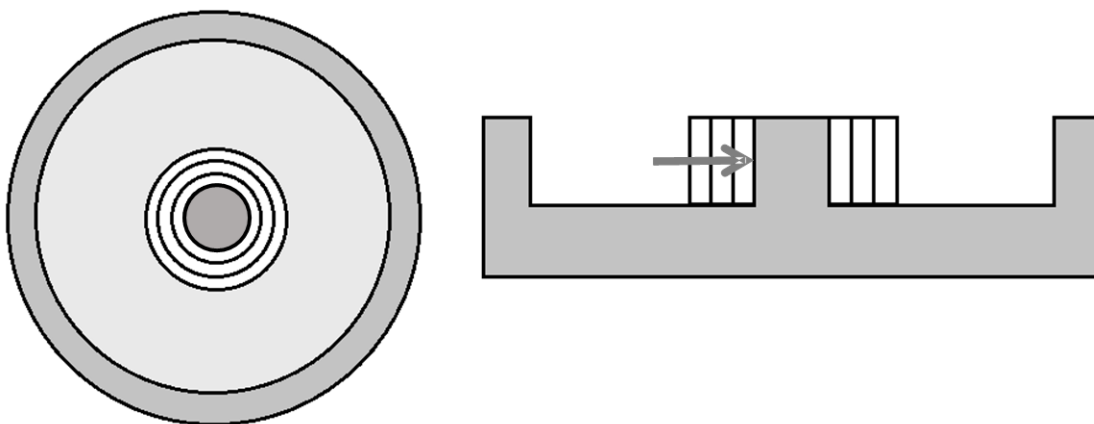
Figure 2.13: FIB cutting procedure showing the steps of circular milling around a pillar of interest. (left) above view of process and (right) side view of process.

Before milling any material, a sacrificial platinum cap is deposited on the sample where the final pillar will reside to limit gallium damage. An accelerating voltage of 30 kV and emission current of 50 pA was found to be optimal on this particular instrument for producing a continuous cap. Figure 2.13 illustrates the cutting method where a progressively lower current is used to make progressively smaller cuts on the sample. The dark grey indicates the substrate as well as the fabricated pillar. First, a cut of 15 μm outer diameter and 5 μm inner diameter is made at 5 μA. This current typically mills away enough material for the desired height of the pillar and leaves enough space for further sputtered material to not be deposited on the pillar. Such a large outer diameter is required to leave sufficient room for a probe to definitively locate the pillars and complete testing without the testing tip crashing into the side walls. A series of smaller and smaller cuts with currents decreasing to 10 pA are then performed in conjunction with imaging with the electron beam between FIB cuts to obtain the geometry of interest.

Height to diameter ratio is kept low, ranging from a 1 to 1 and increasing to 3 to 1 in attempt to avoid any buckling in the pillars. As aspect ratio increases, bucking becomes
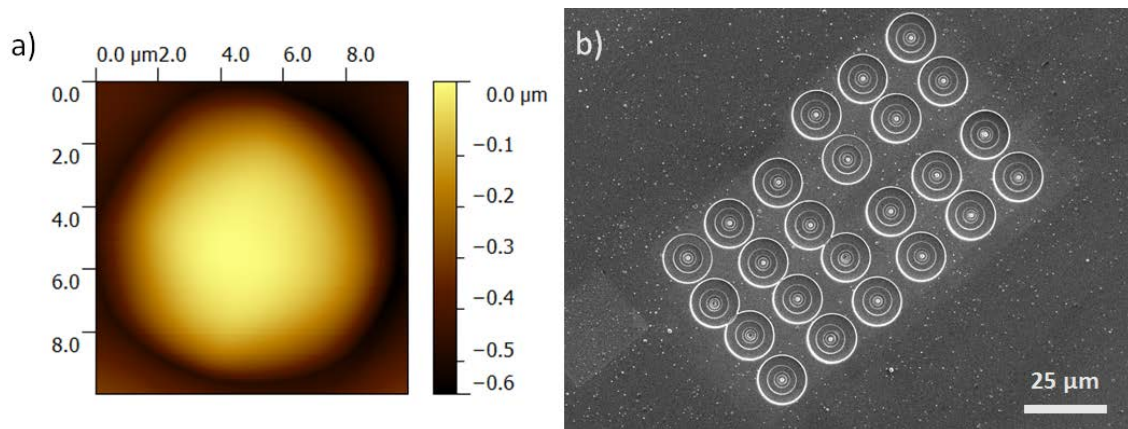
Figure 2.14: a) SPM scan of Si micropillar for testing alignment and b) array of FIB-milled Si micropillars.

an issue [80], where the data generated is more difficult to interpret and is not useful for many of the material property measurements of interest here. To avoid buckling or bending, the load should be applied in the center of the pillar to ensure the entire small volume, or pillar, is uniformly compressed and there are minimal stress concentrators from the tip. If the load is not well centered, then this eccentric loading can induce bending or cracking in the micropillars, as has been observed in small scale tension testing [139]. However, small misalignments are inevitable at this scale and testing method, though scanning pillars with the tip before compressing is done in attempt minimize these effects and control for any tip to optic misalignment. Many pillar samples are tested to attempt to get an average value for material properties, obvious improper pillar contacts are removed from the data – seen in gradual loading slopes in raw compression data – and post-SEM imaging gives another indicator for permanent bending in the pillar. An example of an SPM scan of a micropillar for tip-pillar alignment as well as an SEM image of an array of micropillars are shown in Figure 2.14.

Chapter 3 Hydride Impacts: Deformation and Fracture of ScD$_2$ Thin Films

3.1 Motivation

Neutron generators have become useful analytical tools for a variety of purposes where elemental analysis is key, including applications in the chemical and medical industries. As this technology has developed, smaller, cheaper, and portable neutron generator devices such as neutron tubes are now readily available on the open market. These devices operate by generating neutrons through deuterium-deuterium or deuterium-tritium reactions using a target material [140, 141, 142]. Typically, a thin film metal hydride target is bombarded by a beam of deuterons. Depending on whether the metal hydride is a deuteride or tritide, the nuclear reactions are as follows [143]:

$$\,^2_1H + \,^2_1H \rightarrow \,^1_0n + \,^4_2He + Q \text{ and} \qquad\qquad 3.1$$

$$\,^2_1H + \,^3_1H \rightarrow \,^4_0n + \,^4_2He + Q, \qquad\qquad 3.2$$
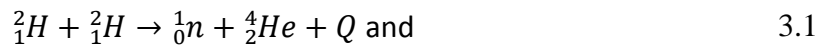
where Q is the latent heat of formation. These devices work best when the target material has high deuterium or tritium content, can interact with the deuteron beam without damaging the target material, and can be controlled over a time and temperature range of device operation.

One such metal hydride, ScD$_2$, is used because it can reach steady-state neutron yield quickly, has relatively good thermal stability, and does not exhibit crater formation in the film during use [143]. However, these systems are very expensive and have some production issues, where films can crack and delaminate during fabrication, prompting

these extended mechanical property studies to support modeling efforts to predict fracture properties and performance in these films [9]. While there is limited information available about ScD_2 mechanical properties, other systems such as TiH_2 [144, 145, 146], ZrH_2 [147, 148] and HfH_2 [88] have the same structure and should have similar mechanical behavior trends. Like many other hydrides studied in compression [95], ScD_2 exhibits both brittle and ductile behavior that warrants further investigation. In addition, while there is a vast amount of information available on bulk-scale hydride materials as previously mentioned, there is very little known about small scale hydride films and observing the behavior of these materials in small volumes is an area of study relatively unexplored. Sc thin films are also relatively unexplored materials, as Sc is a rare material and is very expensive to obtain and purify.

ScD_2 films were fabricated for this work by deuterium charging electron beam evaporated Sc films in vacuum and at an elevated temperature in a proprietary method. During this process, film channel cracking occurred as the deuterium charged film was cooled to room temperature. Cracking in the film does not necessarily impact the performance of the films in a device, but if cracks propagate enough to spall or lose material on the substrate, this will limit film and device reliability [143]. To better predict the reliability of these films for device production, it is necessary to define the mechanical properties of the films for modeling efforts. However, mechanical properties of these films cannot be measured by traditional testing techniques due to the small thickness of the films. As a result, nanoindentation and micropillar testing are used to measure these small scale mechanical properties. Using these two testing methods will also provide some information

about how the material behaves in triaxial and uniaxial stress states. Micropillar testing is of interest because this testing targets size effects in the material by decreasing the probability of defects in the testing volume. In addition, this testing enables the study of yield and strain hardening data to understand plasticity behavior, and removes the residual stress in the material to more directly measure fracture toughness instead of depending on a model of thin film fracture.

First, the bulk film fracture was quantitatively defined by finding the temperature and estimating stresses for channel cracking of production-like ScD_2 thin films on fused silica through *in-situ* monitoring. The ScD_2 on fused silica substrates is a model system ideal for studying conditions for film cracking during processing since substrate processing is relatively simple and the entire fabrication process can be imaged through the substrate while the films remain in vacuum. While fracture can be observed through the fused silica substrates, the fracture toughness value calculated from these observations is based on a crude model and is not a direct mechanical measurement. Given the several uncertainties, elastic modulus, hardness, and fracture toughness were determined using nanoindentation and micropillar compression of ScD_2 films on polished molybdenum (Mo) substrates. Mo was chosen as it is a typical substrate for these devices in industrial applications. Micropillar fabrication through FIB milling, while alleviating the residual stresses from processing, provides samples for direct measurements of material fracture. Earlier studies have been completed on similar 150 nm thick ScD_2 films that focused on mechanical and chemical properties of precursor and processed films on fused silica as a function of aging [9]. In this work, the focus is more heavily on mechanical properties and fracture toughness

values of ScD_2 on a Mo substrate as a function of size. Three pillar sizes were chosen in attempt to investigate individual grains as well as grain boundary effects. There appears to be multiple modes of mechanical behavior in these films and these studies are the beginning of understanding the mechanisms behind these observations.

3.2 Sc Background

Before discussing ScD_2, Sc should also be discussed. Nilsen was credited with the discovery of the element Sc in the decomposition of minerals as documented in his 1879 publication [149]. However, not much insight was accomplished with the pure element due to the difficulty of finding and isolating large amounts of pure materials until the 1930-50's [150] and minimal studies have been completed on the mechanical properties of bulk Sc metal. Sc is known to have a close-packed hexagonal structure at room temperature, but can transform into a body-centered cubic structure at high temperatures [151]. In the case of impurities, Sc will form intermetallic phases with many other transition metal elements, but generally, solid solutions Sc or phases of $Sc+Sc_xM_y$ will form with moderate additions of impurities [152, 153, 154]. The bulk mechanical properties that have been previously determined that can be compared to the deuteride in the current study are: E = 75-80 GPa [155, 156, 157], microhardness for the (0001) plane = 130-210 HV [158], and yield strength = 130-170 MPa [156]. The variety in the mechanical properties are likely due to impurity content differences [150]. A film system has been reported by Kennedy et al that showed a depth dependence on hardness of Sc films on SiO_2/Si substrates from 2-6 GPa due to substrate effects [9].

3.3 Experimental Procedure

ScD$_2$ films were fabricated in a proprietary two-step process by others at Sandia National Laboratory, but will be summarized here. First, Sc films were electron beam evaporated onto polished Mo or fused silica substrates to a thickness of 2.5-3.0 µm. Sc films had some impurity content from the initial supplier; the films listed here have impurities around 100 ppm Al unless otherwise noted. The films were then thermally charged with deuterium to form ScD$_2$, and cooled to room temperature for testing. Cracking due to thermal misfit strains, as optically observed during cooling of the deuterium charged films, resulted in films comprised of networks of islands of material. This effect was particularly pronounced in films on fused silica substrates, where high thermal misfits led to higher relative film stresses compared to Mo substrates. Film fracture features were measured by SEM, and were used to determine residual stresses as described in Section 3.5. Nanoindentation using a Hysitron TI-900 Triboindenter with a Berkovich tip was used to characterize the films.

Micropillar compression involved testing multiple diameters of micropillars that were milled with an FEI Quanta 3D FIB following a similar procedure as first described by [137] and adapted to smaller pillar sizes by [138]. Pillars of 1600, 800, and 300 nm diameter were produced in attempt to control the number of grain boundaries in the x-y plane; 300 nm pillars should contain only one to two grains, while larger grains should contain multiple grain boundaries. All micropillars had an approximate height to diameter ratio of 2:1, though 1600nm pillar height was limited to approximately 2 µm to ensure that the pillar height did not include sections of the substrate. The micropillars had a slight taper of ~2°. Dimensions of micropillars before and after loading were determined from SEM

images of the micropillars before and after mechanical testing. Micropillars were tested *in-situ* with an SEM mounted Hysitron PI-85 PicoIndenter operating inside an FEI Versa FIB/SEM with a 3 μm flat punch indenter tip for most testing. However, *ex-situ* testing with a Hysitron TI-900 Triboindenter with a 5 μm conical tip was also completed. Strains of 5 to 40% were achieved.

3.4 Film Characterization

XRD data and EBSD maps with corresponding pole figures were taken on cross sections of the films. Together, this demonstrated that Sc films have a hexagonal structure with a very strong basal (0001) normal orientation and texture as seen in Figures 3.1 and 3.2. Cross sections of the Sc films have a mixture of (1010) and (11$\bar{2}$0) orientations. The grain size was near 400 nm.
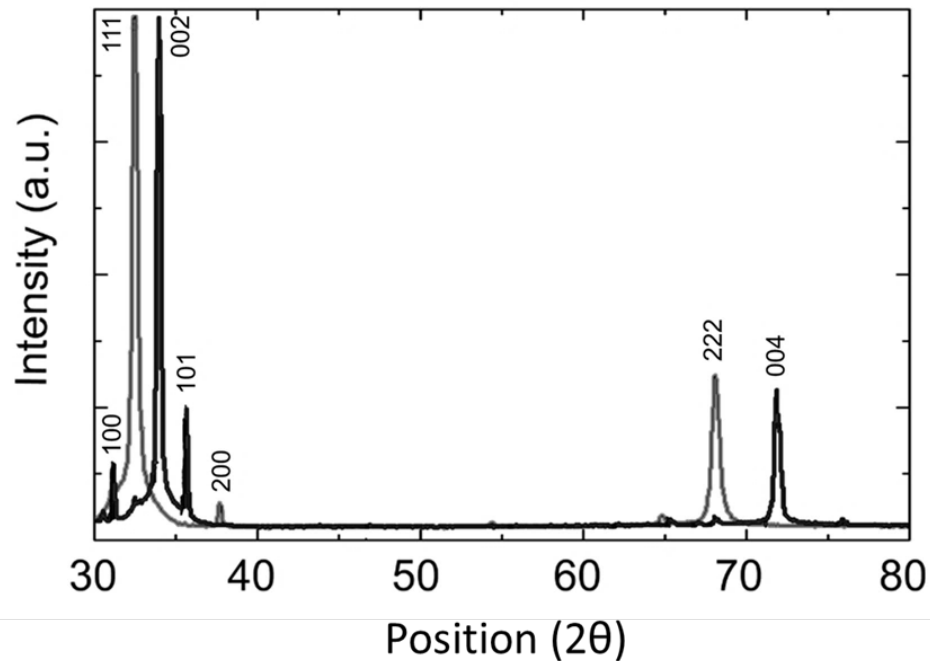
Figure 3.1: XRD of Sc (black) and ScD$_2$ (grey).
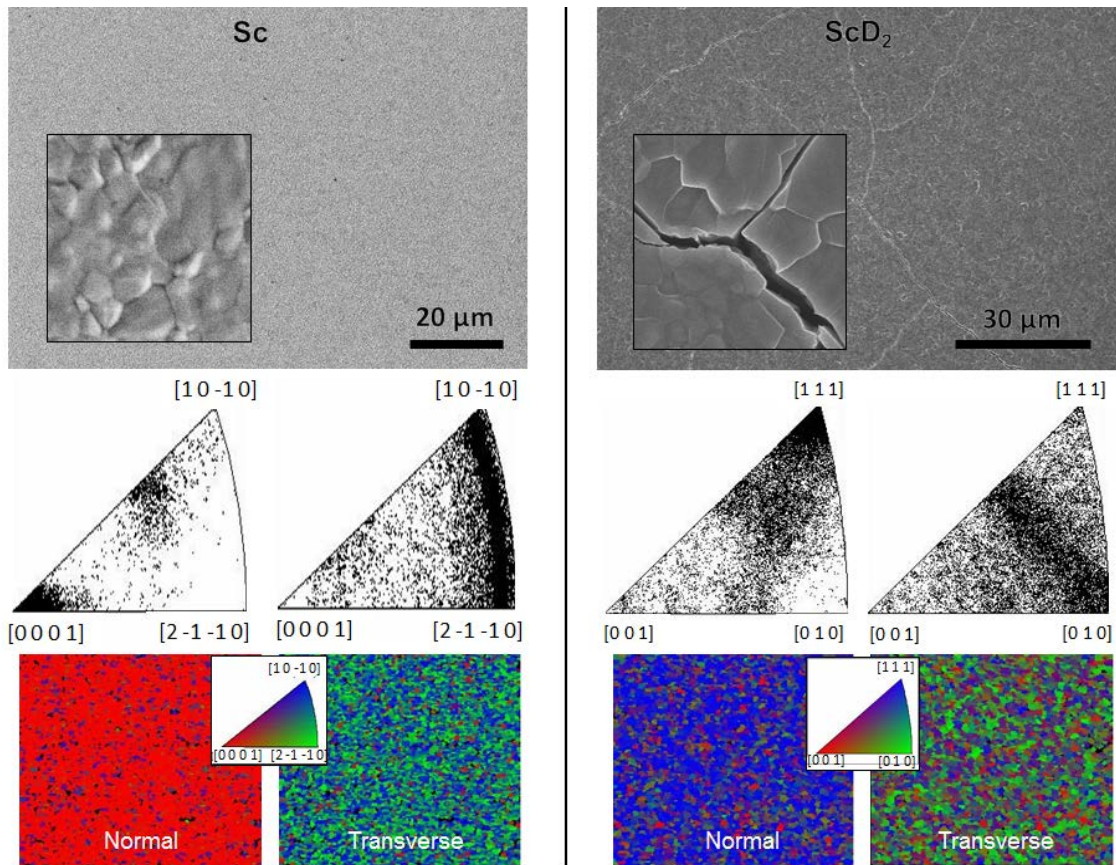
Figure 3.2: Sc (left) and ScD₂ (right). Top: SEM images of the films as well as magnified areas of the films showing morphology. Middle: Pole figures of normal and transverse directions of films. Bottom: EBSD images of normal and transverse directions of films with inverse pole figure legends.

Deuterium charging changed surface appearance and topography of the films while maintaining the small grain size microstructure. XRD, inverse pole figures and EBSD maps seen in Figures 3.1 and 3.2 showed that deuterium charging changed the Sc films from a hexagonal to an FCC-fluorite structure with a (111) normal orientation typical of hydrides and deuterides [88]. Transverse film directions had a mixture of (110), (100), and to a lesser degree (111) oriented grains. These results indicate that most if not all of the Sc is transformed into ScD₂ during the charging process as there are no indications that the Sc remains in the areas investigated with EBSD. The deuterium charging process also lead to

a surface oxide thickness increase of approximately 17 nm, determined from where the composition of O was less than 10 at%, from the originally deposited Sc as shown in Figure 3.3. These measurements were taken by scanning Auger microscopy (SAM), a characterization technique that uses an electron beam to generate Auger electrons that are used to determine the elemental composition of the surface of a material [136]. This material is depth sensing by destructively milling away part of the material and repeating
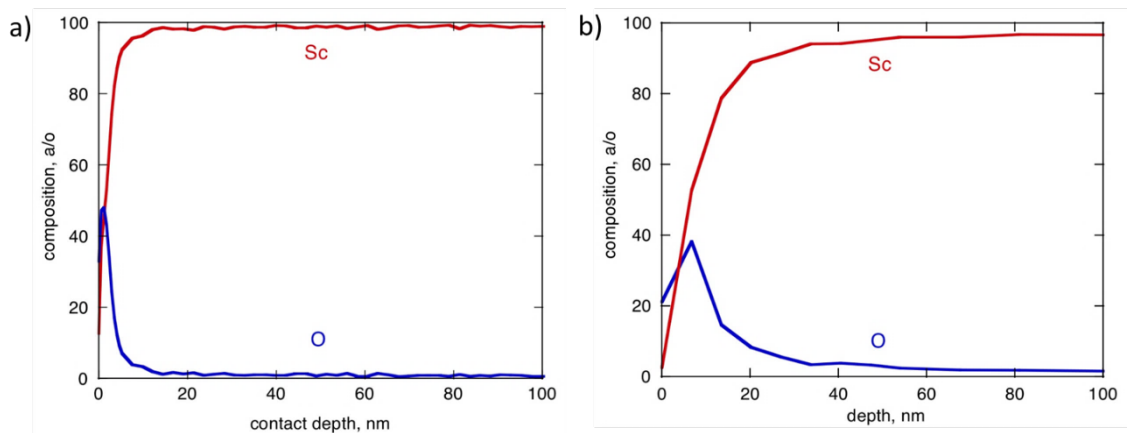
Figure 3.3: a) Sc and b) ScD₂ SAM measurements of Sc and O composition used to determine oxide thickness.

the scans. As previously shown, the heat treatment of the films increased the depth over which surface hardening occurred in nanoindentation, but should not impact through-thickness film properties in nanoindentation [9].

Nanoindentation was used to determine hardness and elastic modulus of the Sc and ScD_2 films. The indentation size effect, seen at low contact depths and discussed in Chapter 2, are apparent in all datasets and were not removed to show all data collected. Tests using a Berkovich tip and investigating films on fused silica substrates established that as-deposited Sc films which have a modulus and hardness near 55 GPa and 2 GPa respectively, see Figure 3.4. The Sc films reported here were provided by Dr. N. Moody at

Sandia National Laboratories; the S10 and S12 films were deposited on fused silica substrates and had thicknesses of 3 and 4 µm respectively. All the films here have small
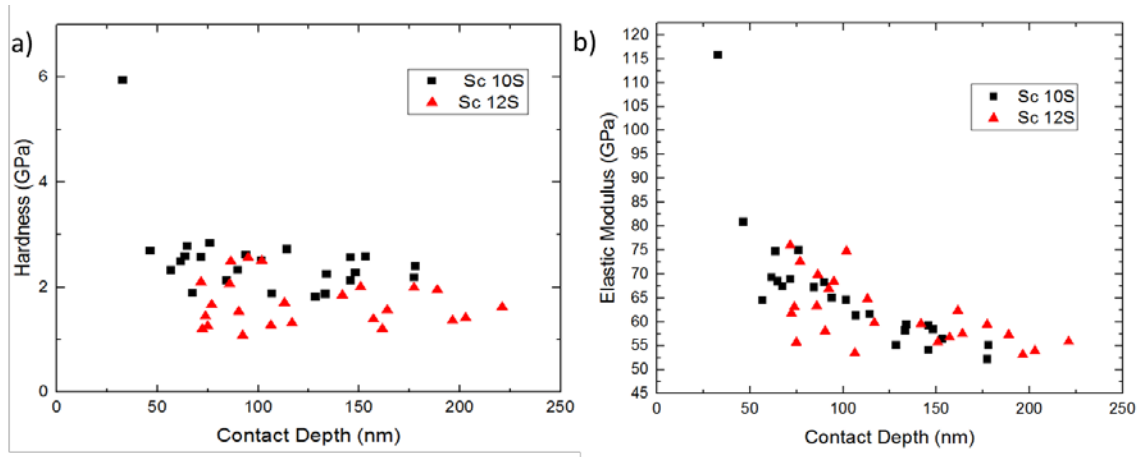
Figure 3.4: a) Hardness and b) elastic modulus of electron beam evaporated Sc films 3 µm (10S) and 4 µm (12S) thick on polished fused silica substrates.

impurities of aluminum. The reported modulus values for Sc are somewhat lower than that reported in bulk studies, but are likely impacted by differences in impurities as well as grain size and texture [150], which are not necessarily reported in the other bulk studies found here. The hardness of the films has a scatter band larger than expected for nanoindentation data; this is partially due to the surface roughness of the material and grain orientation variation. Since these films are formed by electron beam evaporation, surface features will result from the deposition process that cannot be removed via polishing techniques because of the small thickness of the films. The differences in these film thicknesses should not affect hardness measurements at these contact depths, as normally contact depths that only probe ~10% of the film thickness have minimal substrate effects [127]. The hardness differences observed in the two thickness films are likely a result of run to run variation observed in production and potential orientation sampling variances. As seen in the EBSD maps, there are approximately three grain orientations that are probed

60

in the films. However, due to the surface roughness of the films mechanically tested, EBSD

cannot be completed.
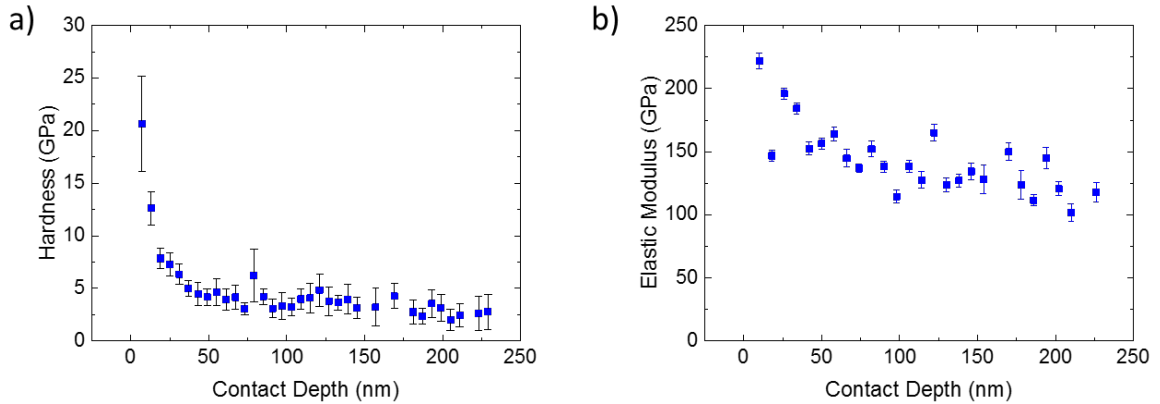
Figure 3.5: a) Hardness and b) elastic modulus of ScD₂ films on fused silica substrate, with 100 ppm Al impurities.

ScD₂ films had a higher modulus (150 GPa) and hardness (4 GPa) than the tested Sc

films, as expected. This can be compared in Figures 3.4 and 3.5. These measurements are

in general agreement with similar systems as reported by Wu et al. [159]. ScD₂ films on

Mo substrates were also tested with nanoindentation, and resulted in similar values for

modulus and hardness as shown in Figure 3.6. The hardness in Figure 3.6 are higher than
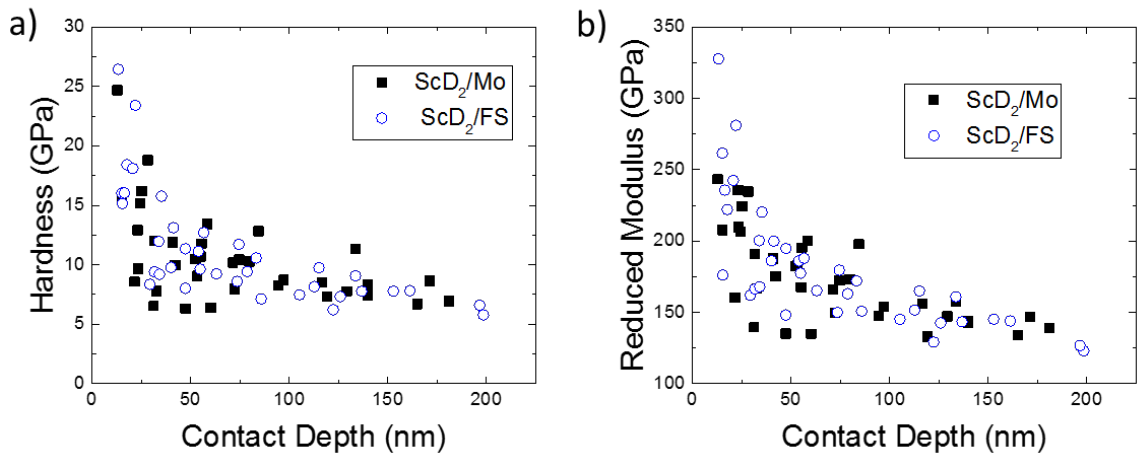
Figure 3.6: a) Hardness and b) reduced modulus of ScD₂ films on Mo and fused silica (FS) substrates using a blunt Berkovich tip.

the other values reported throughout this document and are thought to be artificially higher due to the use of an alternative Berkovich tip, different than the rest of the tips used through this work. In attempt to relate these properties to bulk values, hardness is related to the bulk yield stresses of a material – typically the empirical relation is $H/3$ [130, 131]. The yield stress found through nanoindentation is about 1.3 GPa in ScD_2 and 670 MPa in Sc. The Sc values are about 4 times higher here than reported in bulk specimens. Overall, the deuterium charging process increases the yield strength in the Sc material.

The impacts of impurities on the elastic modulus and hardness of the ScD_2 films were also investigated. As previously stated, these impurities come from the source material for the Sc films, where aluminum is somewhat difficult to remove from Sc. Four impurity contents were provided by Sandia National Laboratories: 100, 1000, 10000, and 50000 ppm Al. Impurity content had minimal impact on the modulus of the material, but had a slightly higher impact on hardness, where larger impurity content lead to harder overall films, though the two highest and two lowest impurity contents are very similar to one
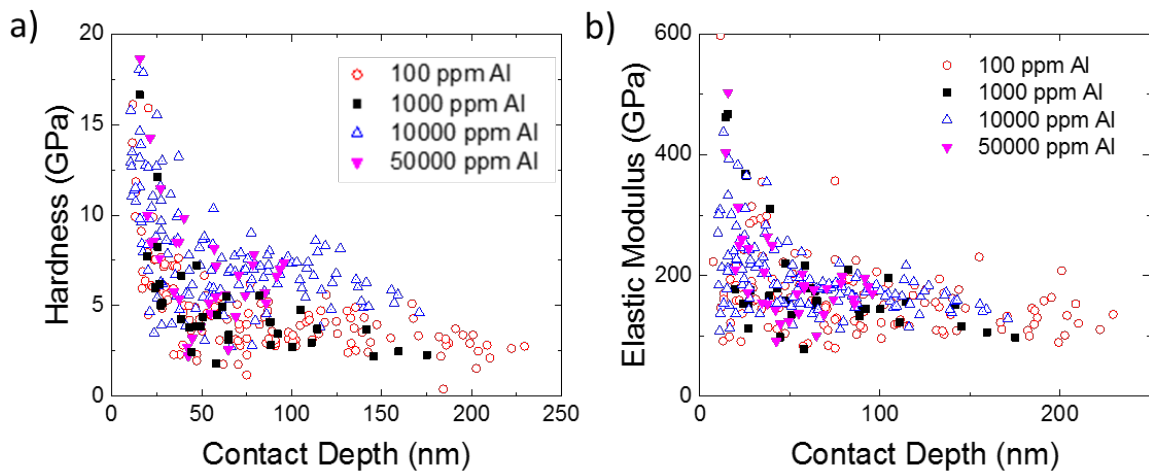
Figure 3.7: Impurity impacts on a) hardness and b) elastic modulus of ScD2 films on quartz substrates.

another, as shown in Figure 3.7. This is typical of many systems where solid solution and/or increasing precipitation of other phases increases the hardness of the material but has minimal impacts on the bulk-bond structure of materials [13].

In all cases of nanoindentation, there were some film to film variation of modulus and hardness, particularly in different production runs. Regardless, no obvious fracture was observed during nanoindentation for films on either substrate. Instead, bulk film features, namely island formation, and micropillar compression were used to make estimations of fracture toughness. In addition, it should also be noted that a small indentation size effect, where hardness slowly decreases with increases in contact depth [44], is apparent in all of the hardness nanoindentation data provided in this section. Also, the initial data reported at low contact depths showing much larger modulus and hardness values, is an artifact associated with improper tip-area function measurements as well as contact issues between tip and the sample surface. These contact issues are due mainly to the surface texture of the ScD_2 films that could not be removed by polishing due to the small film thickness – the data reported in the text reflect the converged values for material property determination.

3.5 Film Cracking

Fused silica substrate systems were used to determine the fracture properties of films during the deuterium charging process as the film could be optically imaged through the substrate. The original Sc films exhibited compressive stresses, however film stresses became tensile after thermal charging as determined through film curvature changes. This indicates that deuterium expands the lattice of the initial Sc film. This is expected as the lattice change from Sc (a = 3.30 Å, c = 5.27 Å) [160] to ScH_2 (a = 4.783 Å) [161] is an

increase of approximately 2.4%. Film cracking occurred during cooldown of the films following deuterium charging, at ~180°C below the processing temperature. Subsequently, additional cracks formed and further subdivided the film into an island-like structure until cooling to ~200°C below the processing temperature. Large scale delamination or spalling was not observed. An example film showing cracking is seen in Figures 3.2 and 3.8a. While some transgranular fracture did occur, intragranular fracture was by far more prevalent on the films' top surfaces. This is likely a result of grain orientation differences as well as texture resulting from deposition introducing additional defect sites.

Since the main channel cracks formed upon film cooling, an estimation of fracture toughness can be made using film crack geometry, see Figure 3.8b for the relevant parameters needed for a calculation. To quantitatively estimate the fracture toughness
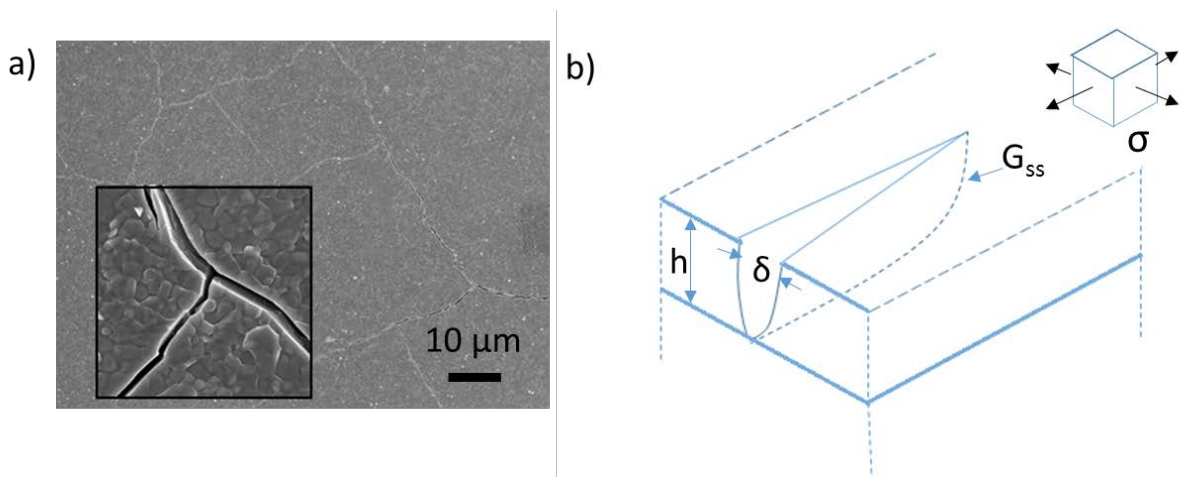
Figure 3.8 a) Example of ScD$_2$ film channel cracking showing examples of island size and b) model of channel cracking showing relevant parameters adapted from Reference **[163]***.*

associated with the films, film fracture was investigated as a growing, through thickness channel crack. Beuth [162] developed this analysis originally proposed by Hutchinson and Suo [163] that looks at the change in energy in a slice of material far ahead versus far

behind a crack tip in a thin film on a substrate geometry. This estimate accounts for the mixed fracture modes associated with channel cracking by finding the steady state strain energy release rate using the following equation [162, 163]:

$$G_{ss} = \frac{\sigma_R^2 h (1 - v_f^2) \pi \cdot g(\alpha, \beta)}{2E_f}.$$

3.3

Above, E_f is the elastic modulus of the film estimated as 150 GPa from nanoindentation, σ_R is the residual stress, v_f is the Poisson's ratio of the film here taken as 0.25 as is typical of hydrides, h is the film thickness, and g is a function of the Dundurs parameters which account for the elastic mismatch in film and substrate where $\alpha \sim 0.24$ and $\beta \sim \alpha/4$, giving *g(α, β) ~1.54* [162].

Two approaches were used to estimate the residual stress in the films to input in Eq. 3.3: a thermal stress and a crack width approach. Since the first network of channel cracks formed spontaneously on cooling $\sim 200°C$, an approach which accounts for differences in film and substrate thermal expansion can provide one estimate for overall film fracture toughness. The thermal residual stress was determined using [164]:

$$\sigma_R = \frac{(\alpha_f - \alpha_s) \Delta T \cdot E_f}{(1 - v_f)}.$$

3.4

Here α is the thermal expansion coefficient denoted by subscripts for the film (f) and substrate (s), and ΔT is the change in temperature. $\alpha_f = 14.5$-15.4 μm/m-°C for ScH_2 [165] and $\alpha_s = 0.4$-0.6 μm/m-°C for fused silica [166]. Using these values and Equation 3.3, the residual stress was determined to be 370-400 MPa. The residual stress range inserted into Equation 3.3 gives $G_{ss} = 6.2$-7.3 J/m^2, resulting in a mode I fracture toughness, K_{IC}, of 0.96-1.1 MPa-m$^{1/2}$.

The second way to estimate the residual stress relevant to channel cracking is to use crack geometry measurements at room temperature. These measurements can provide an upper bound estimate for film residual stress using:

$$\varepsilon = \frac{\delta}{d},$$ 3.5

$$\text{and } \sigma_R \approx \frac{\varepsilon \cdot E_f}{(1-\nu_f)}.$$ 3.6

Here, δ is the crack width, d is the island size. These factors are 100 nm and 27 µm for fused silica substrates. Here, the residual stress used a plane strain approximation and was determined to be 730±280 MPa. This results in $G_{ss} \approx 24.2$ J/m^2 and $K_{IC} = 1.9 \pm 0.7$ MPa-m$^{1/2}$.

Fracture toughness values for films with a fused silica substrate vary by a factor of two but show that the film is tougher than typical values for glass, and fall in a similar range as ceramics. For Mo substrates, the fracture toughness could not be accurately determined through these methods as there is a relative higher cohesion between film and substrate that is thought to constrain crack opening and the smaller differences in thermal expansion coefficients led to smaller residual stresses in the films and less cracking. Further work was done with micropillar compression to determine elastic, plastic, and fracture properties systematically to characterize the film properties.

3.6 Micropillar Modulus, Size Effects, and Fracture

Micropillars of ScD$_2$ were tested in compression and showed two main modes of behavior: plastic deformation and cracking, though some pillars showed mixed modes of behavior as shown in Figures 3.15 and 3.17. This indicated that this material has a DBT. First, pillars that exhibited no fracture indications were used to determine elastic modulus

and hardening effects. Following this, pillars that cracked during testing were used to determine fracture toughness.

Following the work of Greer, et al. and Singh, et al. [167, 168] and summarized in work by Fei, et al. [169] the unloading portion of the stress strain tests of the micropillars were used to determine the elastic modulus of ScD_2. However, instead of calculating change in contact diameter with increasing plastic displacement the actual height and contact diameter measurements of the unloaded deformed pillars were used. Pillar taper effects and underlying material effects were considered by using a modified version of Reference [168] where compliance is adjusted to account for Sneddon's criterion, commonly used to account for compliance of material underneath the pillar:

$$E = \frac{PL_o}{\pi(C - C_{Sneddon})d_o(d_o + L_o \sin\theta)}. \tag{3.7}$$

$$\text{where } C_{Sneddon} = \frac{\sqrt{\pi}(1 - v_s^2)}{2E_s\sqrt{A_p}}. \tag{3.8}$$

Here, P is the maximum load for the test, d_o is the unloaded deformed pillar diameter, L_o is the original, unloaded pillar height, C is the measured compliance, θ is the angle of taper for the unloaded deformed pillar, E_s is the elastic modulus of the substrate, and A_p is the pillar-top area under load.

Results for the E_f calculations can be seen in Figure 3.9. With closer examination, this suggests values for E_f are inaccurate at low displacements, likely due to pillar-tip contact, but could be partially due to the anisotropy of the fluorite structure. Though, some scatter in the modulus measurements is expected as pillar-tip contact, misalignment, crystal orientation, and pillar geometry variations. These error sources are consistent with the

variance of the load displacement curves from ideal elastic loading conditions and the issues with determining modulus via micropillar testing [169]. Despite these potential error sources, the elastic modulus micropillar data are close to the elastic modulus as determined by nanoindentation as shown as the horizontal line on Fig. 3.9.

Yield stress was determined for the micropillars by using a 0.2% strain offset. There is a large amount of scatter in this data, as is typical in micropillar samples where geometry
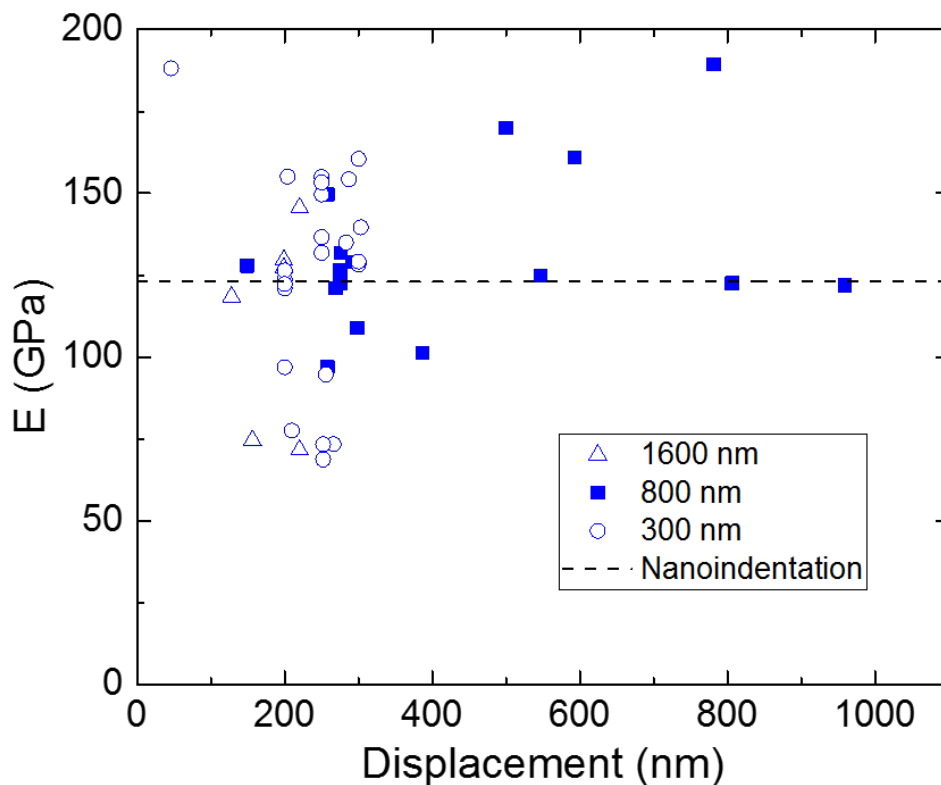
Figure 3.9: Elastic modulus measurements of ScD₂ micropillars of various diameters using C_Sneddon correction and a right circular cylinder approximation. The average modulus value for nanoindentation is overlaid on the plot for comparison.

and tip-pillar contact variance occurs [170]. However, it becomes obvious that the smallest diameter pillars have the highest yield stress. This is likely a consequence of single crystal versus multiple crystal testing volumes [171]. However, all of the yield stresses reported here are about an order of magnitude higher than those reported in Sc metal.

68

Table 3.1: Yield stress and standard deviation of three diameters of ScD$_2$ micropillars.

Pillar Diameter (μm)		Yield Stress (MPa)	
Average	Standard Deviation	Average	Standard Deviation
0.28	0.02	2000	380
0.83	0.02	1100	310
1.65	0.02	1200	260
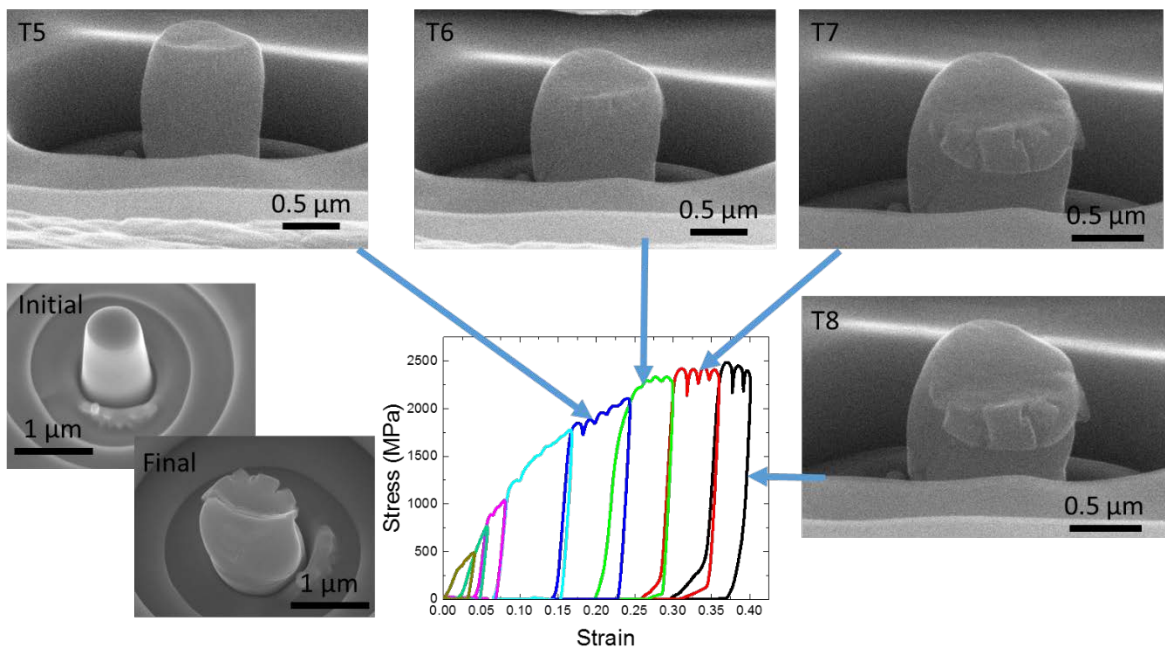
Figure 3.10 Multiply loaded ScD$_2$ micropillar, showing SEM images of the initial pillar and the final pillar morphology at 25° tilt, as well as post-test images starting at test 5 (T5), where eccentric loading began at a 15° tilt.

The plasticity of the micropillars was also investigated, focusing on pillars that showed no fracture indications. Some of the ScD$_2$ micropillars also showed a large amount of ductility, even after multiple loading. One case, where a micropillar was tested seven times, reached an overall strain of 20% without cracking. After this, tip misalignment led to gradient stresses and cracking in the micropillar, but led to an overall strain of 40%
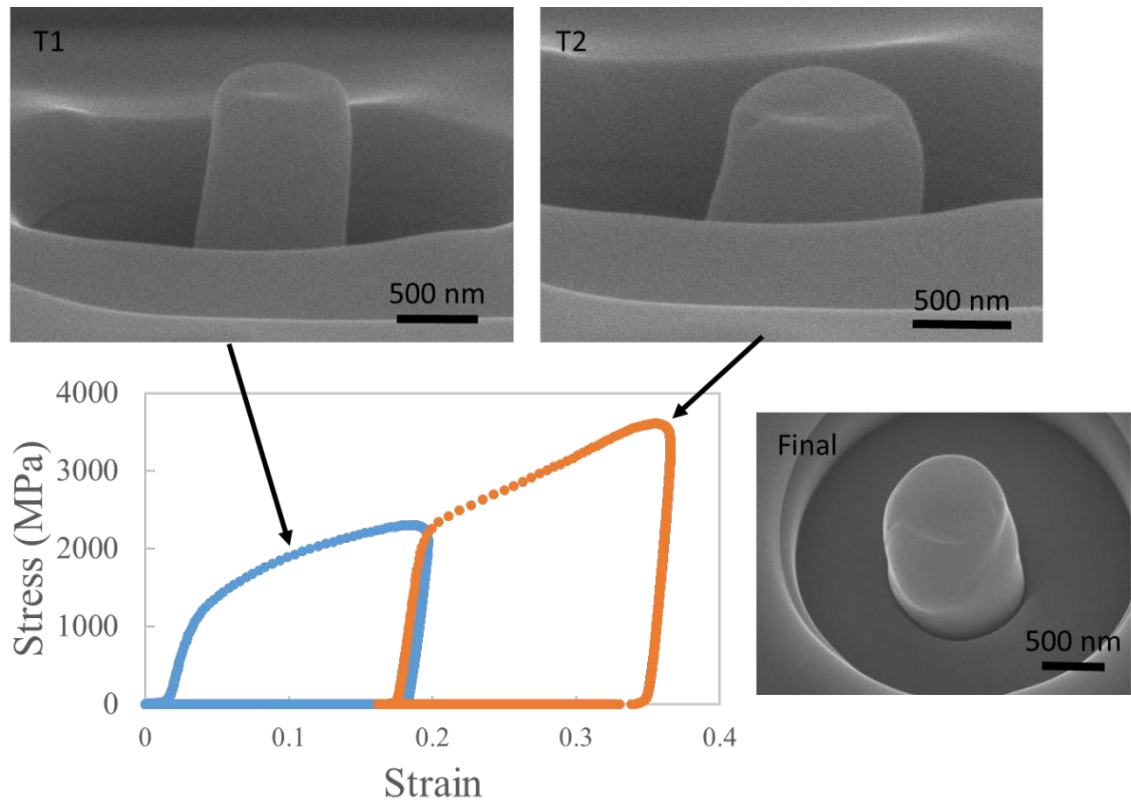
Figure 3.11: Twice loaded 800 nm diameter ScD2 pillar. SEM images for each test number (T#) at a 15° tilt are shown with the complimentary stress-strain curve; the final pillar image is at a 25° tilt.

without catastrophic failure as shown in Figure 3.10, where large load drops are indicative

of cracking or crack propagation events and could also be indicative of some plastic flow.

Part of the apparent increase of plasticity in this sample is due to crack formation, seen in

some videos and in final SEM images, resulting in additional displacement. However, the

most interesting thing to come out of the multiply loaded pillars is that a minimal amount

of fracture occurred with strains up to 35%. These multiple loading and unloading events

lead to enhanced dislocation multiplication, as observed in nanoindentation [172], and are

one potential source for the increased plasticity observed. An example of this behavior is

shown in Figure 3.11, where an 800 nm diameter pillar was loaded twice to a total strain

of 35% without fracture, but some bulging and slip occurred. TEM liftouts of the pillar could be used to investigate this further.

To examine more typical pillar behavior, flow stress was examined in all pillar sizes, revealing a size effect where smaller pillars exhibited higher relative stresses, as shown in Figure 3.12 for micropillars tested *ex-situ*. Initial portions of stress strain curves for the larger pillars were impacted by contact issues: based on chord lengths, a minimum contact depth of at least 64 nm is needed before full pillar-tip contact. Qualitatively the 300
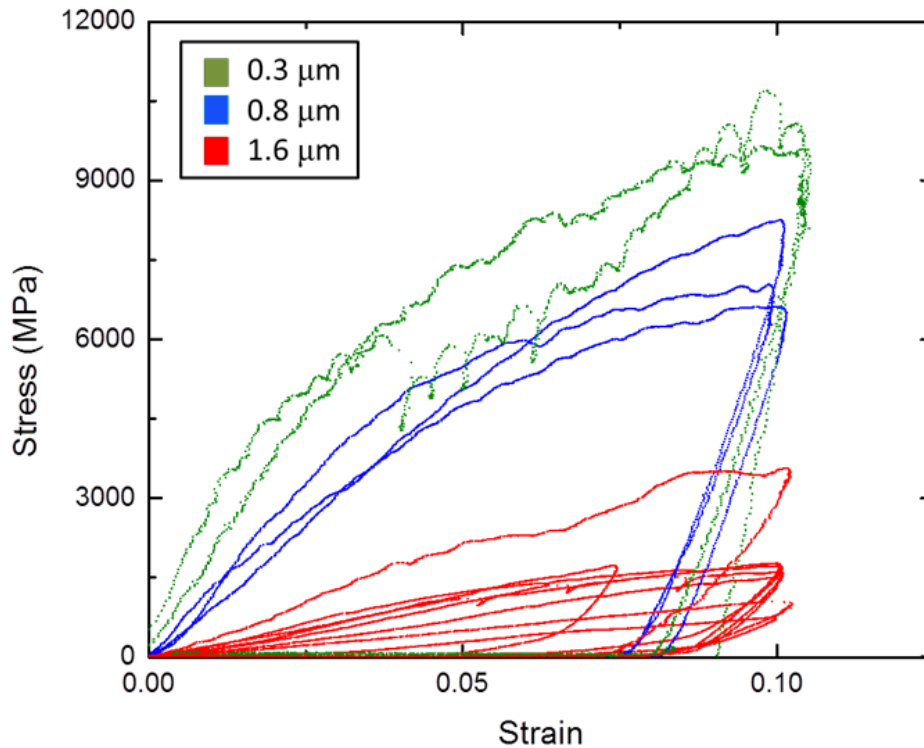
Figure 3.12: Diameter dependence on ScD$_2$ micropillar stress-strain behavior for ex-situ tested samples. These data are representative of pillar behavior but were not analyzed for toughness, hardening, or fracture tests further reported.

nm pillars have more dislocation avalanches, seen in the load drops in the loading curve. It should also be noted that 38%, the smallest percentage of this pillar size tested here, had signs of fracture in post SEM images. This is likely due to a combination of dislocation

71

starvation and higher flow stresses being able to nucleate alternative dislocation nucleation sites from the pillar surfaces as well as these samples being single crystalline. In attempt to quantitatively compare pillars tested *in-situ*, pillar flow stresses were determined at 8% strain across all sizes to minimize possible contact issues. There is a moderate size dependence determined, with smaller pillars having higher relative stresses at the same given strain as shown in Figure 3.12 and 3.14a.
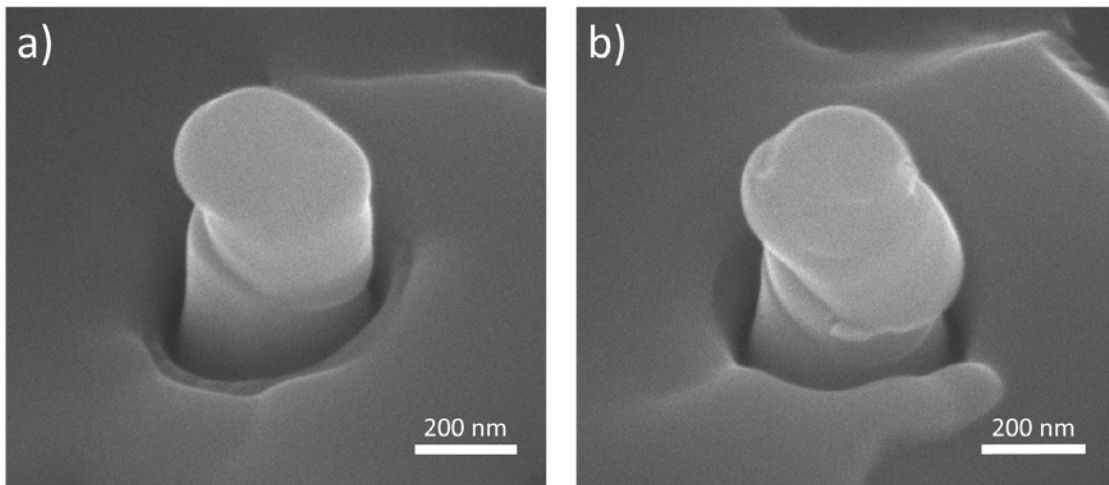
Figure 3.13: 300 nm diameter pillars of ScD₂ examples of a) slip and b) mixed slip and fracture behavior.

ScD$_2$ is expected to slip on (100)[110] like other fluorite crystals [144]. The best examples of slip are seen in the 300 nm diameter pillars, shown in Figure 3.13. These pillars are expected to be individual grains, and larger pillars are not expected to show such obvious slip patterns due to multiple orientations of slip. Deformation in these crystal structures is typically dominated by the Peierls mechanism at low temperatures. To estimate the stress, τ_p, required to activate a dislocation, a simplified Peierls model was used [20]:

$$\frac{\tau_P}{G} = \frac{2}{1-v} exp^{\frac{-2\pi a}{(1-v)*b}},$$ 3.9

where G is the shear modulus, b is the Burgers vector and a is the distance between slip planes. Here, $\frac{\tau_P}{G} \approx 3*10^{-3}$. Using the bulk modulus of ScH_2 to estimate G [173] , $\tau_p \sim 175$ MPa, and is well below the stresses calculated in the micropillars during testing. While the Peierls mechanism is likely the main proponent of initial plasticity in these samples, hardening was apparent after yielding and full pillar contact.
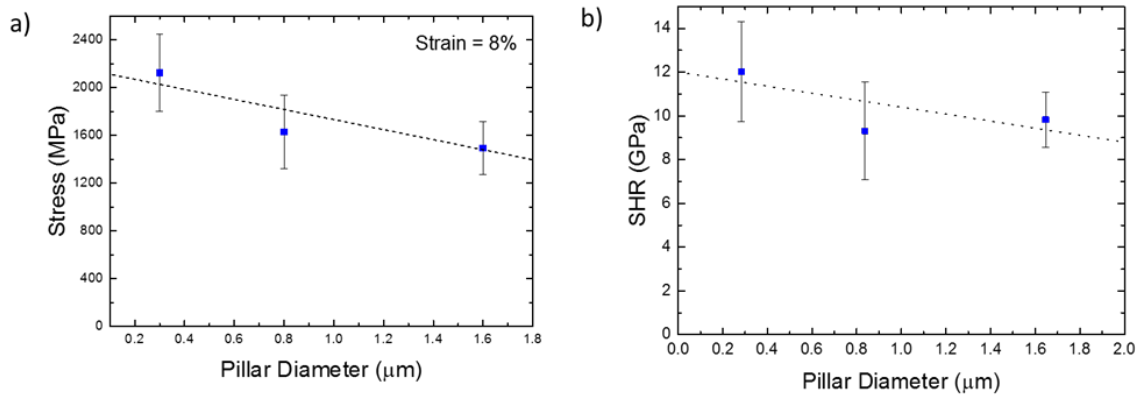
Figure 3.14: a) Flow stress at 8% strain and b) strain hardening rate (SHR) for multiple diameters of ScD₂ micropillars.

To quantify hardening behavior, the strain hardening rate (SHR), $\Delta\sigma_{true}/\Delta\varepsilon_{true}$, was calculated from *in-situ* tests; results are found in Figure 3.14b. The SHR decreased as pillar size increased, indicating that smaller pillars harden more readily than larger pillars. This is consistent with dislocation exhaustion – that smaller pillars are likely to have mobile dislocations terminate at the pillar surfaces, leading to increased hardening relative to the larger pillars [174]. It should be noted here that grain size is likely a factor in the size dependence observed. Larger pillars are also more likely to have grain boundaries, leading to a larger number of overall dislocation nucleation sites and traps as well as a potential to

create a larger internal stress near grain boundaries. This should also lead to larger probability of fracture in larger pillars, as there should be a higher number of defects per volume due to grain boundaries. Future TEM studies should confirm this speculation, though this argument is consistent with other authors [174, 175, 176, 45].
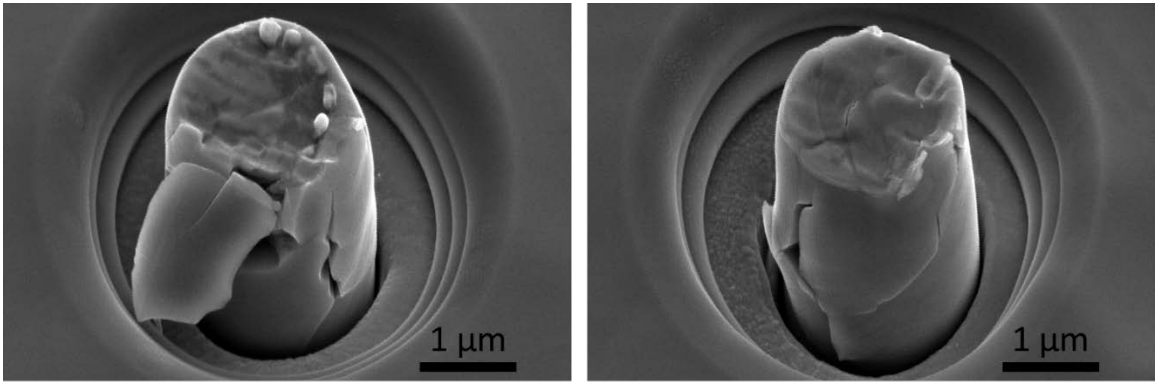
Figure 3.15: SEM of vertical crack formation as well as plastic deformation in two different, 1.6 μm diameter ScD$_2$ micropillars.

While all pillars showed some plasticity, some micropillars also fractured during loading. To further complicate the fracture behavior of this material, some pillars showed significant plastic deformation before fracture. Two examples of this mixed behavior are shown in Figure 3.15, where fracture occurred after deformation, as evidenced though *in-situ* monitoring. This mixed behavior is likely a result of strain localization in the pillars due to the taper of the pillars [177]. The most interesting observations are the vertical cracks that were formed during testing, which has also been observed in other work [46, 178]. It is possible that vertical cracks can form as slip intersects with defects such as grain boundaries as postulated by Hoek [179] and Moser, et al [80]. Examples of vertical cracks are seen in Figures 3.15 and 3.17.
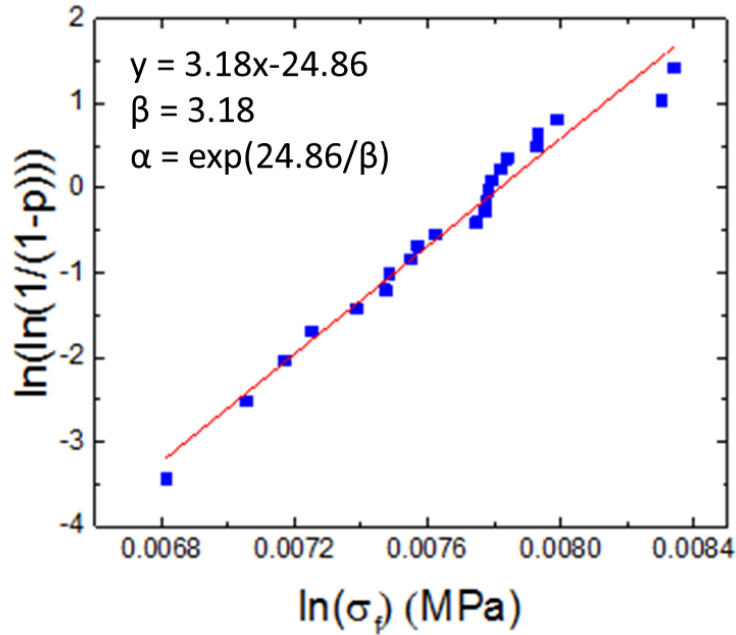
Figure 3.16: Weibull parameter determination for fractured 300 nm diameter ScD₂ micropillars.

Fracture probabilities of the micropillars were determined using two-parameter, cumulative Weibull distributions of normal fracture stress based on average pillar diameter with the following equation [180, 181]:

$$F(\sigma) = 1 - exp^{-\left(\frac{\sigma}{\alpha}\right)^{\beta}},$$ 3.10

where, $F(\sigma)$ is the fracture probability at a given stress, α is a scale parameter, and β is a shape parameter. The fracture probability here is defined as any fracture event, whether it be corner crack initiation or catastrophic pillar failure. The parameters α and β are found by plotting $ln(\sigma)$ versus $ln(ln(1/(1-p)))$, where p is the empirical distribution function [180, 181]:

$$p = \frac{i - 0.3}{n + 0.4},$$ 3.11

with i the rank of observation, or the sample number of failure stress in increasing order, and n being the total sample population. A linear regression of the above relationship is used to find β, the slope of this plot, and α, exp(y-intercept/β). See Figure 3.16 for an example plot for Weibull parameter calculations. Generally, a minimum sample size of 30 is required for Weibull plots [181]. In these experiments, ten, ten, and twenty-two samples fractured in 0.3, 0.8, and 1.6 μm diameter pillars, respectively. Regardless, this does indicate that fracture evolution is dependent on relative pillar diameter and is also likely related to grain size. As seen in Figure 3.17c, the 0.3 μm pillars have smaller probabilities of fracture at a given stress. However, it is unexpected that the 0.8 μm pillars show a higher probability of fracture at a given stress than the 1.6 μm pillars. The parameters of the Weibull distributions may shed light on this as the 800 nm pillar have the lowest α parameter of 1756 MPa, and highest β parameter of 6. It likely indicates that 800 nm pillars have a lower characteristic strength based on α which may indicate that the flaw sizes here are larger than the other pillar sizes [182]. Values of α and β are 2490 MPa and 3.2 for 300 nm pillars and 2100 MPa and 5 for 1.6 μm pillars, respectively. It should be noted that larger pillars had higher relative percentage of failure in the sample size given, 80% of the 1.6 μm pillars versus 46% of the 0.8 μm pillars fractured during testing. Weibull statistics of failure are limited in bulk metal hydrides, but it is likely that bulk hydrides fail at stresses less than 1 GPa, such as observed in lithium hydride [183], titanium hydride [144], and zirconium hydride [148]. It is still likely that the material's high surface area relative to volume enhances the plasticity observed here, particularly in the 0.3 μm case where it is likely that single-crystal volumes of ScD_2 limit fracture.
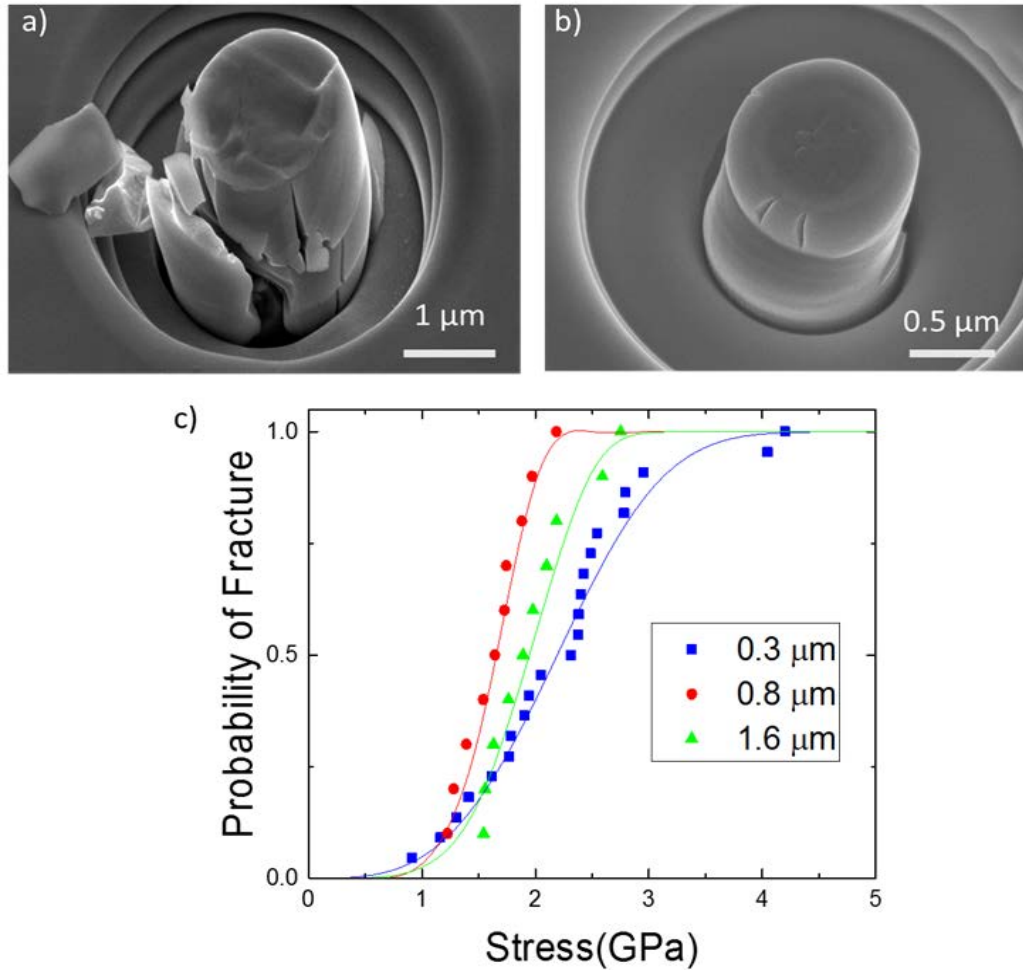
Figure 3.17: a) and b) showing mixed modes of plastic deformation and fracture in micropillar compression tests where plastic deformation was followed by extensive to minor cracking in the micropillars; c) Weibull statistics for probability of fracture versus stress in three micropillar diameters.

After the Weibull parameters analysis, an investigation of the toughness of the material was pursued. This analysis, finding the area underneath the stress strain curve using Origin, was completed for all pillar sizes, as seen in Figure 3.18. It should be noted the Weibull statistics from micropillars were taken to various strains with various strain rates even though there are no obvious trends that relate strain rate to fracture stress. These
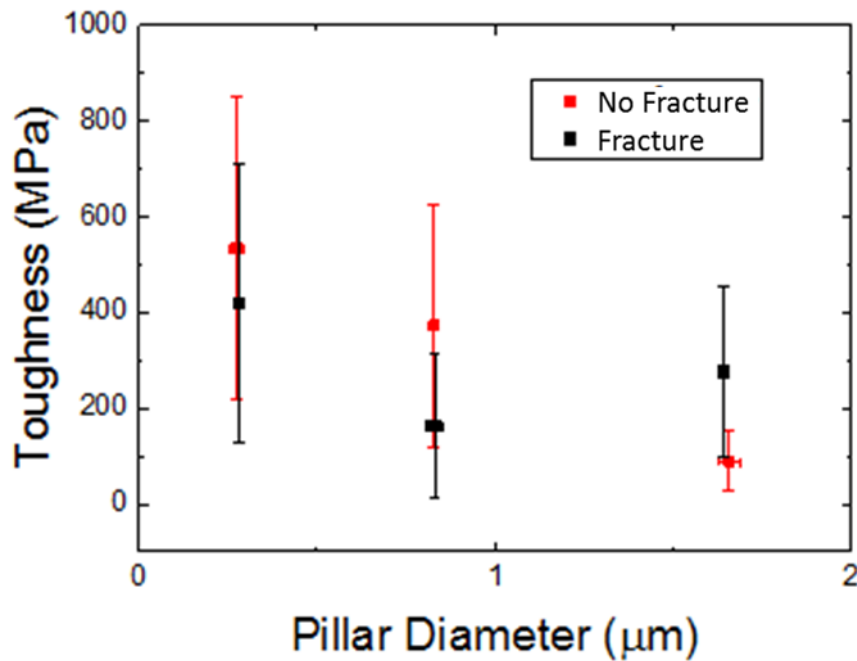
Figure 3.18: Toughness values for all tested ScD$_2$ micropillars with one standard deviation error bars.

statistics could be greatly improved by testing samples by using consistent strain rates for testing. However, in the specimens that only plastically deformed, the toughness is arguably larger for smaller pillar diameters. It is also interesting that the mean toughness of the 300 and 800 nm diameter pillars is lower for fractured specimens than the plastically deformed specimens. This could be a result of these pillars having a higher number of grain boundaries that are oriented for easier fracture, but the small sample size could skew this data. In addition, most of the 800 nm pillars that were primarily used for this work were tested multiple times, and introducing dislocations into the material appears to promote plasticity relative to single-tested specimens. This is experimentally shown by the multiply tested pillars had less fracture and larger overall strain. The questions that still arise from this data are why do the 800 nm diameter pillars fail at higher rates and have lower

78

toughness values than the 1600 nm diameter pillars? The best explanations are that this data has a small sample size that does not reflect the true nature of the material or the 800 nm diameter pillars have more grain boundaries oriented for easier fracture than the other pillar sizes. A zeroth-order estimate of grain boundaries to outer surface area shows that the 800 nm have the smallest surface area to number of grains in an average volume. This indicates that perhaps there is less surface area for dislocation termination and thus a larger chance for higher dislocation back stresses. However, 1600 nm diameter pillars are more likely to contain internal grain boundaries, which should further exacerbate this problem. The other thing to note here is that the 1600 nm diameter pillars showing only plastic deformation have the lowest toughness values than all of the other reported categories. This is due to user input as the samples that did not fail were taken to lower overall strains than the other specimens that fractured. These results leave room for improvements and extension of the experiments to further characterize this material, as explained in Chapter 6.
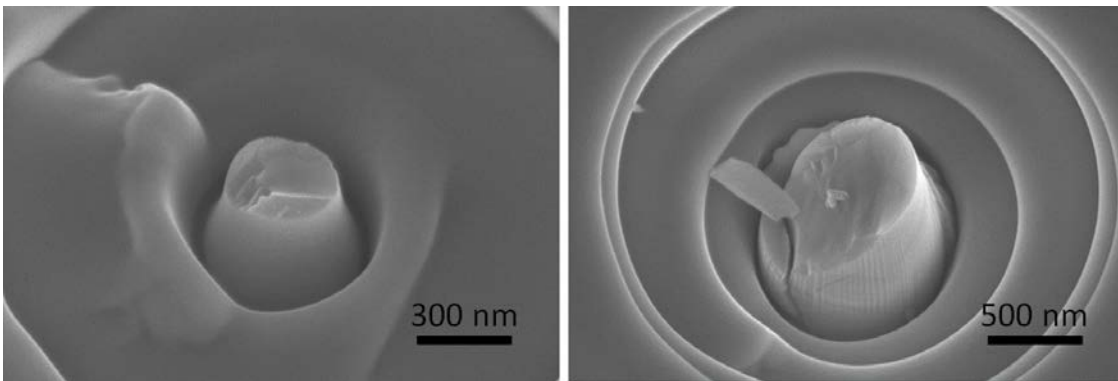
Figure 3.19: Catastrophically failed micropillars of ScD$_2$ with varying fracture surface angle.

Despite the mixed mechanical behavior of the ScD$_2$ micropillars, cracking typically emanated from the top edges of the pillar where the stresses and plastic strains are largest

due to pillar taper. With increasing load, cracking preferentially occurred across the sample into through-thickness wedge cracks that split the pillars, see Figure 3.18. Most of these cracks follow the same orientation as the channel cracks, approximately perpendicular to the substrate. However, some of the pillars, particularly where large sections of the pillars were missing or dislodged after testing, had fracture surfaces ~45-50° relative to the substrate. Catastrophic failure, where large sections of the micropillar were destroyed and missing after testing also occurred, and large variation in fracture planes occurred. Two extreme cases of this behavior are shown in Figure 3.19, where there is almost a 45° and almost flat fracture surface. Transgranular and intergranular cracking fracture surfaces were both observed based on the texture of the fracture surfaces.

While there are no explicit analytical solutions for fracture toughness from corner cracking or wedge or through-thickness cracking in cylindrical micropillars, there are solutions for crack growth in square beams. The following equations were applied to these tests by examining the largest cracks in each of the fractured samples. Examples of pillar fracture and schematics for the analysis methods can be seen in Figure 3.20. Tada provides the solution for fracture toughness for a corner crack in a square beam under uniform stress as [184]:

$$K_{Ia} = \frac{2}{\pi} \sigma \sqrt{\pi a} \cdot F_Q(\theta), \text{ where} \tag{3.12}$$

$$F_Q(\theta) = F(\theta) \cdot F\left(\frac{\pi}{2} - \theta\right), \text{and} \tag{3.13}$$

$$F(\theta) = 1.211 - 0.186\sqrt{\sin\theta}, \text{giving} \tag{3.14}$$

$$F_Q(\theta) = \left(1.211 - 0.186\sqrt{\sin\theta}\right)\left(1.211 - 0.186\sqrt{\cos\theta}\right). \tag{3.15}$$

Where a is the crack length, σ is the stress of the pillar, and θ is an angle describing the geometry of the crack. Equation. 3.12 is an upper bound value for fracture toughness. While it is unlikely this geometry has a gradient stress, for demonstration and as a lower bound estimate, the solution for fracture toughness of a corner crack under an applied gradient stress in a square beam is given as [184]:

$$K_{Ia} = \frac{2}{\pi}\sigma\sqrt{\pi a} \cdot F(\theta), \text{where}$$ 3.16

$$F(\theta) = 1.0 - 0.72\sqrt{\sin\theta} + 0.11(\sin\theta)^2, \text{ for } (10° < \theta < 80°).$$ 3.17

Equation 3.16 is a lower bound for fracture toughness as determined from corner cracks. As a zeroth-order estimate, it is assumed that the crack opening tensile stress is on the order of the normal compression stress giving:

$$\sigma = \frac{P}{A} = \frac{4P}{d_o^2}.$$ 3.18

However, it is more likely that the radial stresses contribute to crack opening, and these stresses are less than the applied normal stresses, as observed in bulk cylindrical specimens [185, 186]. There are several models that can be used to estimate the circumferential stresses in cylindrical specimens, but averaging the multiple models found in work by Al-Chalabi and Huang [185], the modified circumferential stresses in the micropillars are approximately half of the normal stresses applied. These models also indicate that though there is a minor gradient in the circumferential stresses, it is far more likely that the pillars have a uniform stress in this direction. This could explain the extremely small values of fracture toughness determined from a stress gradient approach, though realistically the plasticity observed in the small pillars will not accurately reflect fracture toughness values

81

through this analysis which assumes only brittle failure. Additionally, the fracture toughness values, calculated by the geometry of the cracks when the load has been removed, do not reflect the stresses at which the crack initiated, and do not account for secondary cracking.
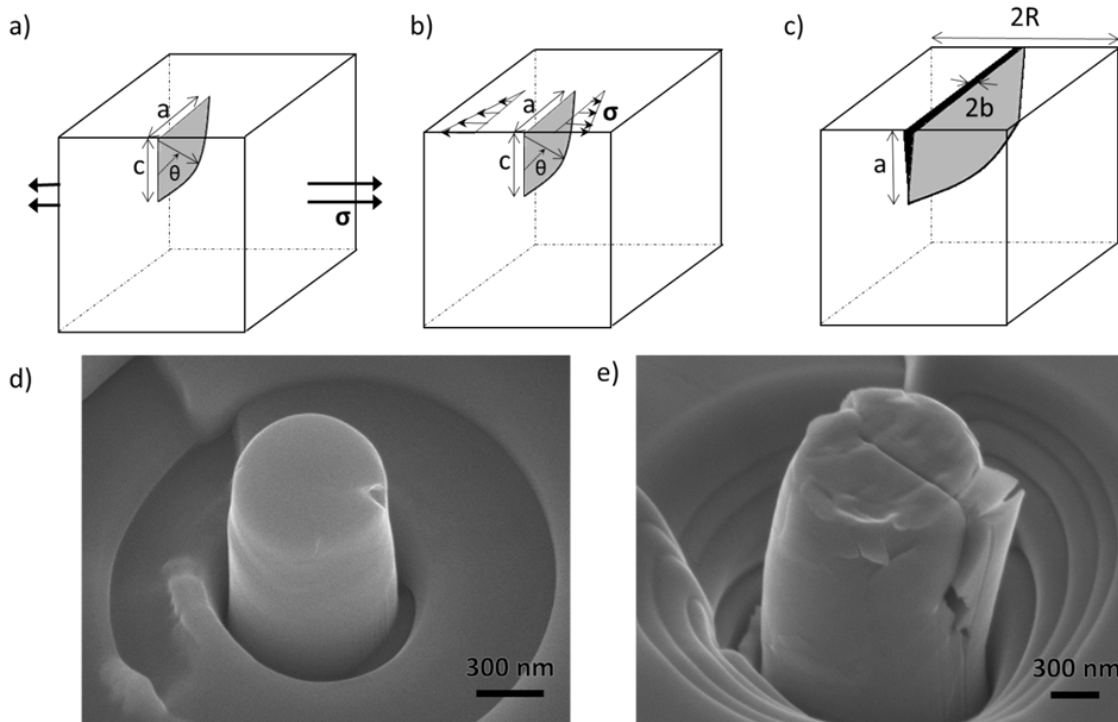
Figure 3.20: (a-c) adapted from Reference **[184]** *Models showing parameters for fracture toughness calculations for a) a corner crack under uniform stress in a square beam, b) a corner crack under a gradient stress in a square beam, c) through-thickness pillar failure. SEM images of ScD$_2$ on Mo tested micropillars showing (d) corner cracking and (e) through thickness failure.*

Since the cracks in these pillars tended to propagate towards through thickness cracking, it is understandable that there is a significant scatter in the data calculated using a corner cracking model. This is due to effects from plastic deformation, especially at the top of the pillar, unknown crack front geometry inside of the pillar samples, and estimations of the stresses that caused cracking. Cracks that propagated across the pillar diameter were examined by treating the pillar as a square cross section using [55, 187]:

82

$$K_{Ic} = \frac{\sqrt{3}E_f b R^{3/2}}{4a^2(1 - v_f^2)},$$

3.19

where R is the half of the beam cross section, here set equal to the pillar radius, and b is the half wedge opening. This analysis considered only the main cracks, assumed a film modulus of 150 GPa and Poissons ratio of 0.25. See Table 3.2 for all fracture property data. Ostlund, et al. [55] also used Broeks' analysis for pillar fracture toughness, and took further steps of using finite element analysis to model a cylindrical specimen with a curved crack. The modeling results of the cylindrical specimen versus the Broeks' analysis using a square-cross section did not differ by more than 20%.

Table 3.2: Fracture property data of ScD₂ micropillars and films. All values are given in MPa-m$^{1/2}$.

Analysis Method		Substrate		
		Fused Silica	Mo	
Corner Crack	Uniform stress	1.0	*Diameter ≤ 0.8 µm* 0.33±0.08	*Diameter ≥ 0.8 µm* 1.8±0.57
	Stress gradient	0.4	0.14±0.04	0.72±0.23
Wedge opening crack		1.4	1.2±0.2	1.1±0.3
Channel cracking		1.0-1.9	N/A	

There seems to be a heavy size dependence and large scatter in fracture toughness determined in through corner crack analysis, but axial splitting in all pillar sizes resulted in approximately the same fracture toughness for all pillar sizes. This is expected as the variables in Equation 3.19 are more dependent on material properties and crack length rather than stress conditions of the test, leaving less opportunity for variability in the data. Nevertheless, all data minus the smallest pillar sizes on the Mo substrate have fracture

toughness values within one standard deviation of each other, including the fracture toughness values calculated on the fused silica substrates. Here, it should be noted that the fracture at the top of the pillars could be a consequence of the loading conditions and the stress gradients caused by the somewhat rounded tip. Other issues include a higher likelihood that the smallest pillars have some bending due to the height: diameter ratio, significant plasticity occurs in the smaller pillars, and the stress analysis is oversimplified. Regardless, smaller pillars here are less likely to fracture statistically.

Throughout testing, thirty-four 0.3 μm diameter pillars were tested, with only 47% of these showing some fracture as opposed to sixteen 1.6 μm diameter pillars tested where 80% of samples fractured. This shows a markedly larger percent of larger diameter pillars fracturing. In addition, the fracture of the pillars appears to be intergranular, as evidenced by some post-test SEM images. Even though smaller pillars are unlikely to have more than one grain in their x-y plane, it is possible that some of the 0.3 μm pillars contained a grain boundary, and exhibited fracture. This would explain the pillar splitting fracture toughness values being so similar in all pillar sizes, and points at grain boundaries as the stress-limiting design factor for these films.

Chapter 4 : Activation Volumes for Dislocation Motion in Ni and Si After Thermal Hydrogen-Gas Charging

4.1   Introduction

This chapter focuses on methods to experimentally characterize the mechanical property changes in single crystals of Ni and Si due to the addition of hydrogen, and begins to quantify parameters that describe plastic deformation at small length scales by determining the activation volume for dislocation motion. Ni and Si are meant to be representative of ductile and brittle materials, and both systems have previously shown hydrogen charging effects [188, 189, 190, 191, 192, 193, 91]. Small volumes will be investigated, because Si requires small volumes to promote plasticity over fracture at room temperature [73, 55]. In addition, Si has applications at small scales that are relevant to the testing completed here, see Chapter 2 for additional details. Ni, on the other hand, has few applications at this scale, but small scale testing can define dislocation activation parameters for mechanical property mechanistic studies at larger scales, such as monitoring Ni-based components in industrial use [194].

As previously stated, activation volume, when multiplied by the effective stress, determines the mechanical energy necessary for dislocation motion at a given temperature. This parameter provides a quantitative measure of dislocation activity without relying upon *in-situ* TEM mechanical testing or imaging lift-outs of the material with transmission electron microscopy to observe dislocation structures. Two primary methods for determining activation volume, nanoindentation and micropillar compression, are assessed

and provide insight about the impact of stress state on dislocation dynamics. Relative comparisons of effective stress and activation volume in Si demonstrate that both the dislocation velocity and fracture toughness are likely to decrease as seen in nanoindentation and micropillar compression, respectively. In this chapter, basics of the experiments will be presented followed by the results of the experiments on Ni then Si. First, it is important to discuss the materials themselves to have a basic background on expected material behavior.

4.1.1. Ni

The mechanical behavior of Ni is relatively straightforward as the ductile metal has an FCC structure; slip operates on the $\{111\}<0\bar{1}1>$. However, at these small volumes, Ni has size effects as previously determined by Reference [195], where pillars below 20 μm diameter are likely impacted by a combination dislocation exhaustion followed by rapid dislocation multiplication due to the high stresses at this scale. Thus, micropillars should display slip bands and discontinuities in load-displacements due to slip events associated with large dislocation bursts [195, 127].

Ni is also impacted by hydrogen, where larger concentrations of hydrogen at grain boundaries result in higher susceptibility to intergranular fracture [196, 197, 198]. There are competing experiments with single crystals of Ni at the bulk scale that have yet to be fully understood. Studies of single grains of Ni that have been hydrogen charged have shown a drastic decrease in fracture toughness [199] but others have shown that ductile processes dominate in tension but with increased work hardening rates relative to non-hydrogen charged materials [197]. The results can be used to support the HEDE

86

mechanism due to increased fracture at grain boundaries or another mechanism where dislocations are stabilized by hydrogen causing additional pile-ups, and eventually nucleate cracks on slip plane intersections [198]. Small volumes of Ni should isolate this behavior and the post-test sample fracture surfaces could provide further evidence for one mechanism or another.

4.1.2. Si
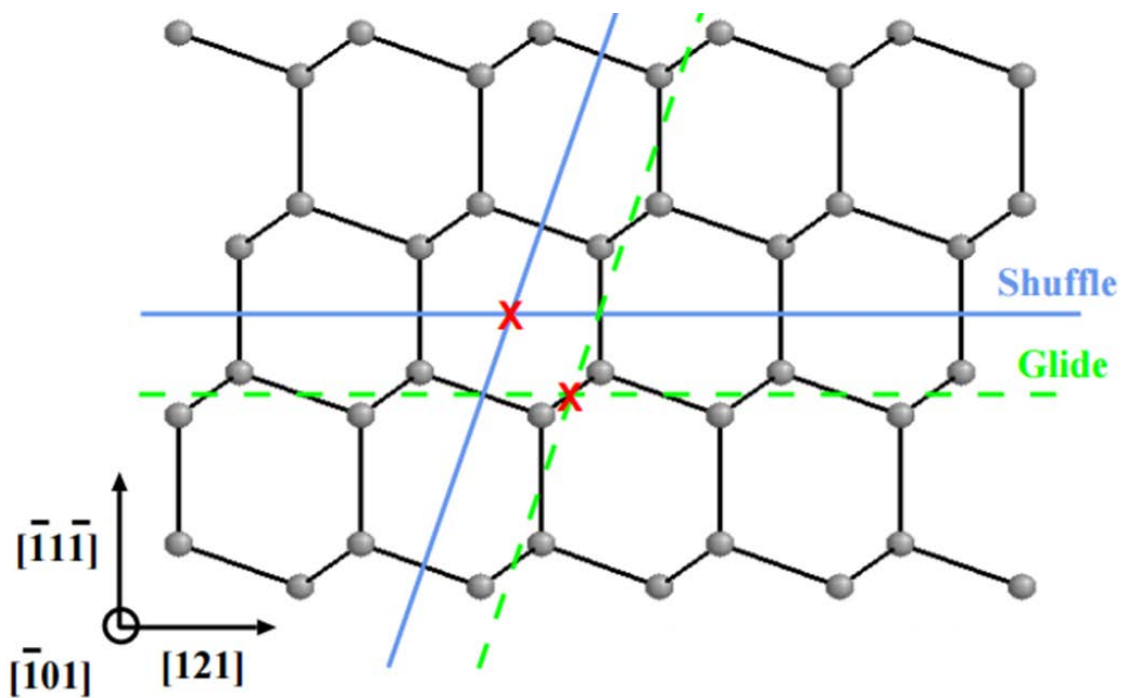
Figure 4.1: A (101) projection of the Si lattice, showing two glide and shuffle slip planes. Taken from Reference **[201]**.

Si is generally considered a brittle material; however, for small length scale components, plastic deformation and cracking can occur and must be accounted for in component design [56, 200]. This DBT transition in Si is also impacted by dopants, temperature, stress state, and phase transformation as discussed at length in Chapter 2 [188, 4]. To further complicate the behavior, hydrogen can also alter the dislocation

behavior. Since MEMS devices are often produced in acidic environments and are also typically exposed to humidity, there is opportunity for hydrogen to diffuse into these devices and impact mechanical properties [200, 7]. These experiments may demonstrate a path to resolve long standing issues of what hydrogen concentrations in various materials require more in-depth solutions involving HEDE and HELP mechanisms. This work focuses on plastic deformation and fracture by determining the activation volume for dislocation motion in both as-received and hydrogen charged material.

Si has a diamond cubic structure, and the slip behavior is somewhat more complicated in this crystal structure since it is not a close-packed structure [201, 21, 63]. Dislocations in Si are summarized as functioning on the {111} planes in a broad shuffle or narrow glide set. The shuffle set has been observed to operate at room temperature and high stresses [202, 55] whereas the glide plane operates mostly at high temperatures and lower stresses [203]. A projection of the (101) in Si with the two slip planes from Reference [201] are shown in Figure 4.1. At low temperature, dislocation motion is in Si controlled by the Peierls mechanism and a dislocation will move through a structure through a double kink formation [63]. However, the small volumes studied here affect dislocation nucleation and motion by promoting plasticity in the material. The increase in plasticity is thought to occur due to the high stresses in these volumes causing slip systems to transition from the glide to the shuffle set [55]. Another possible explanation is that small volumes may limit the dissociation of dislocations into only one, faster partial dislocation. This faster partial dislocation can move through the material with nucleation of a single kink [55, 204]. Other studies testing larger volumes of n-doped Si, but charging the sample with a hydrogen

plasma that introduces additional material damage, also showed an increase in dislocation velocity under applied stress at elevated temperatures [76]. Thus, in this testing scheme it is important to define original mechanical properties for a material before determining hydrogen effects at room temperature.

4.2   Experimental Procedures

4.2.1. Ni
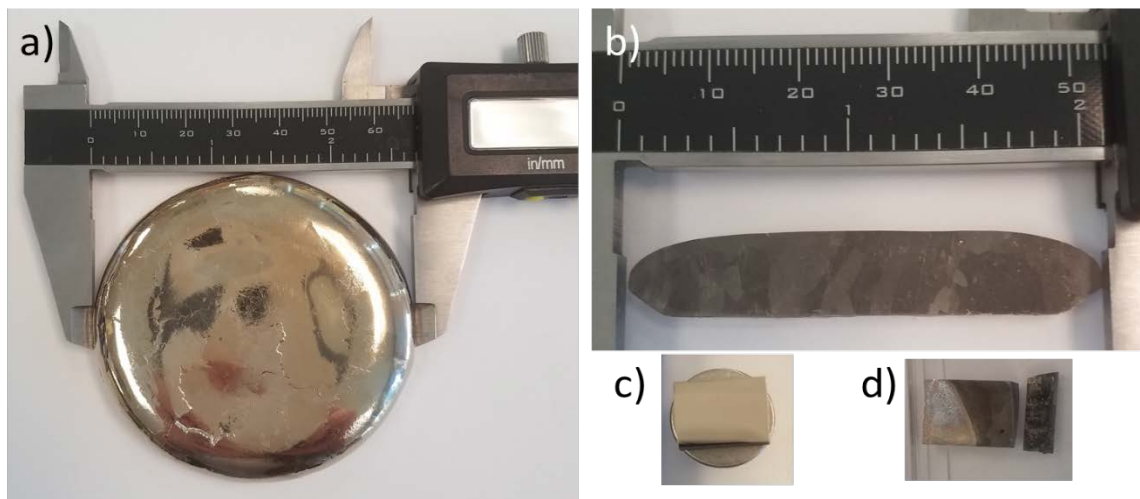
Figure 4.2: a) 3 inch, arc melted Ni buttons b) cross section of button c) polished specimen used for nanoindentation and thermally charged with hydrogen and d) electrolytically hydrogen-charged samples.

99.99% Ni shot was arc melted in vacuum at Knolls Atomic Laboratory using zirconium as an oxygen getter during the arc melting process. This resulted in samples with visibly large crystalline grains that were used for single crystal studies, see Figure 4.2a and b. Arc melted button material was then cut into manageable, flat slices using a circular diamond saw for transverse directions of the button face. Polishing of these samples was completed using diamond pads as well as a finishing polish with colloidal alumina. EBSD was completed on these small sections to determine grain orientation before mechanical

testing to document grain orientation with an Oxford system on the JEOL 6500 SEM in the UMN characterization facility. Images of the arc melted Ni button, cross sections of the button, and prepared samples for testing are shown in Figure 4.2. After EBSD, micropillars were milled using a similar procedure as in Chapter 2, but only two pillar diameters were produced: 400 and 800 nm.

4.2.2. Si

The majority of experiments for Si were completed on polished, phosphorus-doped, 380 μm thick (100) wafers (ρ = 1-10 Ω), and a small amount of experiments were performed on polished, arsenic-doped, 500 μm thick (111) wafers (ρ = 1-10 Ω). n-type Si was chosen because n-type dopants should promote the plasticity of the material, as has been previously documented, where n-type Si showed an increase in the dislocation velocity versus intrinsic material [205, 206].

Single crystal wafers were used for nanoindentation testing, and uniaxial compression tests were completed on micropillars that were produced with a FEI 200 3D Quanta FIB using an accelerating voltage of 30 keV on the same wafers, as outlined in Chapter 2. Three diameters of micropillars were created: 0.5, 0.75, and 1 μm. All Si used in this chapter was etched with an HF-HCl solution post FIB-processing to mitigate oxide effects and Ga damage from the ion beam [207]. The etching solution was a combination of 15 mL HF, 5 mL HCl, and 250 mL DI water. Samples were stirred in the solution for a minimum of 6 minutes, then rinsed with three separate baths of DI water, and dried under a fume hood. Subsequent cleaning with solvents was completed as needed.

SiO$_2$ thickness was measured before and after hydrogen charging using a VASE ellipsometer to measure any additional oxidation caused by the elevated temperatures required for hydrogen charging.

4.2.3. Hydrogen Charging

Material was thermally hydrogen charged at Sandia National Laboratory in a purged chamber at 573K and 140 MPa hydrogen gas for 10 days. Hydrogen charged samples were kept in dry ice to limit hydrogen outgassing until testing. Electrolytic hydrogen charging was also attempted on the Ni using perchloric acid with Pt foil as an anode. Although the electrolytic cell produced gas bubbles on the Ni surface, the surface of the Ni was too damaged through the process to perform adequate nanoindentation experiments. Examples of these surfaces can be seen in Figure 4.2d.

Fick's second law was used to make a first order estimation of hydrogen concentration in both samples, though experimentally determining hydrogen concentration was not completed. Fick's second law is [13]:

$$\frac{\partial C}{\partial t} = D \frac{\partial^2 C}{\partial x^2},$$ 4.1

Where C is a concentration of a solute, here hydrogen, t is time, x is distance and D is the diffusion coefficient. Both systems are modeled using the semi-infinite solid solution, and assume that the hydrogen concentration at the surface is constant [13]:

$$\frac{C_x - C_0}{C_s - C_0} = 1 - \mathrm{erf}\left(\frac{x}{2\sqrt{Dt}}\right).$$ 4.2

Where concentration subscripts refer to values at the s, surface; 0, initially in the sample, and x, at a given distance from the surface. Results are found in section 4.4.1.

4.3 Mechanical Testing Details

Samples were tested at room temperature using a Hysitron TI-900 Triboindenter with a Berkovich tip for nanoindentation and a 5 µm radius conical tip for pillar compression. Hardness and elastic modulus of the materials were determined using nanoindentation, while micropillar compression was used to determine yield stress. The hardness measured using nanoindentation was later converted to yield stress to compare testing methods. Pillar imaging was completed before and after testing with a JEOL 6700 SEM at 5 keV to measure relevant sample dimensions and testing implications.

4.3.1 Strain Rate Jump Testing for Activation Volume Determination

There are four widely used methods that can be used to determine the apparent activation volume for dislocation motion. These include stress relaxation testing [208, 209, 210, 211], strain rate jump testing [208, 212, 213], differential creep tests [214, 211], and finding the yield stress at several strain rates and fitting these value to the Eyring equation [215, 216]. Stress relaxation testing is a process where a constant strain rate is applied to a material until it reaches a predetermined load, then no additional strain is applied as load drops are measured. This process occurs only on the elastic portion of the material, depends on pre-existing dislocations in the material, and must be repeated multiple times on the same sample and requires an extremely low drift rate for the tests to be valid [211]. This makes this test method unsuitable for nanoindentation as plastic deformation is always applied and the drift rates for the nanoindentation equipment available are too high for long relaxations times. Differential creep tests require a material to be heated to higher temperatures with a constant stress, then a material is subjected to a temperature or stress

92

change that is related to the strain rate response [217]. However, no temperature stage was available for most testing and drift rates are still an issue with this testing method. Lastly, while yield stress determinations from various strain rates are straightforward and accomplishable through nanoindentation, the differences in sample geometries and the number of samples for a statistically significant analysis are daunting and sample preparation is that much more expensive. Instead, multiple strain rate jumps were employed for all nanoindentation and micropillar compression tests where strain rate was changed by approximately an order of magnitude to determine the material's stress response. Strain rate jump testing is readily applicable to nanoindentation techniques as each test is relatively short, multiple tests can be completed on an individual sample, and plastic deformation is expected to occur in micropillars as these tests are typically done past the yield stress of the material.

Strain rate jump tests require the use of multiple constant strain rates. To maintain constant strain rates, slightly different techniques were used for micropillar compression and nanoindentation. Specifically, micropillar compression directly compared changes in
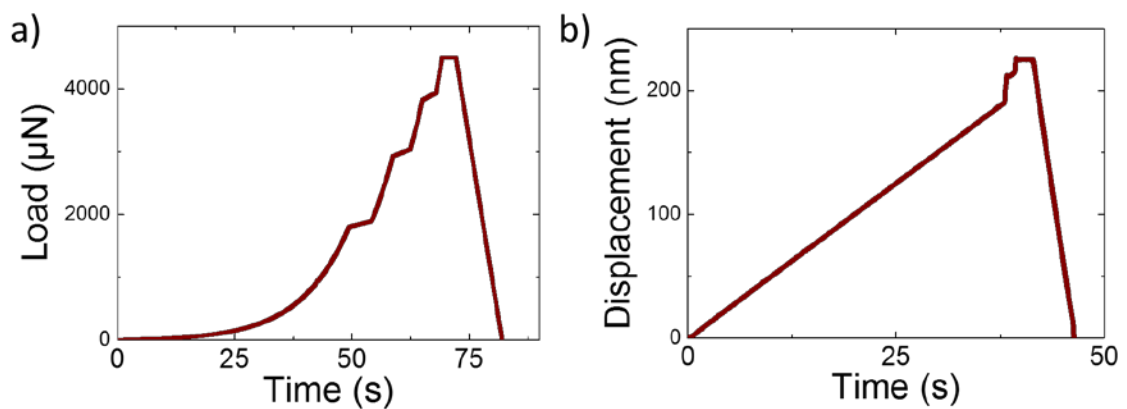
Figure 4.3: Strain rate jump test testing schemes for a) nanoindentation and b) micropillar compression.

93
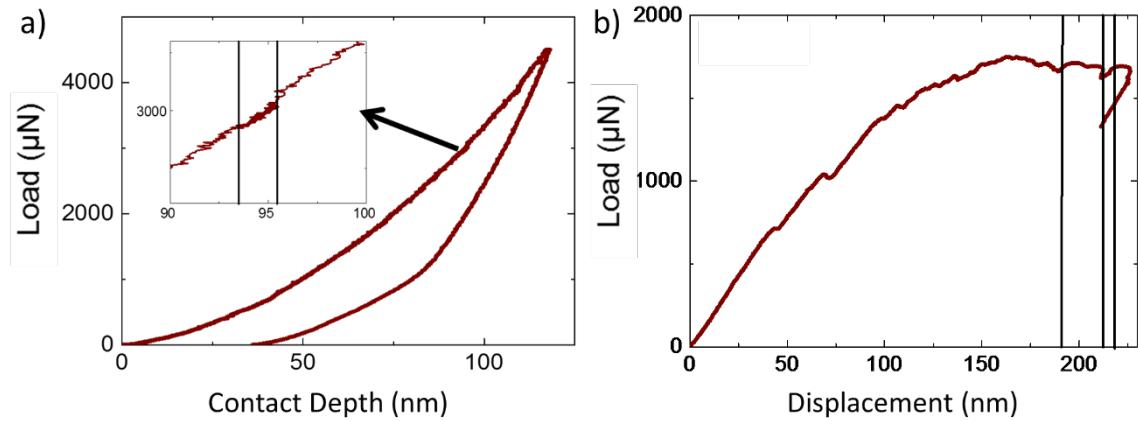
Figure 4.4: (100) Si strain rate jump tests, with vertical lines indicating strain rate jumps for a) nanoindentation and b) micropillar compression.

strain rate to changes in stress [85], while nanoindentation testing compared strain rate changes to relative hardness values [212]. Pillar compression testing was controlled by displacement and strain rates were determined through engineering strain while nanoindentation was controlled by maintaining a constant effective strain rate of $2\dot{\varepsilon} = \dot{P}/P$ [218, 219]. Testing with these two methods provides information for material in a triaxial and uniaxial stress state, respectively. Examples of the user-input testing schemes for these tests can be seen in Figure 4.3a-b, and example data sets demonstrating changes in load due to strain rate jump tests for nanoindentation and micropillar compression of (100) Si are shown in Figure 4.4a-b.

4.4 Results and Discussion

4.4.1   Hydrogen Estimations

4.4.1.1 Ni

Before discussing the mechanical testing, first hydrogen diffusion should be discussed. The diffusion parameters in Ni are well defined; the diffusion coefficient can be estimated below 360°C from the empirical fit by Reference [220] as:

$$D = 4.8 * 10^{-3} exp\left(-\frac{0.408 eV}{RT}\right) cm^2 s^{-1}, \qquad 4.3$$

The solubility has also been determined at 1 atm [221]:

$$S = 3.26 * 10^{-3} exp\left(-\frac{3.6\ kcal}{RT}\right) atoms/atom, \qquad 4.4$$

and was used as a lower estimation of hydrogen concentration in the material. The same arguments of error and issues with the analysis are listed in the previous section, however, the diffusivity of hydrogen is significantly higher in Ni than in Si, resulting in only minutes of time for free hydrogen to remain in the material. However, trap sites in the Ni will likely retain hydrogen in the sample, particularly at surfaces and grain boundaries, though dislocations and vacancies in Ni can also trap hydrogen to a small degree [198]. Similar samples could undergo gas extraction, etc, in the future to confirm this experimentally.

4.4.1.2 Si

Diffusion parameters for hydrogen in Si at room temperature are relatively difficult to determine, but several authors have extrapolated the diffusion coefficient of hydrogen in Si as $\sim 10^{-10}$ cm^2/s [222, 223, 224, 225, 90]. This is heavily dependent on dopant concentration particularly in p-type Si, but in n-type Si, hydrogen or hydrogen-species are most likely to diffuse in the Si lattice in interstitial sites [222, 226]. The diffusion coefficient of hydrogen in Si at 573 K was estimated as $6*10^{-7}$ to $5*10^{-10}$ cm^2/s based on extrapolation from Reference [90]. The estimated maximum solubility of hydrogen in Si was again extrapolated from Reference [90], ranging from $2*10^5$ to $4*10^7$ atoms/cm^3. Based on a simple diffusion model assuming zero initial hydrogen concentration, the total concentration inside the wafer samples at depths less than 10 μm, relevant for mechanical

testing, reached the equilibrium concentration during the lengthy charging process. After the charging process, the excess hydrogen is expected to diffuse out of the sample.

A similar diffusion estimate for outgassing using the expected hydrogen concentration due to charging and the room temperature diffusion coefficient suggests that a significant amount of free hydrogen remained in the Si material for 100's of hours post charging and outgassing at room temperature. Testing time was limited to a maximum of 24 hours at room temperature, significantly longer than the time required for experimental measurement. Additionally, significant hydrogen is likely trapped in the material at defect sites and stress gradients result from outgassing. Unfortunately, these assumptions are only first order estimations with several error sources, and do not allow us to explicitly calculate the hydrogen concentration during testing. Further tests could be completed with gas extraction, etc. to confirm the hydrogen concentration in these specimens.

4.4.2   Mechanical Testing

The following sections show the marked difference in how a ductile, FCC metal can drastically differ from a brittle diamond cubic structure semiconductor, both with and without hydrogen additions. However, to examine how a different stress state impacts mechanical properties, nanoindentation and micropillars were tested. Nanoindentation represents a triaxial stress state, while micropillar compression is close to a uniaxial stress state.

The same procedure and nanoindentation and micropillar testing scheme was used for the Ni as in Si. Two main differences are expected and observed in these samples: Si is less ductile and Ni is more strain rate sensitive. The marked difference in mechanical
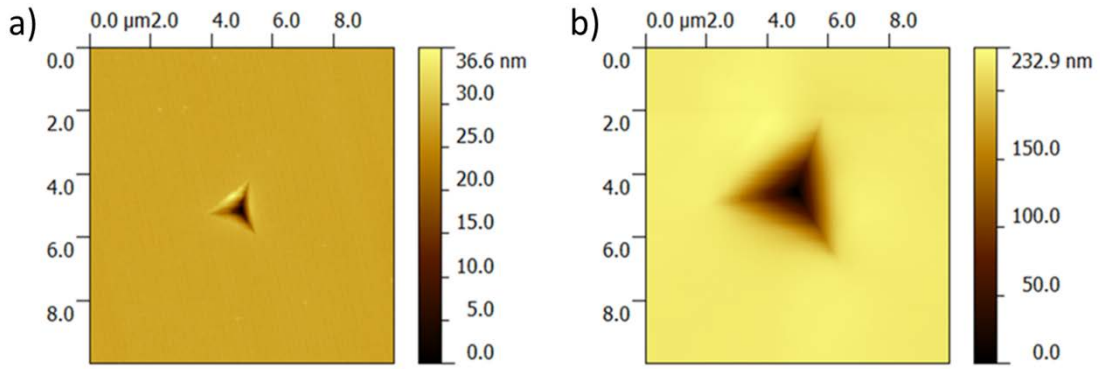
Figure 4.5: Berkovich indentation impressions taken by the triboindenter's scanning mode after a 4500 µN load for a) Si and b) Ni.

behavior of Si versus Ni can be seen not only in the hardness calculations but in the size of the indent generated by the Berkovich tip. When Ni and Si are tested to the same load, Ni has a much larger indent impression as seen in Figure 4.5. In addition, the stress response from a strain rate jump test is more significant in Ni than it is in Si samples due to the increased strain rate sensitivity. In general, Ni has larger modulus but lower hardness values than the Si material tested. Ni also has much easier slip than Si – this is particularly evident in micropillar sample results shown in the following sections.

Apparent activation volume, V*, normalized by the Burgers vector cubed, was also determined for nanoindentation and micropillar compression. V* was found in both testing conditions by calculating [212, 227, 85]:

$$V^*_{nanoindentation} = \sqrt{3}k_B T \left(\frac{\partial ln\dot{\varepsilon}}{\partial \sigma^*}\right)_T \; and \qquad\qquad 4.5$$

$$V^*_{micropillar} = \frac{k_B T}{\left(\partial\tau^*/\partial\dot{\varepsilon}\right)_T}. \qquad\qquad 4.6$$

Here, T is temperature, $\dot{\varepsilon}$ is strain rate, τ^* is the effective shear stress and σ^* is the effective stress. For indentation, it is assumed that the shear stress is related to the normal stress by

a factor of 0.5. The change in stress was found by determining the nanoindentation hardness of the material and dividing by an empirical constant, 2.4 for Si [130, 131] and 3 for Ni [129]. These equations are very similar to Equation 2.20 but have modifications for both stress and indenter geometries.

4.4.2.1 Ni

4.4.2.1.1   Nanoindentation
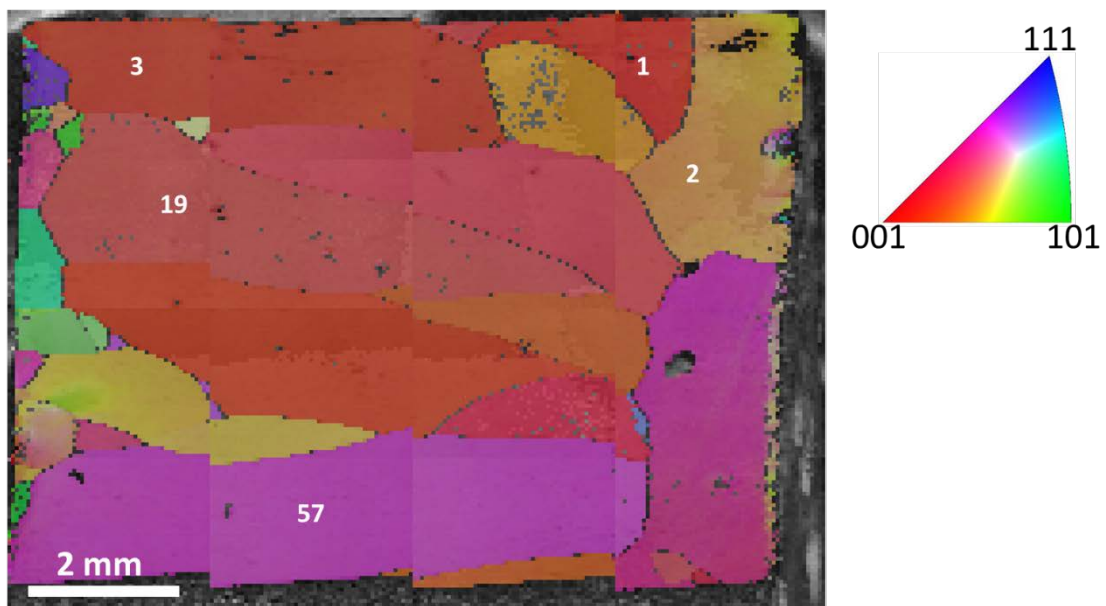
Figure 4.6: EBSD map of Ni for nanoindentation. Approximate grain orientations are: Grain 3 ~ (124), Grain 19 ~ (123), Grain 57 ~ (312). Grain 1 ~ (135) and Grain 2 ~ (300) were tested after hydrogen charging.

EBSD maps of Ni were generated and three grains were investigated with nanoindentation before hydrogen charging, see Figure 4.6 for the EBSD map and the three selected grains for nanoindentation, each which can be considered single crystals in these testing schemes. Grain boundaries were defined by a 15° misorientation.

Hydrogen outgassing did not seem to impact the reduced modulus or hardness over the period where testing occurred in Ni. However, with the addition of hydrogen, hardness

increased by about a factor of 2. Modulus and hardness values vary with orientation and local dislocation sampling on Ni as previously shown [228, 229, 230, 195]. The reduced modulus values found for grains 3 and 19 are much lower the expected range modulus for Ni and are not reported, though all other values are reasonable within previous experimental results and are provided in Table 4.1 [228, 229, 230, 195]. Pile up, or plastic deformation around the tip that would increase the actual tip-sample area, could have impacted these measurements. Measured hardness values would have an apparent increase in this case, but no scans of the material were taken post-indentation. It should be noted that all nanoindentation was completed using a magnetic stage, and that Ni mechanical properties are impacted by magnetization, though this usually corresponds to an overall increase in elastic modulus [231]. No fracture indications occurred during any Ni nanoindentation, likely due to stress state and the large ductility of this system. The other obvious change with this testing is that hydrogen charged Ni has a higher hardness than the non-charged samples, though this is partially due to the different grain orientations tested. The hardness and reduced modulus of the grains tested before and after hydrogen charging are found in Table 4.1.

Table 4.1: Ni nanoindentation mechanical property summary.

Grain Number	Orientation	H-charging?	H (GPa)	E_r (GPa)
3	(124)	No	0.91 ± 0.02	250 ± 14
1	(135)	Yes	1.7 ± 0.2	200 ± 19
2	(300)	Yes	2.1 ± 0.4	220 ± 29

4.4.2.1.2　Micropillar Testing
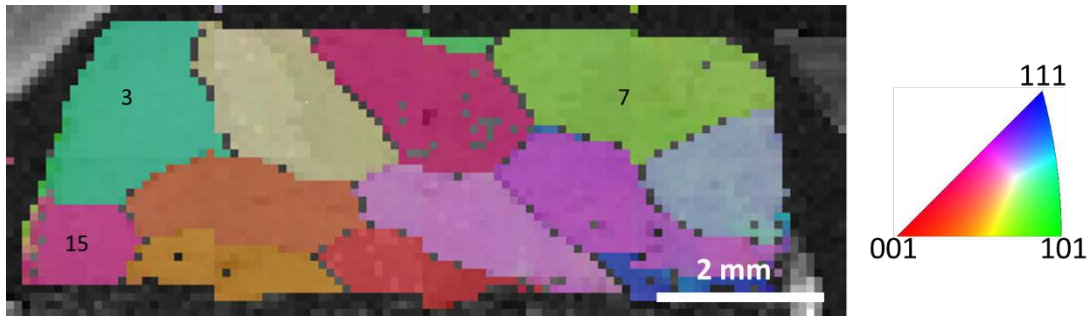
Figure 4.7: EBSD image of Ni specimen with grains of interest for micropillar compression. Grains were higher ordered planes, but the closest approximations are: Grain 7 ~ (110), Grain 3 ~ (111), Grain 15 ~ (012).

Due to the magnetic nature of Ni, FIB milling and SEM was more difficult than other samples. However, pillars were generated and characterized with these methods. Smaller sample sizes and larger working distances were used to minimize the samples' magnetic interaction with the imaging electrons. An EBSD map of the sample that was used is shown in Figure 4.7, highlighting the three grains of Ni where micropillars were milled. The grains selected were the lowest order planes available on the sample surface as follows: grain 7 ~ (110), grain 3 ~ (111), and grain 15 ~ (012*)*. Only one micropillar diameter, 1 μm, was made for each non-hydrogen charged samples, but two sizes were milled for hydrogen charging samples: 0.8 and 0.4 μm. Previous studies have shown a size effect in Ni pillars, where smaller pillars have shown increased yield stresses and strain hardening [82].

Micropillars were tested with constant displacement rates. Example images of the pillars and the corresponding stress-strain curve are shown for each grain tested without hydrogen charging can be seen in Figure 4.8a-c. What becomes obvious in these results is

that large slip planes are generated, and result in large load or stress drops during pillar

testing as expected. This means that strain rate jump tests and these load drops cannot be
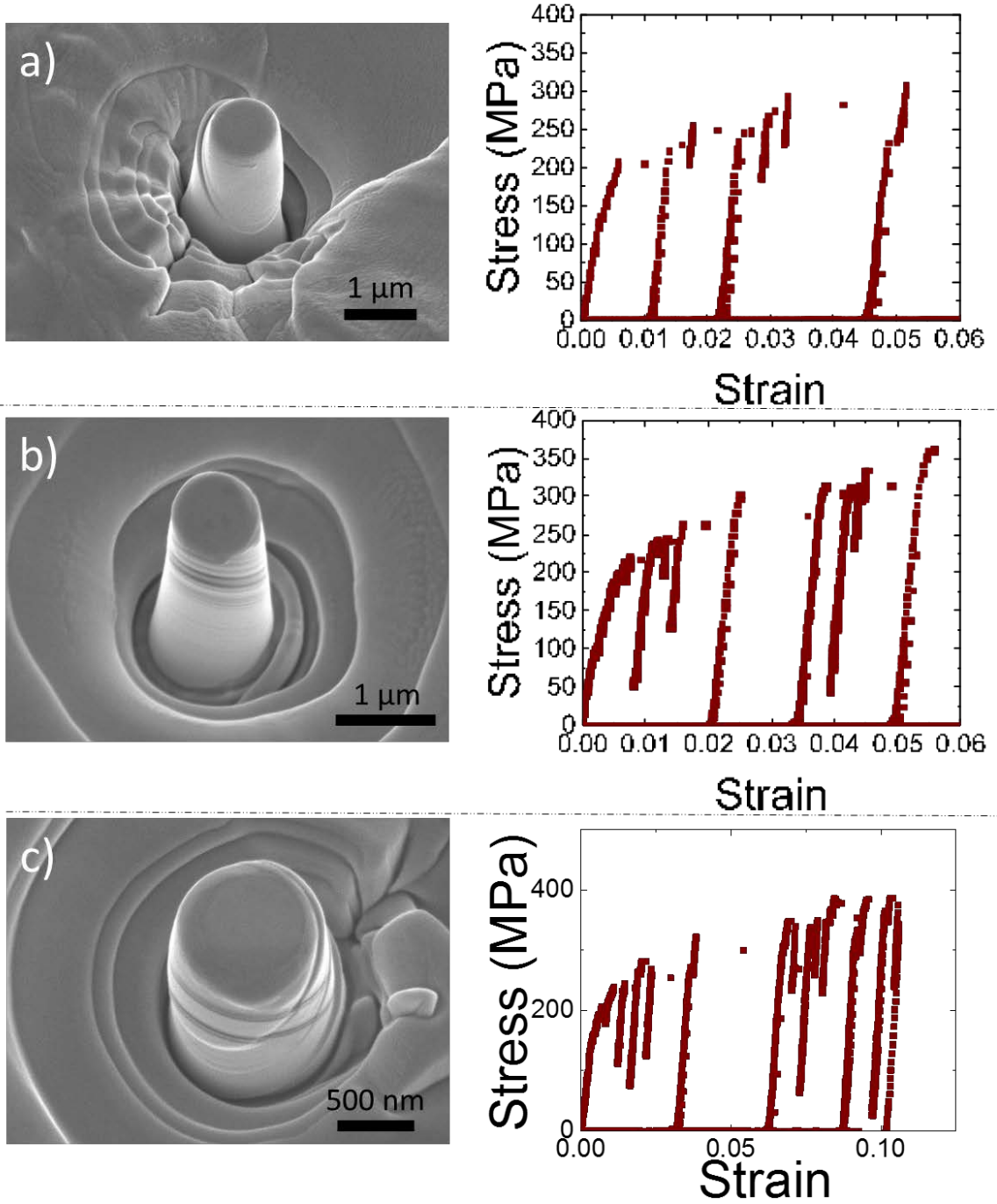
Figure 4.8: Ni micropillar tests showing slip bands in SEM images (left) and load drops in the corresponding stress-strain curves (right) for grains a) 3, b) 7, and c) 12 as mapped in Figure 4.7.

differentiated, and activation volume cannot be determined by this method. More testing samples were not made to determine strain-rate impacts on yield stress, however, yield stresses for the pillars were determined and can be found in Table 4.2. These yield stress values match very well with other published values for yield stress in Ni specimens, ranging from 60 to 400 MPa [232, 195].

Table 4.2: Yield Stress values for non-hydrogen charged Ni micropillars milled in grains found in Figure 4.7.

Grain Number	Yield Stress (MPa)	Orientation
3	220 ± 23	(111)
7	301 ± 61	(110)
15	226 ± 23	(012)

Though micropillar samples were made on the Ni specimens that were hydrogen charged, none of the pillars survived the charging process. It is possible that the stresses due to hydrogen entering or outgassing through these pillars may have led to pillar failure. Instead, this could have transpired during post-charging or shipment from the charging facilities. Future testing should be completed to fully understand what occurs here.

4.4.2.1.3 Activation Volume

For nanoindentation tests, only the load jumps from fast strain rates to slow strain rates were used to determine activation volumes. This is due to the large time delay in stress decrease with a decrease in strain rate. Micropillar samples provided additional issues - non-hydrogen charged micropillar samples resulted in large slip bands before hydrogen charging. After the hydrogen charging process, no fibbed micropillars survived for subsequent mechanical testing. Thus, Ni micropillars were not used for the activation

volume analysis. The failure of Ni samples after hydrogen charging however, is evidence that hydrogen charging resulted in tensile stresses. In other work, bulk samples of niobium fractured spontaneously and without load after hydrogen charging due to these internal tensile stresses [233]. The Si micropillars survived the charging process and is discussed later. Since Si micropillars were charged at the same time as the Ni specimens, it does point to Ni being more susceptible to processing failures in these experiments. It should be noted that potential FIB damage and intermetallic mixing could have also impacted the failure of the Ni micropillars. The differentiation between hydrogen charging effects versus FIB damage is unknown.
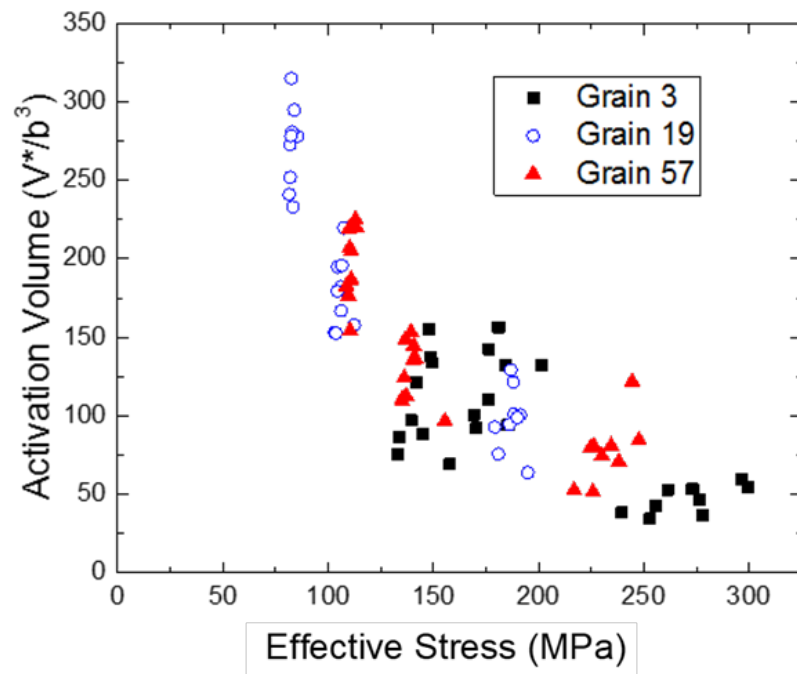
Figure 4.9: Activation volume results for various grains in Ni shown in Figure 4.6.

The Burgers vector of Ni specimens is 0.249 nm, and is used to normalize the activation volume as shown in Figure 4.9 where multiple orientations of Ni grains have similar trends of activation volume versus effective stress. This data corresponds decently well with other Ni tests, where very large grains have activation volumes on the order of 100 to 1000 b^3 for various samples and material preparation [234, 235, 236]. The differences seen in the various grains of Ni are likely attributed to different volumes underneath the indenter tip – each grain likely has different volumes of material between the indenter and subsequent grain of material resulting in a variety of back stresses, changing effective stresses ad activation volume measurements. An example of a strain
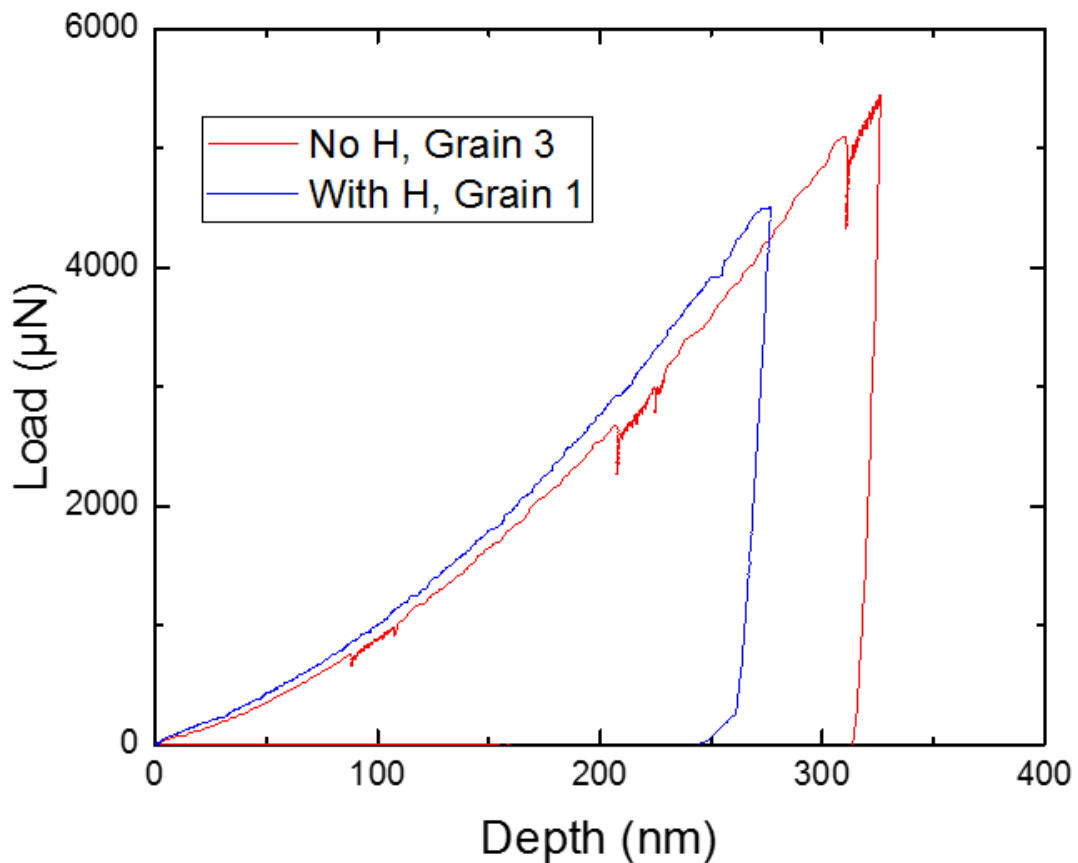
Figure 4.10: Ni nanoindentation strain rate jump tests with obvious stain rate sensitivity in non-hydrogen charged samples.

rate jump test in a non-hydrogen charged samples can be seen in Figure 4.10. Strain rate jumps are quite evident in the image – 5 jumps were completed in each indentation.

After hydrogen charging, the other Ni grains were tested with nanoindentation, and there was no apparent strain rate sensitivity, meaning that the activation volume could not be measured through the techniques used here. An example of the lack of strain rate sensitivity is also shown in Figure 4.10. The same testing inputs were used in this figure for samples with and without hydrogen charging. However, in other bulk, polycrystalline samples, hydrogen has been observed to negatively impact the ductility of Ni [237] and initial results investigating grain-boundary behaviors have indicated that the fracture toughness of single grains of Ni in hydrogen charged samples are greatly lowered [199]. In these experiments, dislocations appear to be less mobile and trapped by the hydrogen atoms, since there are no strain rate effects apparent with the addition of hydrogen into the system. This would favor a HEDE mechanism. However, when a sample is pre-strained, or the dislocation density was increased before hydrogen charging, there was still no strain rate sensitivity effect apparent with the addition of hydrogen. This was evident in nanoindentation tests on a Ni specimen that was subjected to deformation, where various oriented slip lines on all grains of the specimen were generated when removing the specimen from its polishing mount. This indicates that an increased initial dislocation density and a higher hydrogen concentration also prevents a realistic measurement of the activation volume in hydrogen charged Ni. These are initial conjectures and much more work should be done in making a conclusive argument on this subject as discussed in Chapter 6.

4.4.2.2 Si

4.4.2.2.1 Nanoindentation
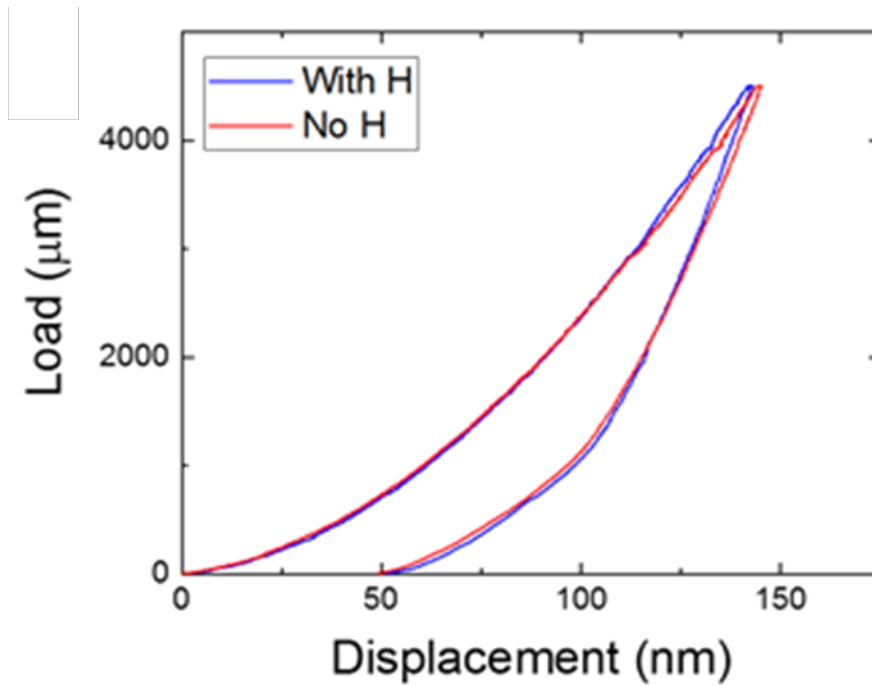
Figure 4.11: Typical nanoindentation tests for n-type (100) Si with strain rate jumps with and without hydrogen charging.

Hardness and reduced modulus values from non-hydrogen charged nanoindentation matched well with accepted values for (100) Si at 10.3±0.3 GPa and 131±2 GPa, respectively [238, 239]. Nanoindentation tests showed no apparent cracking or phase transformation indications.

All testing for the hydrogen charged samples was time monitored, and some time dependence on behavior was noted, particularly in the first thirty minutes after reaching room temperature. However, marked differences in hardness and modulus values compared to non-hydrogen materials were found up to 11 hours after the samples were left at room temperature. The hydrogen charged Si wafers had reduced modulus and hardness values of 148±3 GPa and 10.7±0.4 GPa respectively. The hardness values are only

106

marginally higher than those found in non-charged samples, but the modulus values in hydrogen charged materials are significantly higher than the non-charged material. However, the hardness and modulus measurements exhibited a clear time dependence; the single initial hardness and modulus values were 6 and 2 GPa higher than the average values. Hardness and modulus were rapidly reduced for the second test, approximately thirty minutes at room temperature after the initial test, then over time increased to the average values reported, as shown in Figure 4.12. The single first, and large initial value for hardness and reduced modulus could be an instrument, thermal equilibrium, or sampling error, but the remainder of the changes these measurements are likely due to hydrogen outgassing or may be related to material changes due to thermal charging. It is also possible
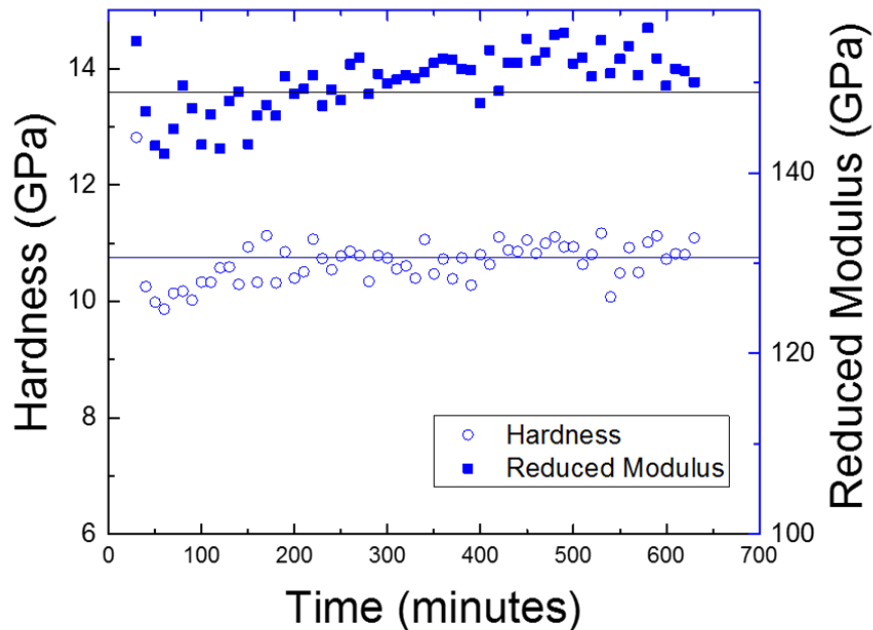
Figure 4.12: Hardness and reduced modulus values determined through nanoindentation as a function of hydrogen outgassing time at room temperature in hydrogen charged Si.

that the increases seen in the hardness and modulus could partially originate from hydrogen outgassing [240].
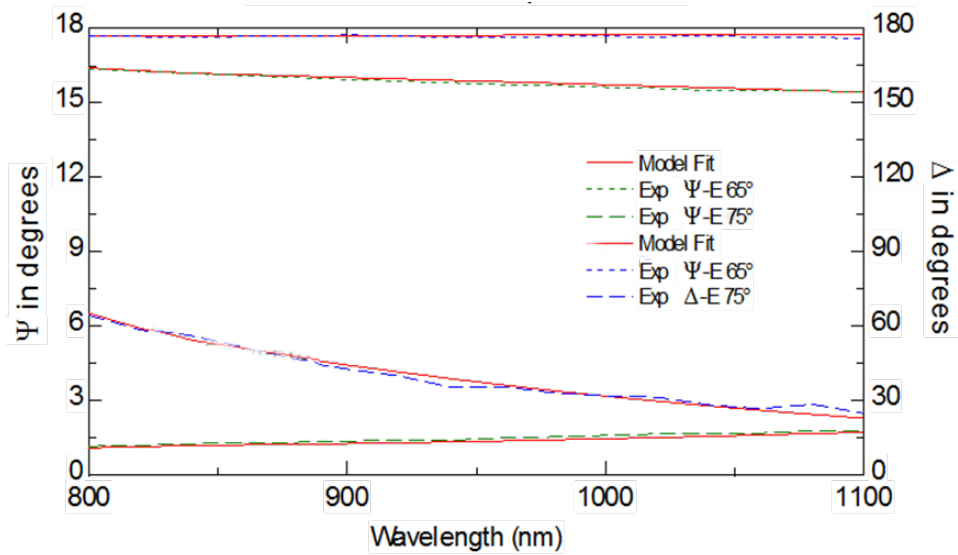
Figure 4.13: Ellipsometry data for a non-hydrogen charged Si wafer used for nanoindentation.

To separate other possible environmental effects, the SiO_2 thickness on Si wafers with and without hydrogen charging was examined. Oxide thickness for Si was measured through ellipsometry. This system works by reflection of light onto a sample, and the polarization changes in the light due to the interaction with the sample are determined by quantifying the amplitude ratio, Ψ, and phase difference, Δ, as a function of the wavelength of light and the angle of incidence of the light on a sample. The thickness of an oxide can be measured because the differences in refractive index of the oxide and Si material result in changes in Δ. Si systems have been well modeled so experimental data can be fit to preexisting models in the WVASE32® software package. The experimental data collected is fit to a model, an example of this is shown in Figure 4.13, and oxide thickness was determined. The non-hydrogen charged material was 2.38 ± 0.4 nm, compared to 2.91 ± 0.1 nm for the hydrogen charged material. This small increase in oxide thickness does not account for the marked increase in the hardness and reduced modulus by itself due to the

displacements used in these experiments [241, 242]. However, because hydrogen outgassing leads to gradient stresses, the Si/SiO_2 interface could be an area of stress concentration due to crystal lattice discontinuity [243]. Stresses were not measured here, but could be determined through FIB milling and digital image correlation developments by others [244, 245].

4.4.2.2.2   Micropillar Testing

Three pillar diameters were used for these tests; compression testing resulted in some plastic deformation measured by height changes as well apparent plasticity from cracking at the top edges of the pillars. Some pillars exhibited brittle failure upon testing, but the majority exhibited mixed apparent deformation and microcracking as indicated in the load versus displacement data for nanoindentation and post-SEM imaging of micropillars. These results are shown clearly in Figures 4.14 a-b) and 4.16 a). Si micropillar samples also had qualitative and quantitative changes in mechanical behavior upon hydrogen charging with smaller overall stresses, larger apparent strains, and increased cracking in final pillar images – see Figure 4.14c for an example image of a hydrogen-charged micropillar before and after compression testing. While hydrogen charging seemed to impact mechanical properties significantly, there was no observable difference in the micropillars after hydrogen charging and before mechanical testing as seen in Figure 4.14b. However, the hydrogen charged samples did have spherical particles in the areas surrounding the pillars, which were heavily exposed to the ion beam, likely implanted gallium coalescing at the surface due to the heat treatment.

An example of the quantitative differences in micropillar behavior with and without
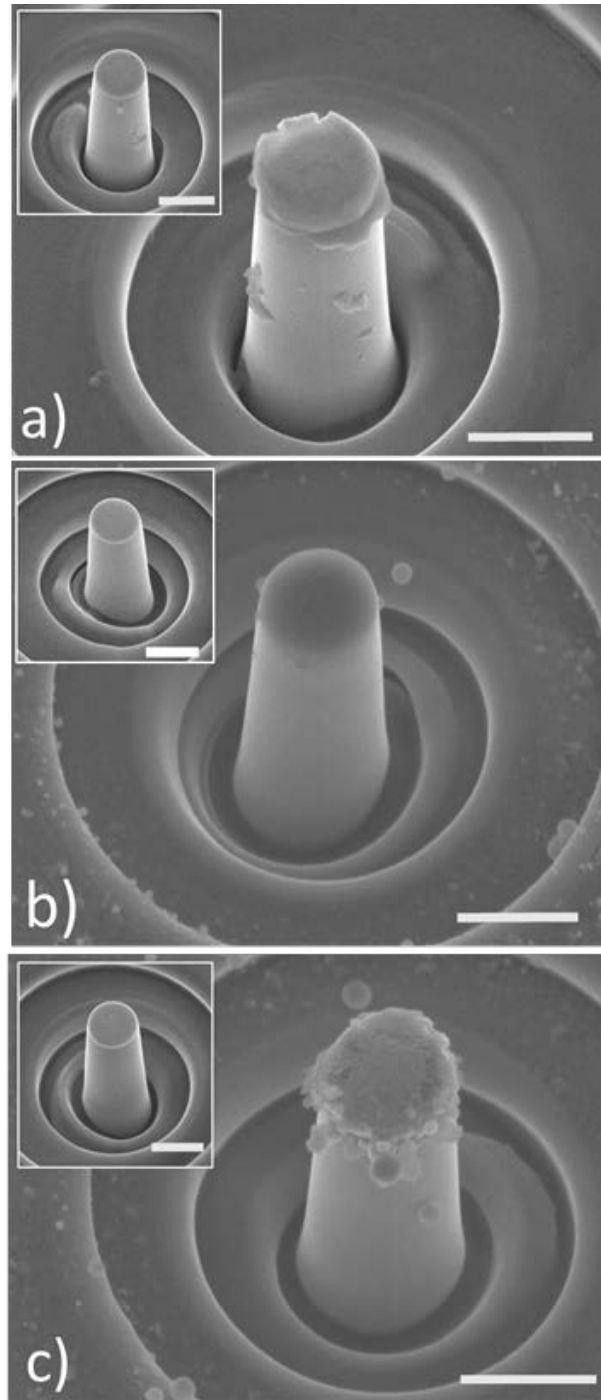
Figure 4.14: All scale bars represent 1 µm. a) micropillar without hydrogen charging after compression testing b) micropillar with hydrogen charging but no mechanical testing c) micropillar with hydrogen charging and compression testing. Subset images on a)-c) are Si micropillars pre-testing

110

hydrogen charging are shown in Figure 4.15 where hydrogen charging resulted in lower stresses and larger apparent strains. However, hydrogen outgassing time also impacted the mechanical responses of the micropillars. The initial two compression tests on micropillars charged with hydrogen showed extraordinary indications of slip or fracture as large load drops repeatedly occurred before catastrophic failure of relatively high strains, up to 16%. Since these samples were tested until failure, SEM could not confirm whether microcracking or slip occurred during this testing. This extreme load-dropping behavior was not apparent in the micropillars after outgassing at room temperature for 1 hour, however, mechanical behavior was still inherently different than non-hydrogen charged samples.
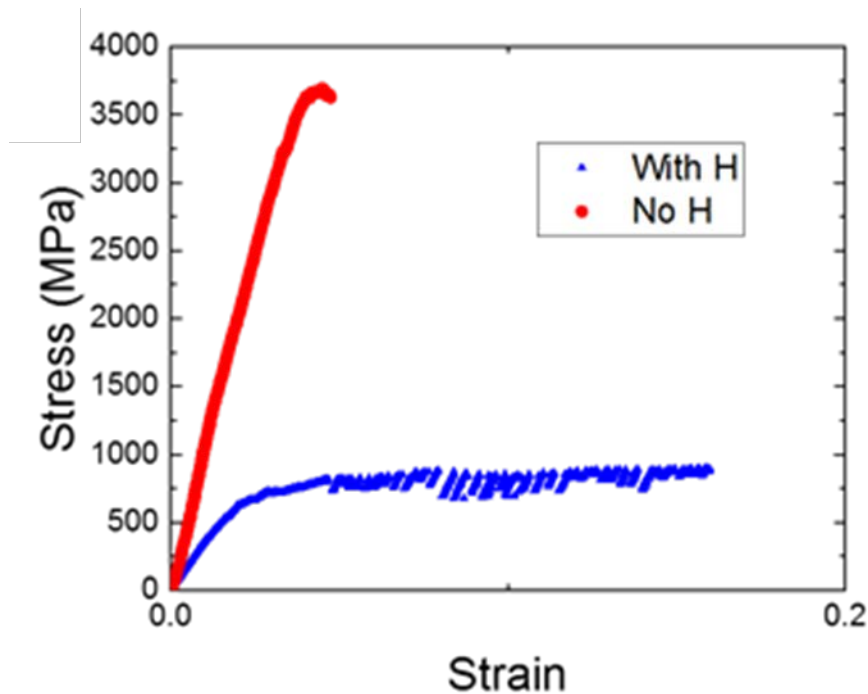
Figure 4.15: Micropillar compression tests for Si without hydrogen charging and immediately after removal from cold storage after hydrogen charging showing large apparent plasticity by significant strain achieved. Both micropillars fractured at the last point on graph.

111

The mean and standard deviation for yield stress were similar for all sizes tested in the non-hydrogen charged material; yield stress for nanoindentation was slightly higher than that found using micropillar compression at 4.3±0.1 GPa and 3.6±0.6 GPa respectively for non-charged Si wafers. The difference is likely due to the confinement in nanoindentation producing larger stresses versus the increased free surfaces available for dislocation nucleation in the pillar samples. The larger standard deviation in the micropillar compression data is attributed to differences in pillar morphology. The average apparent yield stress for the hydrogen charged micropillars was 0.7±0.2 GPa in 750 nm diameter pillars, and 5.1±0.1 GPa in 1 μm diameter pillars, and 4.5±0.2 GPa from nanoindentation. These results are somewhat complicated by hydrogen outgassing since all the micropillars tested were on the same wafer; samples were tested in groups sorted by size. The smallest, 500 nm diameter pillars were tested first, within the first four hours of testing at room temperature, and the largest pillars, 1 μm diameter, were tested within 8 to 12 hours of outgassing at room temperature. Additionally, there were more samples and increased apparent plasticity in the smaller pillars, resulting in more data points for the smaller pillars. This is particularly important for yield stress measurements, as only two of the 1 μm diameter pillars tested had a measurable yield before fracture, as expected due to the larger size [55]. Examples for hydrogen charged pillars with corresponding stress strain curves can be seen in Figure 4.16. The stress strain curves are relatively atypical due to microcracking and resulting sliding, or frictional motion of the pillar top relative to the indenter. All pillar sizes exhibited additional cracking relative to non-charged samples.

The results indicate that microcrack formation, which may also nucleate dislocation plasticity at the micropillar contacts, becomes easier with the addition of hydrogen in uniaxial compression, but does not change much with the triaxial stress state in nanoindentation. The potential explanations for this behavior can relate to either
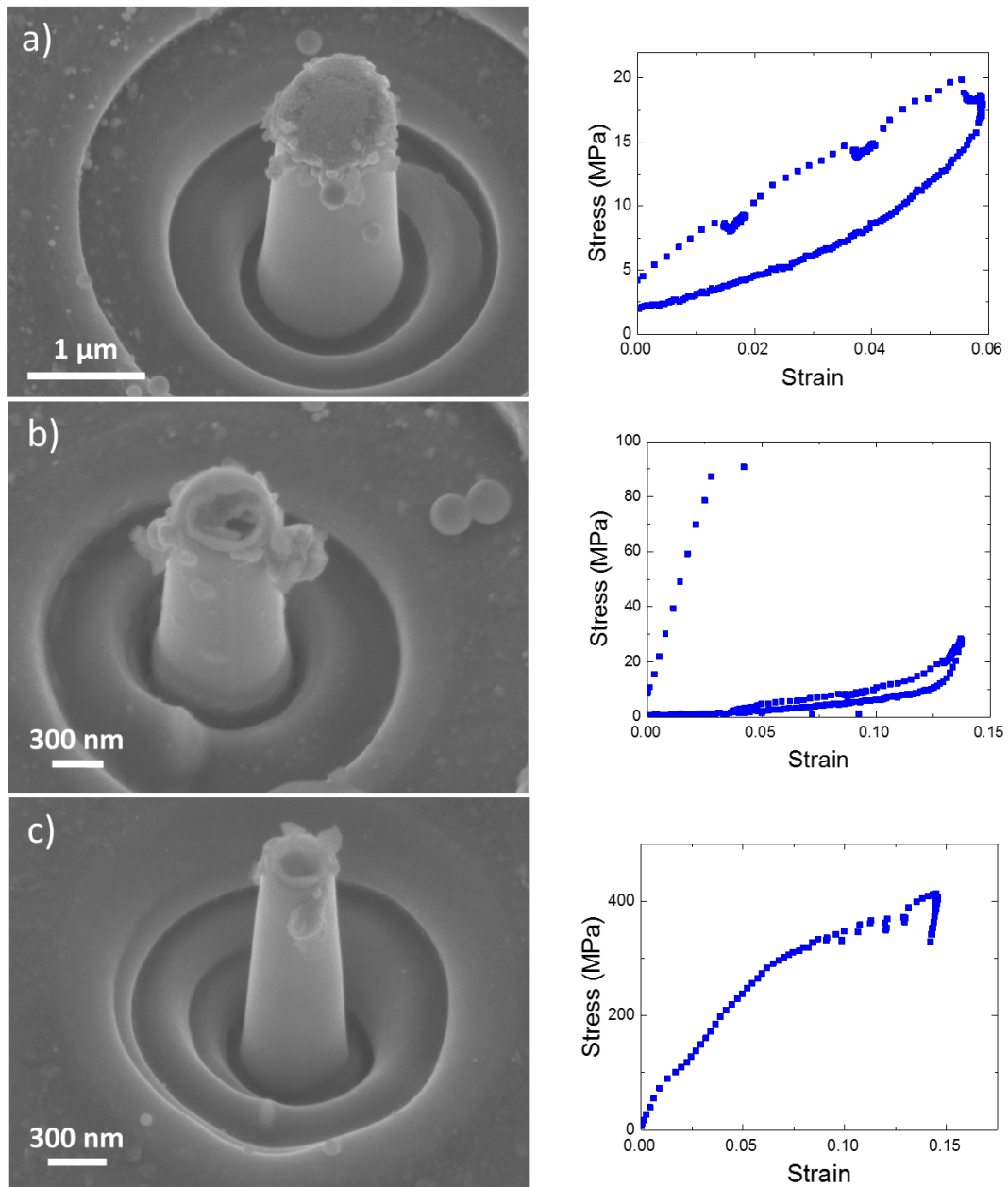
Figure 4.16: Left: post-testing SEM images. Right: corresponding strain curves for hydrogen charged Si pillars with diameters of a) 1 µm, b) 750 nm, c) 500 nm.

113

widening the effective dislocation partial width or increased microcracking due to the uniaxial stress state of the pillar. Hydrostatic stress states are known to inhibit crack formation [246], and there is experimental evidence that impact plastic flow in other materials as evidenced by changes in dislocation activation parameters at higher pressures [247, 248, 249]. This means that areas with internal hydrogen storage should have changes in V*. However, hydrogen outgassing is known to create defect sites at the Si/SiO_2 interface or at the Si surface, leading to increased internal stresses and thus a likelihood of increased cracking relative to non-hydrogen charged materials [250, 243]. Van Arsdell and Brown have shown that K_{Ith}, the stress intensity threshold, in non-hydrogen charged polycrystalline Si MEMS devices is 0.31 MPa*m$^{1/2}$ [200]. The results here indicate that internal stresses in the hydrogen-charged samples are higher than previously reported or that the K_{Ith} has decreased.

Some micropillar compression tests, where some misalignment of the tip with the pillar's center axis, in other words eccentric loading, resulted in pillar fracture near the base, see Figure 4.17 for examples. This is due to the tensile stress fields that result from a
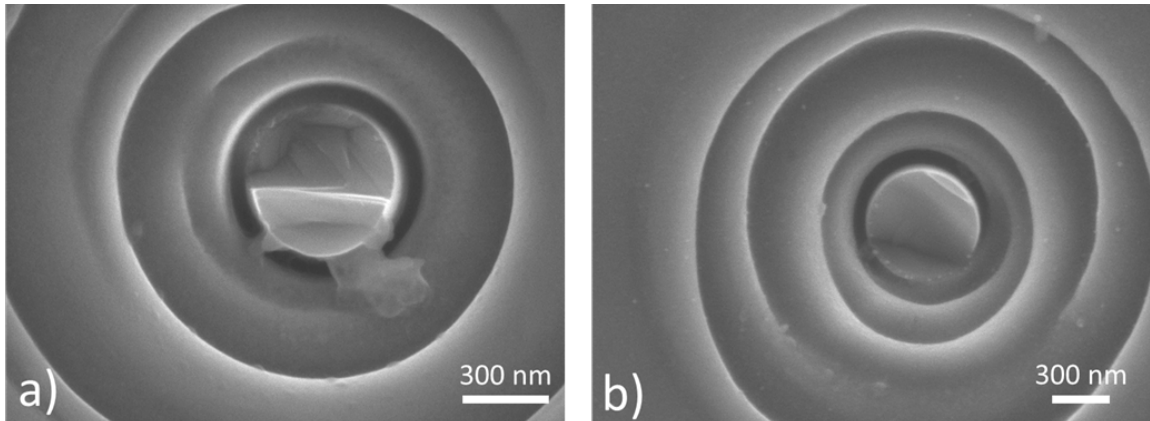
Figure 4.17: Micropillar fracture surfaces of eccentric loaded pillars a) non-hydrogen charged Si and b) hydrogen charged Si showing larger critical crack lengths in non-hydrogen charged Si.

bending moment from the loading conditions. Fractography of the broken pillar bases determined that there is obvious critical crack length that resulted in pillar failure. These dimensions and the load at failure for the compression testing were used to determine a fracture toughness, K_{Ic}. Assuming that K_{Ic} is constant for a given pillar size and the crack opening is very small relative to the pillar length, the stress intensity factor at a crack tip in a bulk square beam is modeled by Bazant as [234]:

$$K_{IC} = \sqrt{\frac{\pi\alpha}{D}}\left[\frac{6Pe}{D}F_M - PF_N\right],$$ 4.7

where D is the relevant thickness dimension, here the pillar diameter, α is the ratio of critical crack length to diameter, P is the modified applied load, e is the eccentricity factor or the length the load is applied relative to the pillar center, and F_M and F_N are functions of the eccentric and normal force respectively, both dependent on α as found in Reference [234]. The simple model for these parameters is shown in Figure 4.18. a, or critical crack length, is measured directly from the pillar fracture surfaces using SEM, but e must be estimated due to the *ex-situ* nature of testing. However, due to the size of the indenter tip and the size of the pillar, e is relatively small relative to pillar diameter. Here, a constant value of 50 nm was used for all pillar sizes. The K_{IC} for non-hydrogen charged specimens was found to be 1.5±0.6 MPa*m$^{1/2}$, though some small dependence on pillar diameter was noted,
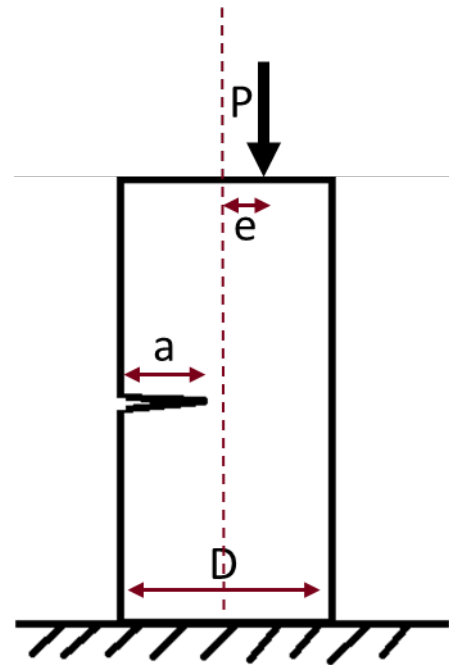
Figure 4.18: Schematic for parameters of eccentric loading for Equation 4.7. Adapted from Reference **[234]**.

115

with smaller pillars having slightly higher average fracture toughness values. However, the scatter for this data is large, as expected, since pillar geometry and stress concentration differences due to taper impact these results.

The K_{IC} for hydrogen charged specimens showed a large dependence on pillar diameter, from 0.66 ± 0.26 MPa*m$^{1/2}$ for 1 μm diameter pillars to 0.11 ± 0.06 MPa*m$^{1/2}$ for 500 nm diameter pillars, all of which are much smaller than the expected values for Si. Complete results for this analysis can be found in Figure 4.19. This evidence supports an embrittlement of Si by hydrogen, and points to an effect of Si/SiO$_2$ interfaces being a stress concentration point leading to increased microcracking [243, 250]. The large standard deviation with these pillars is expected as geometry of the pillar and eccentricity are likely to change throughout testing.

The average crack length and load at failure in non-hydrogen charged samples was larger than that found in the hydrogen charged samples, indicating that K_{IC} is smaller in hydrogen charged samples, and SEM images post-test confirm that microcracking is more likely in hydrogen charged samples. However, increased microcracking would also lead to an increase in local stress concentration sites at the tips of the microcracks, meaning that these sites could more easily nucleate dislocations. It is also possible that the increases seen in the hardness and modulus could partially be due from hydrogen outgassing [240]. The increase in dislocation nucleation at smaller overall stresses due to the microcracks explains the large increase in pillar strain without fracture as K_{IC} is not exceeded. Altogether, this would lead to microcracking nucleated plasticity. Additional investigations, particularly with TEM studies of the micropillars, are needed to validate or
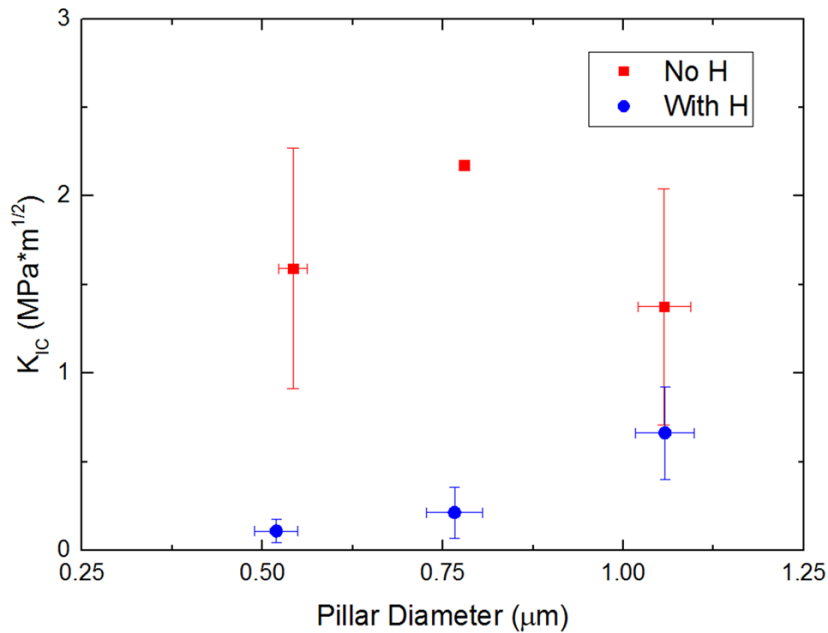
Figure 4.19: Fracture toughness dependence on pillar diameter and hydrogen charging in n-type (100) Si micropillars.

disprove this explanation. However, the fracture toughness values may not be fully accurate in these systems, particularly since local stress values will be inaccurate. Later, another estimation of fracture toughness will be made using the activation volume and effective stresses found in the following section.

4.4.2.2.3   Activation Volume

The results for activation volume for (100) Si nanoindentation and micropillar compression without hydrogen charging are presented in Figure 4.20 and compare well to similar testing by others [66, 56]. In addition, initial results for activation volume in (111) Si pillars are also presented in Figure 4.21 that follow a similar trend to (100) Si pillars, though more work is needed on this material. Si dislocations can operate by partial ($b =$ 0.222 nm) or full dislocations ($b =$ 0.38 nm); however, here partial dislocations were used for the calculations for nanoindentation and micropillar compression. The measured

117
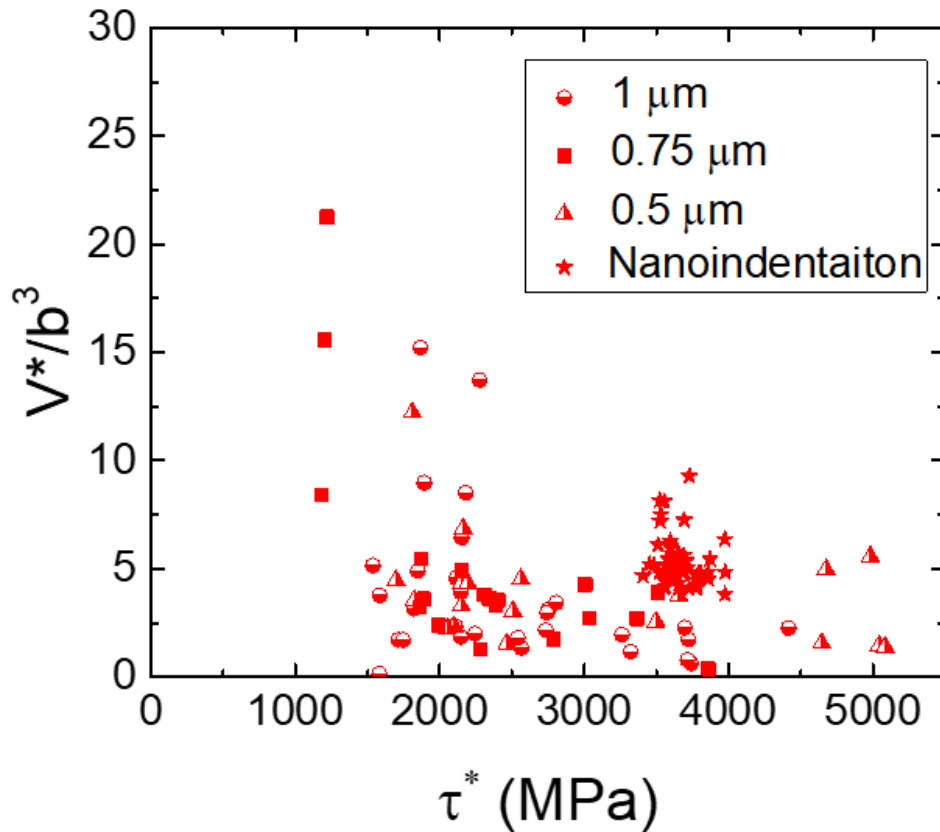
Figure 4.20: Apparent activation volume (V*) normalized by the Burgers vector (b) cubed versus effective stress in non-H charged (100) samples showing effect of stress state in nanoindentation versus micropillar compression as well as the relative independence of pillar diameter.

activation volumes and effective shear stresses indicate that there is an overall higher

energy barrier for dislocation motion in nanoindentation due to back stress effects and

relatively easier dislocation generation at pillar surfaces. This is expected, as constrained

flow in nanoindentation would produce larger back stresses, thus reducing effective

stresses and dislocation emission compared to micropillars. Dislocations in Si are known

to generate at surfaces [203], which would be more prevalent in the micropillar as

compared to nanoindentation samples. In standard, non-hydrogen charged Si, the pillar

diameter did not have a large dependence on activation volume for this relatively small

range of pillar diameters, though both pillar and nanoindentation data sets show some dependence of activation volume on effective stress, as shown in Figure 4.20. After these apparent activation volumes and flow stresses were defined for the standard Si, samples were tested after hydrogen charging.
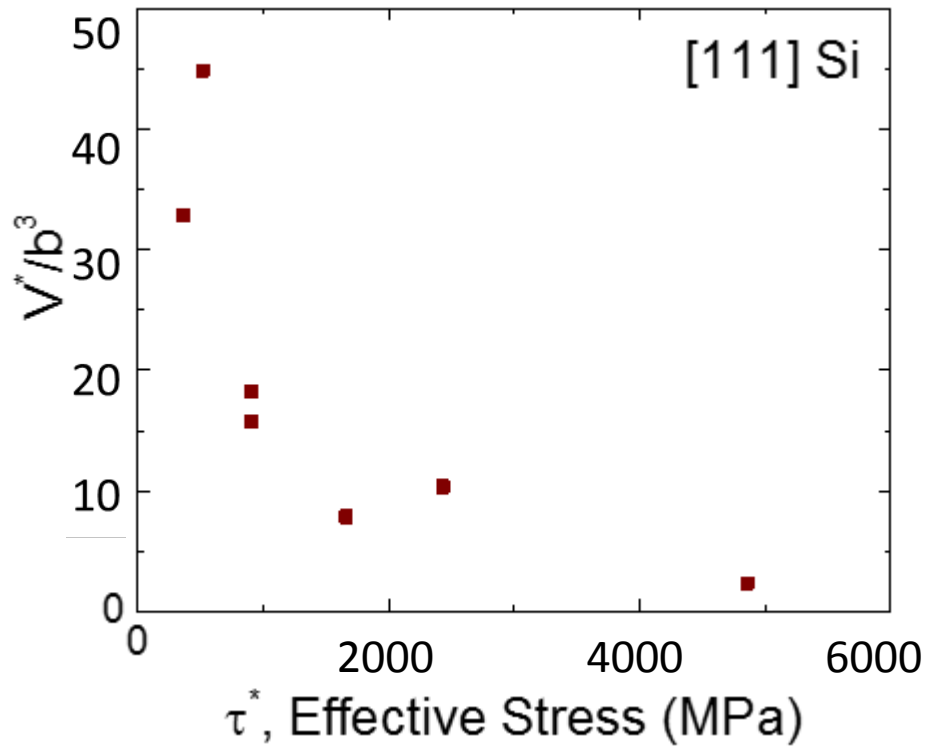
Figure 4.21: Initial results for activation volume in (111) Si micropillars.

Apparent activation volume calculations were impacted by hydrogen charging as shown in Figure 4.22a-b. In nanoindentation, these changes were marked by an increase in flow stress and a general apparent increase in activation volume. Together, this points to an increase in dislocation velocity, which is unexpected, especially with the fracture
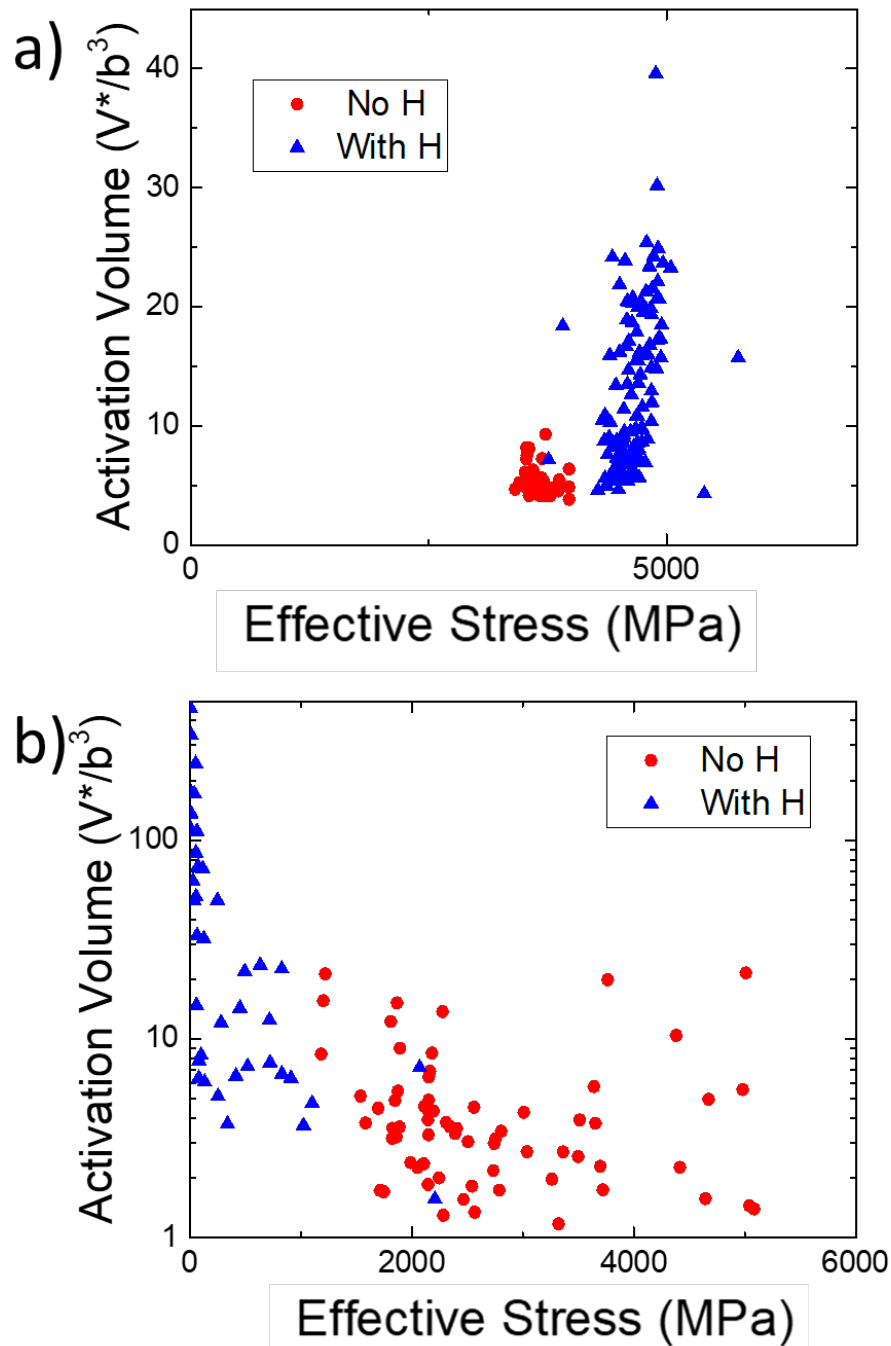
Figure 4.22: Apparent activation volume calculations for (100) Si with and without hydrogen charging of a) nanoindentation and b) micropillar compression. While three sizes of pillars were tested, no observable difference was noted in the activation volume measurements.

toughness results found in the previous section which would indicate decreased dislocation

velocities. Decreasing the dislocation velocity should ultimately decrease dislocation

shielding, making the material more brittle and susceptible to fracture. No direct fracture indications were observed in nanoindentation, likely due to the stress state of the material. However, at the nanoindenter contact edge, where stresses are tensile, this could have introduced microcracking. Furthermore, this could have easily given apparent load drops for activation volumes at low stresses even though the average contact stress was high. The results for V^* and flow stress changes are significantly different from the micropillar compression results where flow stresses were drastically lower and the activation volume was much higher in hydrogen charged samples. Hydrogen charging also produced a higher stress-dependence on activation volume not observed in the control material. However, these calculations show that apparent activation volume is unrealistically large at unrealistically low flow stresses in micropillars. This is explained by microcracking, which allows for sliding in the material and dislocation nucleation. The stress values in Figure 4.22b below about 1 GPa are artificially low due to cracking, which generates very high effective stresses at the crack tips. These V^* and stresses are unrealistic representations of the material behavior in micropillars, however, as flow stresses increase to about 1 GPa as seen in Figure 4.22b, the V^* values overlap with more realistic uncharged hydrogen values. V^* calculations are also somewhat impacted by inaccurate stresses – if the difference in the stresses associated with cracking change, the calculated activation volume will also be impacted. However, it is promising that the normalized activation volume plateaus to a value around 5-2 V^*/b^3, the same values observed in non-hydrogen charged material. Following the mathematical equations in Reference [251], the change in product of V^* and effective stress will correspond to an opposite relative increase or decrease in the

dislocation velocity. There is an average increase in this product with the addition of hydrogen. This also contradicts the fracture toughness calculations found in the previous section. However, better estimations of the effective stresses could help solve these discrepancies, particularly if the stresses due to hydrogen diffusion and local crack tip stresses could be determined.

Table 4.3: Pressure effects on activation volume, taken from other sources.

Material	Pressure (GPa)	V_o^* (b^3)	V_p^* (b^3)	Source
Fe	0.26	1	0.1	[248]
Olivine	1	25	10	[247]
NaCl	10	37	25	[249]
Zn	10	5	2.7	[249]

Nevertheless, for pillars not hydrogen charged, a previous relationship for how increased strength with decreasing pillar size could be used to estimate the activation volumes as indicated in Table 4.3 [252]. Plotting a log-log plot of Table 4.3 shows that there is an inverse relationship with pressure and activation volume. With hydrogen charging, the internal pressure increases, and as shown by previous results, an external hydrostatic pressure can decrease the activation volume by up to a factor of 10 [249, 248]. This trend has been measured in both geological materials, in iron crystals and implied in single crystal Si [249, 248]. Based upon these findings, it was relevant to ascertain if such behavior was consistent with previous findings appropriate to the fracture resistance of single crystal Si. In addition, τ^*V^* must be less than H_0 for thermally activated mechanisms to apply. Average shear stresses and activation volumes were determined for each pillar size for the non-hydrogen charged pillars. Then, the same stresses were assumed

for the hydrogen charged pillars, but a gradient decrease with τ^*V^* was applied to account for pressure effects. With these estimations of τ^* and V^* in hydrogen charged samples, another first order estimation of fracture toughness is possible particularly using the combined micropillar data of hydrogen free samples, considering these are actual effective stresses for pillars. The equation used has been given elsewhere regarding Fe-3% Si, and may be considered relevant to single crystal Si for highly stressed volumes, given by [64, 73]:

$$G_{IC} = \frac{V^*\tau^*\Psi_0}{b^2\dot{\varepsilon}} exp\left\{-\frac{H_0 - \beta V^*\tau^*}{kT}\right\}. \qquad 4.8$$

Here G_{Ic} is a toughness parameter that can be related to fracture toughness by Equation 2.14, T is temperature, β is a geometrical fitting parameter, assumed to be near one, H_0 is the stress-free or thermal activation energy for dislocation nucleation or motion, here 1.4×10^{19} N·m [71], and $\Psi_0/\dot{\varepsilon}$ is the fitting parameter missing from this data set. Ψ_0 is a function including Poisson's ratio, the pre-exponential dislocation velocity, the mobile dislocation density and the plastic strain, $\Psi_0 = f(\nu, v_0, \rho_m, \varepsilon_p)$. $\Psi_0/\dot{\varepsilon}$ is determined to be 23.7 from fitting non-hydrogen charged data of V^* and τ^* found in Table 4.4. The experimental data for non-hydrogen charged samples as well as experimental and estimated appropriate values for V^* and τ^* for hydrogen charged samples are shown in Table 4.4. One can easily obtain fracture toughness values as a function of pillar diameter based upon strength variations. Strengths, as measured for the micropillars, were converted to effective shear stresses assuming partial dislocations and, the activation volumes were calculated. This calculation is much less certain with hydrogen charging data. While the stresses from micropillar testing are low due to the microcracking, internal stresses or some other

mechanism, in the same type of calculation one obtains K_{Ic} to vary with pillar diameter. The results of these calculations using pressure-modified activation volumes, are also shown in Table 4.4.

While this is just a demonstration of a reasonable conjecture, it does strongly imply that hydrogen embrittlement can occur, as is consistent with a decrease in the product of the effective stress and activation volume. The calculations for fracture toughness found in Table 4.3 for hydrogen charged samples, fits for this data shown in Figure 4.23. The resulting calculations from Equation 4.8 using these values of τ^* and V^* to give a first order representation but the reader is cautioned that the pick of two variables of both $\Psi_0/\dot{\varepsilon} =$ 23.7 kg·s/m and $\beta \approx 1$ give considerable leeway in the ability to fit such data.

*Table 4.4 τ^* and V^* Estimate of K_{Ic}. Experimental values as well as estimated values for V^* and τ^* are given for hydrogen-charged micropillars. Estimated values were generated using the assumptions that effective stress increases with hydrogen as noted by nanoindentation while the activation volume decreases due to hydrogen-induced pressure as indicated in Table 4.3. * Uses a different $\Psi_0/\dot{\varepsilon} = 1*10^6$.*

		D (μm)	τ^* (GPa)	V^* (m^3)	K_{Ic} (MPa-m$^{1/2}$)
	w/o H$_2$	1.0	2.2±0.5	7.86x10^{-29}	1.54
		0.75	2.4±0.8	7.08x10^{-29}	0.97
		0.50	3.0±1.2	5.67x10^{-29}	0.63
Exp.	w/H$_2$	1.0	0.020	630x10-29	0.81*
		0.75	0.050	200x10-29	0.35*
		0.50	0.580	160x10-30	0.22*
Est.	w/H$_2$	1.0	2.5±0.5	7.47x10-29	0.69
		0.75	2.7±0.8	6.67x10-29	0.446
		0.50	3.2±1.2	5.28x10-29	0.225
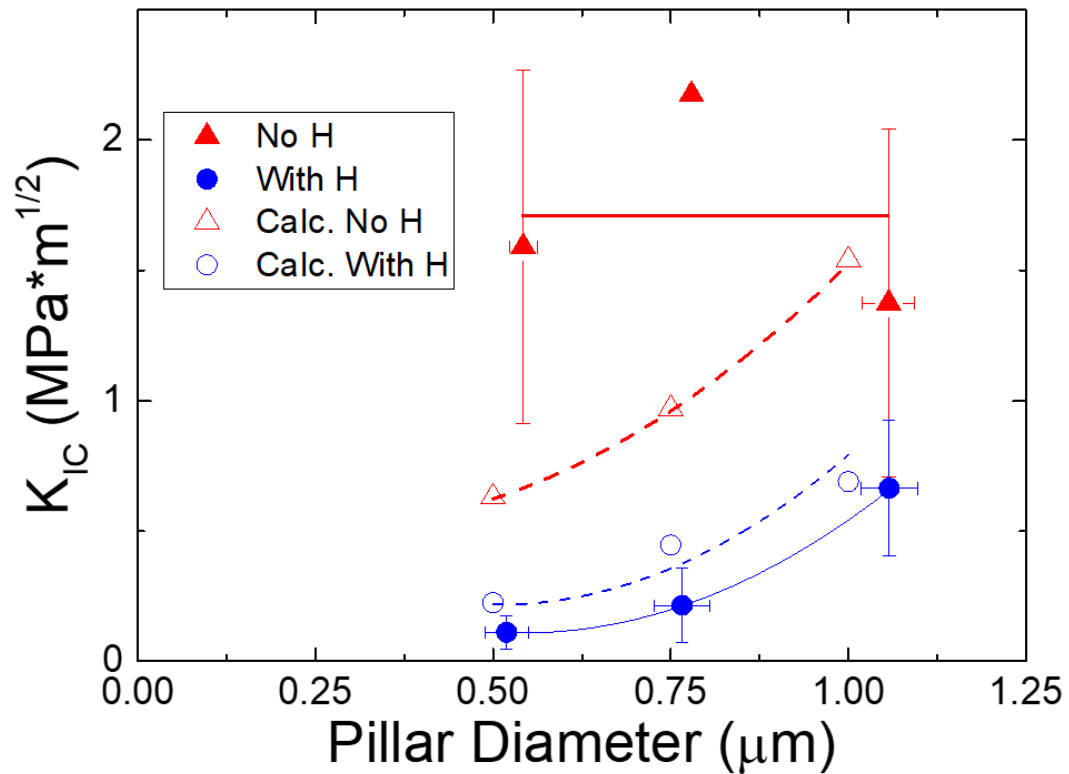
Figure 4.23: Apparent activation volume versus effective stress in non-hydrogen charged samples showing effects of stress state and relative independence of pillar size. Calculated data points are generated using Equation 4.8.

Hydrogen charging appears to lower the fracture toughness of the Si specimens, this supports arguments for an apparent decrease in dislocation velocity, or alternatively this could be pure brittle fracture allowing lower stresses to form microcracks without dislocation nucleation. This is likely partially due to the increased stress present at the Si/SiO_2 interface and suggests that these sites are crack nucleation points or that cracks are present in the system due to hydrogen charging [243, 250]. This is supported by the size dependence of pillar fracture toughness, where smaller pillars exhibit lower fracture toughness, defying the typical trend observed in non-hydrogen charged material. Because

this is a promising approach, it is apparent that more precise models and experimental approaches need to be developed to address these findings.

4.4.2.2.3.1 Elevated Temperature Data

Nanoindentation and micropillar compression tests were completed on the same wafer of Si, the (100) n-type previously discussed. However, these experiments were completed at Los Alamos National Labs in the Center of Integrated Nanotechnology's facilities. A Hysitron TI 950 triboindenter with an xSol high temperature stage was used. This stage has the capabilities of testing materials at temperatures up to 800°C in ambient environments with the aid of an argon shield-gas system to limit reactions from the environment, a reflective metal shield to thermally protect the components of the transducer, and a coolant system that keeps the remainder of the instrument thermally stable. Ambient, 100°C, 200°C, 300°C, and 400°C were used for testing in these experiments. A Helios NanoLab FEI FIB was used for imaging the Si pillars posttest.

Sample mounting is different in this situation; due to the high temperatures of testing, most adhesives are not stable. Instead, a sample is carefully placed directly on a heater imbedded in a large metal plate. Then, a second plate with a small hole, big enough for the indenter tip shaft and between two large plates is placed on top and fixed to the stage through metal clamps. The large mass of the system and direct attachment to the triboindenter stage means that the system is relatively stable from a vibration standpoint. However, it should be noted that high temperature testing is usually associated with more drift in experimental measurements. This is partially due to thermal gradients in the tip when making contact with the sample and very small fluctuations in temperature due to the
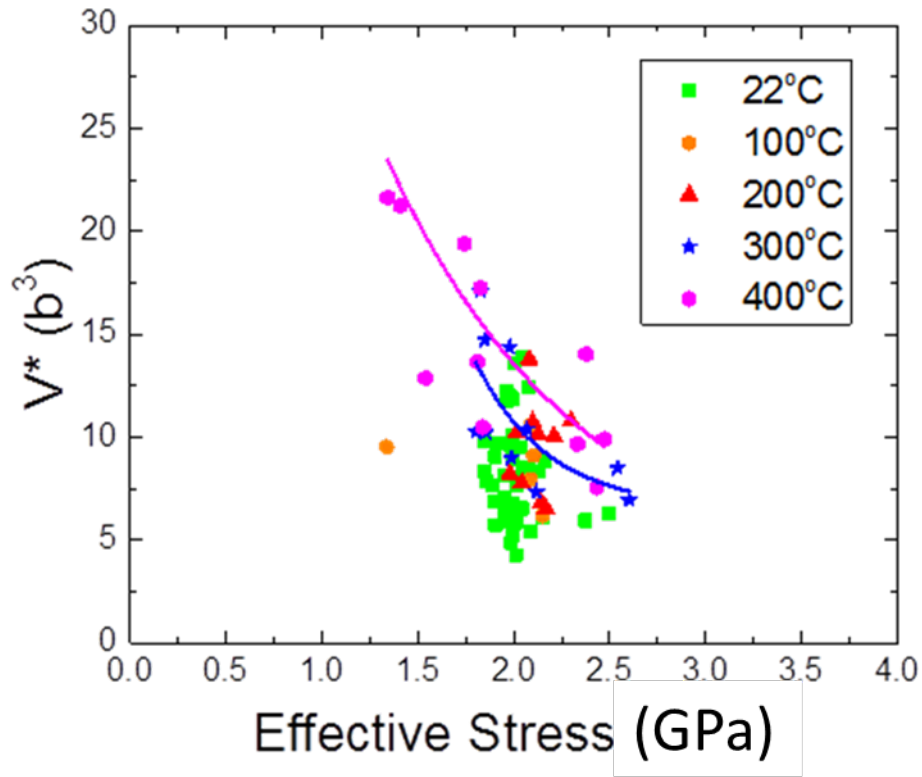
Figure 4.24: Activation volume measurements for Si at elevated temperatures.

PID settings of the Lakeshore device used for temperature control. In addition, the materials subject to the higher temperatures are generally more compliant at higher temperatures. A 10 µm radius of curvature high-temperature conical tip was used for testing the micropillars and a high temperature Berkovich tip was used for nanoindentation. Both tips are made of diamond but have a much longer shaft length than the low temperature tips. A long quartz-cylinder is part of the high temperature tips to enable the tip to reach the sample through the additional equipment needed for high temperature control as well as insuring that tip components that are exposed to the high temperatures do not melt.

Both micropillar testing and nanoindentation testing provides experimental evidence of how the stress state in the material affects dislocation generation and motion and gives information about changes in the activation volume of the material, and with more information could provide a measurement of activation energy. Initial testing results further indicate that there is a definite transition in deformation behavior in Si, where tests at 400°C show very different trends, with a transition to more brittle behavior as temperature decreases. The nanoindentation data, repeated with the same procedures as in the ambient temperature data, show a transition between the relatively scattered data at lower temperatures to an exponential trend as expected in more plastic materials. The higher temperature data also show relatively higher activation volumes at the same effective stresses, though also show a trend of the overall effective stresses decreasing using the same testing strain rates and overall displacements, as shown in Figure 4.24. This indicates that the additional stress-energy needed for deformation is decreasing, and indicates that plastic processes are more energetically favorable relative to the lower temperature tested counterparts.

Testing was also completed on micropillar specimens at elevated temperatures, though only 200°C, 300°C, and 400°C were used for testing in this section of experiments. Qualitatively, the micropillars deformed quite differently over this temperature scale, as seen in Figure 4.25. The micropillars tested at 200°C were visually similar to the micropillars tested at ambient temperatures, with some cracking evident at the top sections

of the pillar. As temperature increased, while fracture behavior was still apparent, more
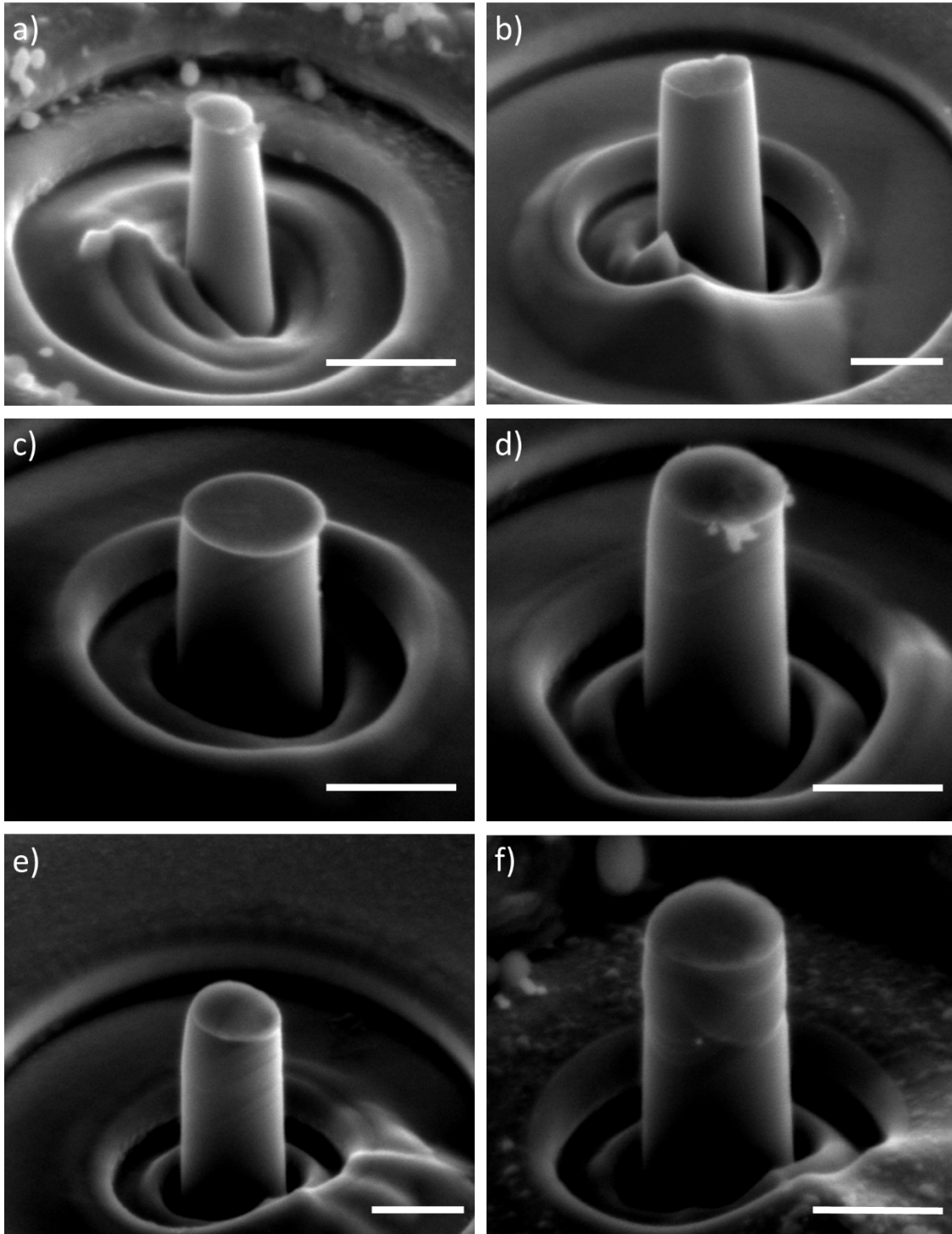
Figure 4.25: Si micropillars tested at various temperatures a-b) 200°C, c-d) 300°C, e-f) 400°C. All scale bars represent 1 µm.
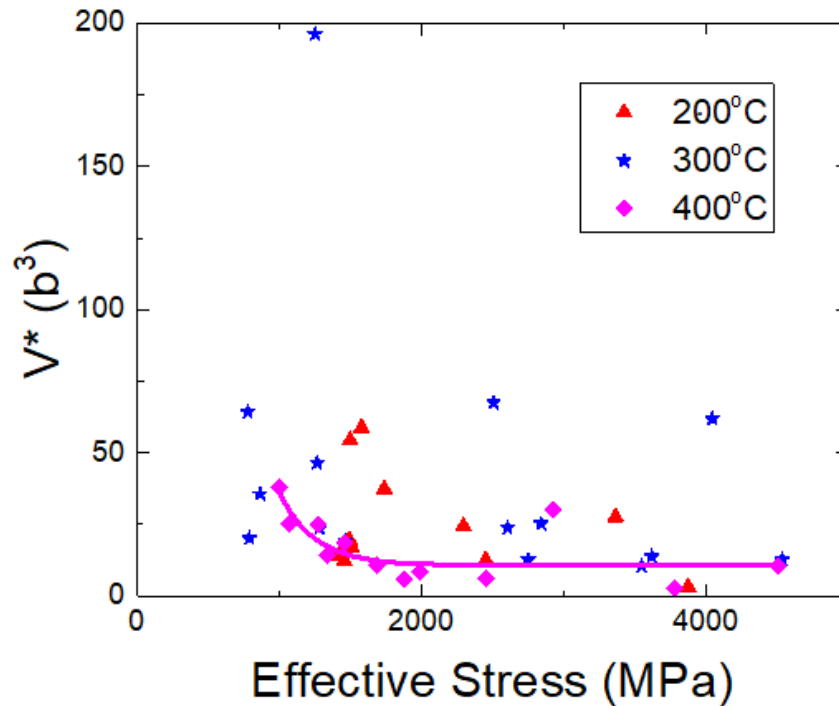
Figure 4.26: Activation volume measurements for micropillars of Si at elevated temperatures.

slip developed. Slip and fracture were apparent at 300°C, and at 400°C multiple slip systems were activated, as shown in Figure 4.25f.

There were also large changes in the measurements of activation volume versus effective stress in micropillars, all results are shown in Figure 4.26. Pillars tested at 400°C showed a consistent trend across effective stress and activation volume, while the remaining pillars showed a scatter that is likely related to cracking phenomenon. There is also a general trend of decreasing activation volume at the same relative effective stresses in the micropillars. Without differentiating the cracking phenomenon from the plastic deformation phenomenon, it is difficult to make conclusions here, other than plastic processes dominating above 400°C. Further samples to fill in the rest of this plot as well as

account for the scatter in the lower-temperature tested specimens could give better insight

on the activation volume, then activation energy that could be determined here.

Chapter 5 : Summary and Conclusions

Throughout this work, the effects of hydrogen on the mechanical properties was investigated in three systems: Sc, Si, and Ni.

5.1 Sc and ScD$_2$

Sc films were produced then deuterium charged. The resulting deuteride films cracked during production and use, prompting mechanical property studies of ScD$_2$ films focusing on elastic modulus, fracture, and size effects observed in the system for future film mechanical behavior modeling efforts. ScD$_2$ films were characterized using XRD, SAM, and EBSD to monitor changes in the films before and after deuterium charging. SEM, nanoindentation, and FIB machined micropillar compression tests were used for mechanical characterization of the ScD$_2$ films. A micropillar diameter-size effect was observed, indicating that film thickness is a relevant tuning parameter for film performance and that grain boundaries are the limiting aspect for fracture in this material. To further define mechanical properties, elastic modulus was determined by micropillar compression and nanoindentation, both techniques resulted in calculated values of approximately 150 GPa. Hardness of ScD$_2$ was also determined through nanoindentation at 4 GPa. The elastic modulus and hardness of the original Sc films from nanoindentation was much smaller than the deuterium charged films, as expected, at 55 GPa and 2 GPa respectively. Impurity content did not impact modulus measurements of the ScD$_2$ films, but large impurities of Al can increase the hardness by 2-3 GPa.

Fracture studies of bulk film cracking as well as compressed, cracked micropillars resulted in fracture toughness around 1.0 MPa-m$^{1/2}$ for almost all pillar dimensions,

substrates, and analysis technique. Despite this relatively low value of fracture toughness, ScD_2 micropillars can have a large degree of plasticity in small volumes and can harden to some degree, demonstrating the ductile and brittle nature of this material. Preliminary Weibull distributions of probability fracture at a given stress in the micropillars are provided. The smallest pillars tested, at 300 nm in diameter, are shown to exhibit higher overall toughness values, and lower fracture probabilities at a given stress.

5.2 Ni

Ni buttons were made through arc melting of Ni shot. This resulted in visibly large grains that could be used for single crystal studies of Ni with the aid of EBSD orientation mapping. Nanoindentation as well as micropillar compression of various grains was attempted with and without thermal hydrogen charging. Ni was also impacted by hydrogen charging. However, micropillars could not be used to determine activation volumes as non-charged samples had large slip bands that were indifferentiable from strain rate jump tests and hydrogen charged samples were destroyed in the hydrogen charging process. However, Ni nanoindentation samples in general had an increased hardness with hydrogen charging, but strain rate sensitivity disappeared with hydrogen charging. This means that though activation volume can be determined repeatedly in nanoindentation without hydrogen charging, that another undetermined method must be used to determine activation volume in hydrogen charged Ni.

5.3 Si

Si wafers were FIB milled into micropillars and both wafer and pillar materials were tested with and without thermal hydrogen charging. Hydrogen charging of (100) n-type Si

with hydrogen resulted in clear changes in mechanical properties, despite material outgassing at room temperature during testing. This shows that Si exposure to hydrogen could have drastic impacts on fracture and plasticity in small volumes, like those generated in MEMS. Nanoindentation results show that hardness, V* and effective stress increase with the addition of hydrogen, initially indicating that dislocation velocity increased. The product of V* and flow stress is also initially shown to increase in micropillar systems, though microcracking in the pillars artificially lowers the effective stresses measured, which should be very high at the crack tips generated. For both nanoindentation and micropillar compression there is a stress effect from hydrogen outgassing that must be considered. With these considerations, both the nanoindentation and micropillar compression testing parameters indicate that the actual dislocation velocity should be decreasing in the hydrogen charged samples.

Some micropillars exhibited catastrophic brittle failure resulting in the pillar fracturing close to the base, but leaving some portion of the micropillar behind. These samples were used to determine fracture toughness with and without hydrogen. Fracture stresses and critical crack lengths in micropillars are shown to decrease significantly with hydrogen charging indicating a decrease in fracture toughness. This evidence further supports the arguments for decreased dislocation velocity with the addition of hydrogen into the system, and bolsters a HEDE mechanism in the material. There appears to be a size-effect with fracture toughness in the hydrogen charged material, that has large impacts on small volumes of Si in environments with hydrogen present. All of these results, though inconclusive from a hydrogen concentration standpoint and inaccurate measures of local

stresses, are consistent with observations that support a HEDE mechanism in Si at small scales.

Chapter 6 : Future Work

This section highlights the main areas where this work could be improved or extended as well as mentions other areas of parallel study that are of interest.

6.1 ScD$_2$

More work needs to be completed in this area of study further defining impacts of grain boundaries on the fracture properties of the ScD$_2$ films. Especially since there are inconsistencies in the expectations of the data – where 800 nm diameter pillars have lower toughness and higher probability of failure than larger 1600 nm diameter pillars. While this is likely attributed to the small sample sizes tested in these studies, there could be a critical flaw density that is not captured from this sample size. Additional testing could also be of interest on this material. Particularly, it would be interesting to test smaller pillars, and to do a careful examination of orientation dependence on modulus, hardness, and fracture toughness. In addition, testing completed on bicrystalline pillars could also give better insight on the cohesive energy between grains and would lead to an interesting analysis of fracture toughness in pillars with pre-existing flaws. Initial experiments were completed on the impacts of impurities on the mechanical properties of the material – there are no observable impacts on the modulus of the material, but the hardness is somewhat impacted meaning that perhaps fracture behavior could change as well [253]. Experiments on micropillars or generation of new films with various impurity contents on quartz substrates could show an impact on fracture toughness. This could be very relevant to industrial applications where source material could contain impurities that would impact device performance. It would also be interesting to see the dislocation structures in the samples

before and after testing – particularly to see how dislocations are distributed relative to grain boundaries. Initial TEM lift-outs of material have been made as seen in Figure 6.1, but high resolution imaging and analysis needs to be completed as these images are insufficient to determine dislocation structures in the material. Twinning has been observed in other similar materials [95] and it would be beneficial to observe twins, dislocation
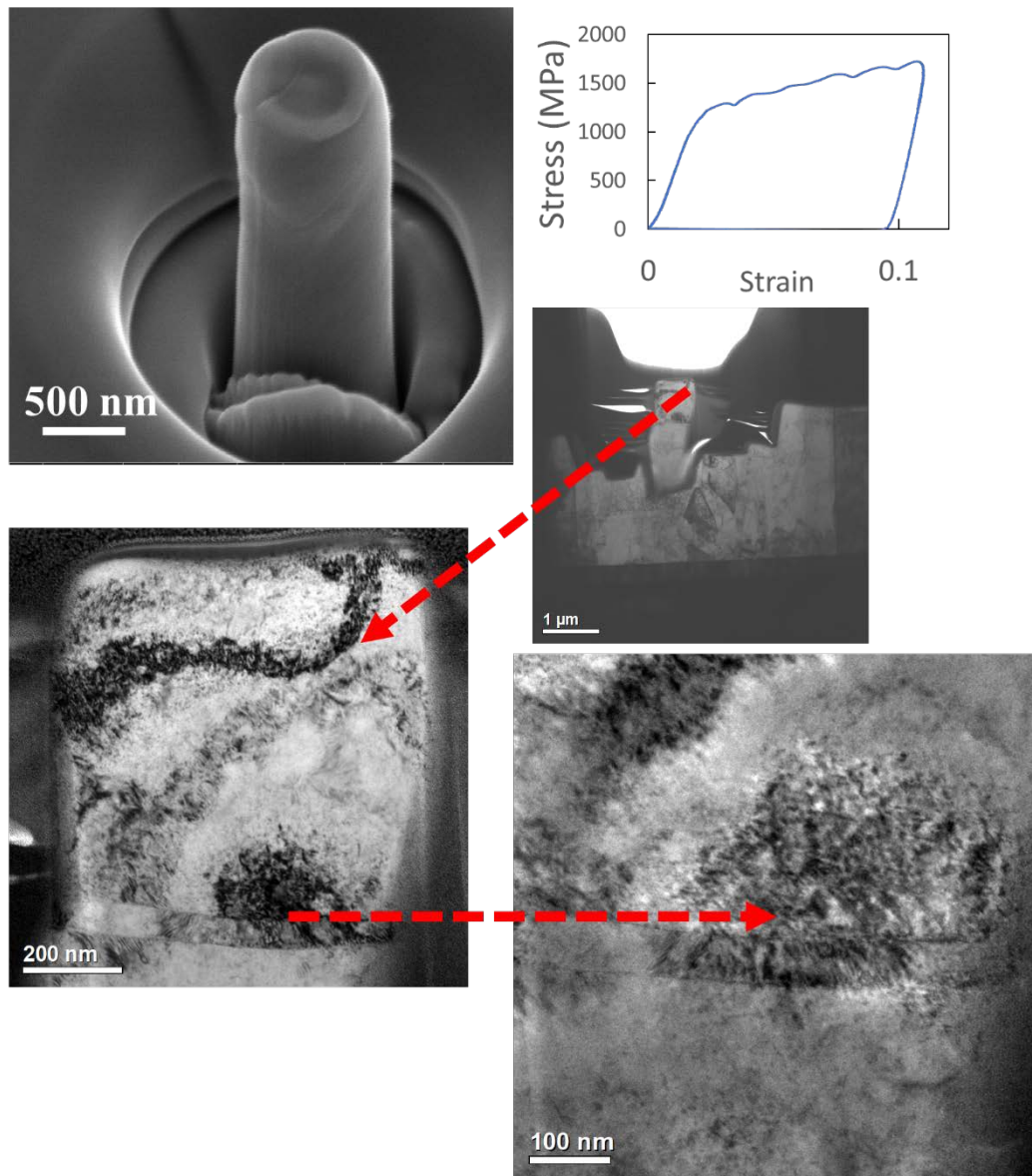
Figure 6.1: ScD$_2$ post tested micropillar SEM image, stress strain curve, TEM liftout, and two subsequent higher magnification TEM images of a ScD$_2$ pillar.

137

structures and relative plasticity of grains of materials in the small, 300 nm diameter pillars, versus the larger multi-grained pillars.

6.2 Ni

This section by far is the least explored out of the main topics in this thesis. Further orientation studies and additional hydrogen charging experiments particularly in micropillar specimens would be useful to elucidate material behavior and further define hydrogen impacts in single crystals of Ni at small scales. The reasons why Ni pillars did not survive the hydrogen-charging process is unknown, but recent studies on Ni have shown that the fracture toughness of a single grain of material is greatly reduced [199]. Having additional experiments isolating grain behavior as well as studying orientation effects with this property could be of extreme interest for Ni-alloy materials in hydrogen environments. It would also be of interest to make TEM samples of the samples tested here to look at dislocation structures beneath nanoindents to assess hydrogen effects on deformed microstructures.

6.3 Si

Additional testing in this material would be useful to further define size effects, particularly with hydrogen-charged, smaller micropillars. These experiments could also be greatly improved by determining actual hydrogen concentration in the samples as well as better defining the concentrations of hydrogen needed to impact mechanical properties significantly. Other crystallographic orientations, dopant concentrations, and dopant types might also be useful, particularly when considering mapping fracture mechanisms in a 3D space as discussed in Chapter 2. Lastly, TEM imaging could also be useful here – imaging

dislocations and the relative differences in the hydrogen and non-hydrogen charged samples are likely to give further insight on material behavior.

Another area of interest that was pursued but not mentioned in this work is an additional modification of Si to increase the dislocation density in the material and further test hydrogen effects. This could be accomplished by shot peening or deforming the material at a high temperature to facilitate dislocation mobility and generation, and could be a route to increasing hydrogen concentrations in the material as well as impact fracture properties even further.

High temperature testing of Si with strain rate jump testing could also elucidate information about the activation energy of dislocation motion in the material and could further prove and specify DBT in the material. Further analysis and additional testing at elevated temperatures could further fill the 3D fracture map as demonstrated in Chapter 2.

References

[1] D. Teirlinck, F. Zok, J. Embury and M. Ashby, "Fracture mechanism maps in stress space," *Acta Metallurgica,* vol. 36, pp. 1213-1228, 1988.

[2] C. Renshaw, N. Golding and E. Schulson, "Maps for brittle and brittle-like failure in ice," *Cold Regions Science and Technology,* vol. 97, pp. 1-6, 2014.

[3] M. Ashby, "A first report on deformation-mechanism maps," *Acta Metallurgica,* vol. 20, pp. 887-897, 1972.

[4] E. Hintsala, C. Teresi and W. Gerberich, "Linking nanoscales and dislocation shielding to the ductile-brittle transition of silicon," *Metallurgical and Materials Transations A,* vol. 47, pp. 2839-5843, 2016.

[5] W. Ko, "Trends and frontiers of MEMS," *Sensors and Actuators A,* vol. 136, no. 1, pp. 62-67, 2007.

[6] R. Bogue, "Recent developments in MEMS sensors: a review of applications, markets, and technologies," *Sensor Review,* vol. 33, no. 4, pp. 300-304, 2013.

[7] D. Fonseca and M. Sequera, "On MEMS reliability and failure mechanisms," *Internationaly Journal of Quality, Statistics and Reliability,* vol. 2011, p. 820243, 2011.

[8] D. Martinez-Martinez and J. De Hosson, "On the deposition and properties of DLC protective coatings on elastomers: A critical review," *Surface Coatings Technology,* vol. 258, pp. 677-690, 2014.

[9] M. Kennedy, N. Moody, M. Clift, D. Adams, L. Espada, D. Kammler, E. Reedy Jr. and D. Bahr, "Adhesion and fracture of scandium deuteride films," *Effects of Hydrogen on Materials, Proceedings of the 2008 International Hydrogen Conference (ASM International),* vol. 8, pp. 710-717, 2009.

[10] A. Volinsky, J. Vella and W. Gerberich, "Fracture toughness, adhesion and mechanical properties of low-K dielectric thin films measured by nanoindentation," *Thin Solid Films,* vol. 429, no. 1-2, pp. 201-210, 2003.

[11] C. Mastrangelo, "Adhesion-related failure mechanisms in micromechanical devices," *Tribology Letters,* vol. 3, no. 3, pp. 223-238, 1997.

[12] T. Anderson, Fracture Mechanics Fundamentals and Applications, Boca Raton: Taylor and Francis Group, 2005.

[13] W. Callister, Materials Science and Engineering an Introduction, USA: John Wiley and Sons, Inc., 2007.

[14] R. Schwarzer and J. Sukkau, "Electron back scattered diffraction: current state, prospects, and comparison with x-ray diffraction texture measurement," *The Banaras Metallurgist,* vol. 18, pp. 1-11, 2013.

[15] J. Weertman and J. R. Weertman, Elementary Dislocation Theory, New York: Oxford University Press, 1992.

[16] V. Tempe, "Probleme der spannungsverteilung in ebenen systemen, einfach gelost mit hilfe der airyschen funktion," *Zeitschrift fur Mathematik und Physik,* vol. 52, pp. 348-383, 1905.

[17] E. Orowan, "Zur kristallplastizitat. III," *Zeitschrift fur Physik,* vol. 89, no. 9, pp. 634-359, 1934.

[18] M. Polanyi, "Uber eine art gitterstorung, die einen kristall plastisch machen konnte," *Zeitschrift fur Physik,* vol. 89, no. 9, pp. 660-664, 1934.

[19] G. Taylor, "The mechanism of plastic deformation of crystals. Part I. Theoretical," *Proceedings of the Royal Society of London A,* vol. 145, no. 855, pp. 362-387, 1934.

[20] D. Hull and D. Bacon, Introduction to Dislocations, Exeter: Wheaton and C. Ltd., 1984.

[21] M. Duesbery and B. Joos, "Dislocation motion in silicon: the shuffle-glide controversy," *Philosophical Magazine Letters,* vol. 74, no. 4, pp. 253-258, 1996.

[22] R. Peierls, "The size of a dislocation," *Proceedings of the Physics Society,* vol. 52, no. 1, pp. 34-37, 1940.

[23] F. Nabarro, "Dislocations in a simple cubic lattice," *Proceedings of the Physics Society,* vol. 59, no. 2, pp. 256-272, 1947.

[24] A. Griffith, "The phenomena of rupture and flow in solids," *Philosophical Transactions of the Royal Society A,* vol. 221, no. 582-593, pp. 163-198, 1921.

[25] C. Inglis, "Stresses in a plate due to the presence of cracks and sharp corners," in *Institution of Naval Architects*, 1913.

[26] G. Irwin, "Fracture dynamics," in *Fracturing of Metals, American Society for Metals*, Cleveland, OH, 1948.

[27] E. Orowan, "Fracture and strength of solids," *Reports on Progress in Physics,* vol. 12, pp. 185-232, 1948.

[28] G. Irwin, "Onset of fast crack propogation in high strength steel and aluminum alloys," in *Proc. 2nd Sagamore Conference Ordinance Materials*, Syracuse, 1956.

[29] J. Pokluda and P. Sandera, Micromechanisms of Fracture and Fatigue in a multiscale context, London: Springer, 2012.

[30] M. Janseen, J. Zuidema and R. Wanhill, Fracture Mechanics, Delft: VSSD, 2002.

[31] A. Booth and S. Roberts, "The brittle-ductile trasition in gamma-TiAl single crystals," *Acta Materialia,* vol. 45, no. 3, pp. 1045-1053, 1997.

[32] J.-Y. Kim and J. Greer, "Tensile and compressive behavior of gold and molybdenum single crystals at the nano-scale," *Acta Materialia,* vol. 57, no. 17, pp. 5245-5253, 2009.

[33] D. Harvey, J. Terrell and T. Sudarshan, "Hydrogen effects on the ductile to brittle transition behaviour of 21-6-9 stainless steel," *Journal of Materials Science,* vol. 29, pp. 5485-5490, 1994.

[34] P. Hirsch and S. Roberts, "Comment on the brittle-to-ductile transition: a cooperative dislocation generation instability; dislocation dynamics and the strain-rate dependence of the transition temperature," *Acta Materialia,* vol. 44, no. 6, pp. 2361-2371, 1996.

[35] M. Tanaka, E. Tarelton and S. Roberts, "The brittle-ductile transition in single crystal iron," *Acta Materialia,* vol. 56, no. 18, pp. 5123-5129, 2008.

[36] A. Giannattasio, Z. Yao, E. Tarleton and S. Roberts, "Brittle-ductile transitions in polycrystalline tungsten," *Philosophical Magazine,* vol. 90, no. 30, pp. 3947-3959, 2010.

[37] W. Hosford, Mechanical Behavior of Materials, Cambridge: Cambridge University Press, 2010.

[38] L. Botvina, E. Kolokolov and P. Koshelev, "Determining the ductile-brittle transition temperature in different types of tests," *Metal Science and Heat Treatment,* vol. 17, no. 7, pp. 570-574, 1975.

[39] J. Mason, A. Lund and C. Schuh, "Determining the activation energy and volume for the onset of plasticity during nanoindentation," *Physical Review B,* vol. 73, p. 054102, 2006.

[40] D. Kiener, C. Motz, T. Schoberl, M. Jenko and G. Dehm, "Determination of Mechanical Properties of Copper at the Micron Scale," *Advanced Engineering Materials,* vol. 8, no. 11, pp. 1119-1125, 2006.

[41] W. Gerberich, W. Mook, C. Perrey, C. Carter, M. Baskes, R. Mukherjee and A. Gidwani, "Superhard silicon nanospheres," *Journal of the Mechanics and Physics of Solids,* vol. 51, no. 6, pp. 979-992, 2003.

[42] C. Schuh, "Nanoindentation studies of materials," *Materials Today,* vol. 9, no. 5, pp. 32-40, 2006.

[43] W. Oliver and G. Pharr, "An improved technique for determining hardness and elastic modulus using load and displacement sensing indentation experiments," *Journal of Materials Research,* vol. 7, no. 6, pp. 1564-1583, 1992.

[44] W. Nix and H. Gao, "Indentation size effects in crystalline materials: A law for strain gradient plasticity," *Journal of Mechanics Physics Solids,* vol. 46, no. 3, pp. 411-425, 1998.

[45] W. Gerberich, J. Michler, W. Mook, R. Ghisleni, F. Ostlund, D. Stauffer and R. Ballarini, "Scale effects for strength, ductility, and toughness in "brittle" materials," *Journal of Materials Research,* vol. 24, no. 3, pp. 898-906, 2008.

[46] F. Ostlund, P. Howie, R. Ghisleni, S. Korte, K. C. W. Leifer and J. Michler, "Ductile-brittle transition in micropillar compression of GaAs at room temperature," *Philosophical Magazine,* vol. 91, no. 7-9, pp. 1190-1199, 2011.

[47] J. Ye, J. Lu, Y. Yang and P. Liaw, " Study of the intrinsic ductile to brittle transition mechanism of metallic glasses," *Acta Materialia,* vol. 57, no. 20, pp. 6037-6046, 2009.

[48] J. Rabier, A. Montagne, J. Wheeler, J. Demenet, J. Michler and R. Ghisleni, "Silicon micropillars: high stress plasticity," *Physica Status Solidi,* vol. 10, no. 1, pp. 11-15, 2013.

[49] P. Veyssiere, J. Rabier, J. Demenet and J. Castaing, Deformation of Ceramic Materials II, Plenum Press: New York, 1984.

[50] K. Yasutake, S. Shimizu, M. Umeno and H. Kawabe, "Velocity of twinning partial dislocations in silicon," *Journal of Applied Physics,* vol. 61, no. 3, pp. 940-946, 1987.

[51] P. Hirsch, S. Roberts and J. Nye, "Modelling plastic zones and the brittle-ductile transition," *Philosophical Transactions of the Royal Society A,* vol. 355, pp. 1991-2002, 1997.

[52] W. Mook, J. Nowak, C. Perrey, C. Carter, R. Mukherjee, S. Girshick, P. McMurry and W. Gerberich, *Physical Review B,* vol. 75, p. 214112, 2007.

[53] E. Bitzek and P. Gumbsch, "Mechanisms of dislocation multiplication at crack tips," *Acta Materialia,* vol. 61, pp. 1394-1403, 2013.

[54] W. Kang and M. Saif, "In situ study of size and temperature dependent brittle-to-ductile transition in single crystal silicon," *Advanced Functional Materials,* vol. 23, pp. 713-719, 2013.

[55] F. Ostlund, K. Rzepiejewska-Malyska, K. Leifer, L. Hale, Y. Tang, R. Ballarini, W. Gerberich and J. Michler, "Brittle-to-ductile transision in uniaxial compression of silicon pillars at room temperature," *Advanced Functional Materials,* vol. 19, no. 15, pp. 2439-2444, 2009.

[56] J. Rabier, L. Pizzagalli and J. Demenet, "Dislocations in silicon at high stress," *Dislocations in Solids,* vol. 16, pp. 47-108, 2010.

[57] A. Wagner, E. Hintsala, P. Kumar, W. Gerberich and A. Mkhoyan, "Mechanisms of plasticity in near-theoretical strength sub-100 nm Si nanocubes," *Acta Materialia,* vol. 100, pp. 256-265, 2015.

[58] D.-M. Tang, C.-L. Ren, M.-S. Wang, X. Wei, N. Kawamoto, C. Liu, Y. Bando, M. Mitome, N. Fukata and D. Golberg, "Mechanical properties of Si nanowires as revealed by in situ transmission electron microscopy and molecular dynamics simulations," *Nano Letters,* vol. 12, no. 4, pp. 1898-1904, 2012.

[59] Y. Zhu, F. Xu, W. Qin, W. Fung and W. Lu, "Mechanical properties of vapor-liquid-solid synthesized silicon nanowires," *Nano Letters,* vol. 9, no. 11, pp. 3934-3939, 2009.

[60] K. Zheng, X. Han, L. Wang, Y. Zhang, Y. Yue, Y. Qin, X. Zhang and Z. Zhang, "Atomistic mechanisms governing the elastic limit and the incipient plasticity of bending Si nanowires," *Nano Letters,* vol. 9, no. 6, pp. 2471-2476, 2009.

[61] S. Hoffmann, I. Utke, B. Moser, J. Michler, S. Christiansen, V. Schmidt, S. S., P. Werner, U. Gosele and C. Ballif, "Measurement of the bending strength of vapor-liquid-solid grown silicon nanowires," *Nano Letters,* vol. 6, no. 4, pp. 622-625, 2006.

[62] G. Stan, S. Krylyuk, A. Davydov, I. Levin and R. Cook, "Ultimate bending strength of silicon nanowires," *Nano Letters,* vol. 12, no. 5, pp. 2599-2604, 2012.

[63] R. Hull, Properties of Crystalline Silicon, London: INSPEC, 1999.

[64] E. Hintsala, C. Teresi, A. Wagner, K. Mkhoyan and W. Gerberich, "Fracture transitions in iron: Strain rate and environmental effects," *Journal of Materials Research,* vol. 29, pp. 1513-1521, 2013.

[65] A. Beaber, J. Nowak, O. Ugurlu, W. Mook, S. Girshick, R. Ballarini and W. Gerberich, "Smaller is tougher," *Philosophical Magazine,* vol. 91, pp. 1179-1189, 2011.

[66] H. Feng, Q. Fang, L. Zhang and Y. Liu, "Special rotational deformation and grain size effect on fracture toughness of nanocrystalline materials," *International Journal of Plasticity,* vol. 42, pp. 50-64, 2013.

[67] P. Pirouz, J. Demenet and M. Hong, "On transition temperatures in the plasticity and fracture of semiconductors," *Philosophical Magazine A,* vol. 81, pp. 1207-1227, 2001.

[68] A. George and G. Champier, "Velocities of screw and 60-degree dislocations in n- and p-type silicon," *Physica Status Solidi,* vol. 53, pp. 529-540, 1979.

[69] J. Patel, L. Testardi and P. Freeland, "Electronic effects on dislocation velocities in heavily doped silicon," *Physical Review B,* vol. 53, pp. 3548-3557, 1976.

[70] M. Kiran, T. Tran, L. Smillie, B. Haberl, D. Subianto, J. Williams and J. Bradby, "Temperature-dependent mechanical deformation of silicon at the nanoscale: Phase transformation versus defect propagation," *Journal of Applied Physics,* vol. 117, p. 205901, 2015.

[71] T. Ando, T. Takumi, S. Nozue and K. Suo, "Fracture toughness of Si thin film at very low temperatures by tensile test," in *MEMS 2011 IEEE 24th International Conference*, 436-439, 2011.

[72] K. Kang and W. Cai, "Size and temperature effects on the fracture mechanisms of silicon nanowires: Molecular dyamics simulations," *International Journal of Plasticity,* vol. 26, pp. 1387-1401, 2010.

[73] W. Gerberich, D. Stauffer, A. Beaber and N. Tymiak, "A brittleness transition in silicon due to scale," *Journal of Materials Research,* vol. 27, no. 3, pp. 552-561, 2012.

[74] J. Weertman and J. Weertman, "High temperature creep of rock and mantle viscosity," *Annual Review of Earth Planetary Sciences,* vol. 3, pp. 293-315, 1975.

[75] A. Cottrell and B. Bilby, "Dislocation theory of yielding and strain ageing," *Proceedings of the Physical Society A,* vol. 62, no. 1, p. 49, 1949.

[76] Y. Yamashita, F. Jyobe, Y. Kamiura and K. Maeda, "Hydrogen enhanced dislocation glides in silicon," *Physica Status Solidi A,* vol. 1999, pp. 27-34, 1999.

[77] H. Kolar, J. Spence and H. Alexander, "Observation of moving dislocation kinks and unpinning," *Physical Review Letters,* vol. 77, pp. 4031-4034, 1996.

[78] K. Kusters and H. Alexander, "Photoplastic effect in silicon," *Physica B+C,* vol. 116, pp. 594-599, 1983.

[79] T. Namazu, Y. Isono and T. Tanaka, "Plastic deformation of nanometric single crystal silicon wire in AFM bending test at intermediate temperatures," *Journal of Microlectromechanical Systems,* vol. 11, pp. 125-135, 2002.

[80] B. Moser, K. Wasmer, L. Barbieri and J. Michler, "Strength and fracture of Si micropillars: a new scanning elecron microscopy-based micro-compression test," *Journal of Materials Research,* vol. 22, no. 4, pp. 1004-1011, 2007.

[81] D. Kiener and A. Minor, "Source truncation and exhaustion: Insights from quantitative in situ TEM tensile testing," *Nano Letters,* vol. 11, no. 9, pp. 3816-3820, 2001.

[82] C. Frick, B. Clark, S. Orso, A. Schneider and E. Arzt, "Size effect on strength and strain hardnening of small-scale [111] nickel compression pillars," *Materials Science and Engineering A,* vol. 489, no. 1-2, pp. 319-329, 2008.

[83] A. Minor, J. Morris Jr and E. Stach, "Quantitative in situa nanoindentation in an electron microscope," *Applied Physics Letters,* vol. 79, no. 11, pp. 1625-1627, 2001.

[84] R. Nelmes and M. McMahon, "High pressure in semiconductor physics," *Semiconductors and Semimetals,* vol. 54, pp. 177-180, 1998.

[85] Q. Wei, S. Cheng, K. Ramesh and E. Ma, "Effect of nanocrystalline and ultrafine grain sizes on the strain rate sensitivity and activation volume: FCC versus BCC metals," *Materials Science and Engineering A,* vol. 381, pp. 71-79, 2004.

[86] A. Lasia, "On the mechanisms of hydrogen absorption reaction," *Journal of Electroananlytical Chemistry,* vol. 593, no. 1-2, pp. 159-166, 2006.

[87] A. Borgschulte, R. Germaud and Griessen, "Interplay of diffusion and dissociation mechanisms during hydrogen absorption in metals," *Physical Review B,* vol. 78, p. 094106, 2008.

[88] W. Mueller, J. Blackledge and G. Libowitz, Metal Hydrides, New York: Academic Press, 1968.

[89] S. Jo, J. Kang, X.-M. Yan, W. J.M., J. Ekerdt, J. Keto and J. Lee, "Direct absorption of gas-phase atomic hydrogen by Si(100): A narrow temperature window," *Physical Review Letters,* vol. 85, no. 10, pp. 2144-2147, 2000.

[90] M. Stavola, "Hydrogen diffusion and solubility in c-Si," in *Properties of Crystalline Silicon*, London, INSPEC, 1997, pp. 511-521.

[91] M. Louthan, G. Caskey, J. Donovan and D. Rawl, "Hydrogen embrittlement of metals," *Materials Science and Engineering,* vol. 10, pp. 357-368, 1972.

[92] W. Johnson, "On some remarkable changes produced in iron and steel by the action of hydrogen and acids," *Proceedings of the Royal Society of London,* vol. 23, pp. 168-179, 1874.

[93] C. Zappe and C. Sims, "Hydrogen embrittlement, internal stress, and defects in steel," *Transactions of AIME,* vol. 145, pp. 225-259, 1941.

[94] B. Sakintuna, F. Lamari-Darkrim and M. Hirscher, "Metal hydride materials for solid hydrogen storage: A review," *International Journal of Hydrogen Energy,* vol. 32, no. 9, pp. 1121-1140, 2007.

[95] H. Birnbaum, "Mechanical properties of metal hydrides," *Journal of the Less Common Metals,* vol. 104, no. 1, pp. 31-41, 1984.

[96] M. Louthan, "Hydrogen embrittlement of metals: A primer for the failure analyst," *Journal of Failure Analysis and Prevention,* vol. 8, no. 3, pp. 289-307, 2008.

[97] J. Lufrano, P. Sofronis and H. Birnbaum, "Modeling of hydrogen and elastically accomidated hydride formation near a crack tip," *Journal of Mechanics Physics Solids,* vol. 44, no. 2, pp. 179-205, 1996.

[98] D. Shih, I. Robertson and H. Birnbaum, "Hydrogen embrittlement of alpha titanium: In situ TEM studies," *Acta Metallurgica,* vol. 36, no. 1, pp. 111-124, 1988.

[99] K. S. Chan, "An assessment of delayed hydride cracking in zirconium alloy cladding tubes under stress transients," *International Materials Review,* vol. 58, no. 6, pp. 349-373, 2013.

[100] H. Chu, S. Wu and R. Kuo, "Hydride reorientation in Zircaloy-4 cladding," *Journal of Nuclear Materials,* vol. 373, pp. 319-327, 2008.

[101] H. Birnbaum, "Mechanisms of hydrogen related fracture of metals," *Hydrogen Effects on Material Behavior,* p. 693, 1990.

[102] C. Beachem, "A new model for hydrogen-assisted cracking (hydrogen "embrittlement")," *Metallurgical Transactions,* vol. 3, p. 437, 1972.

[103] H. Birnbaum and P. Sofronis, "Hydrogen Effects in Materials," in *TMS, Warrendale, PA*, 1996.

[104] S. Lynch, "Environmentally assisted cracking: Overview of evidence for an adsorption-induced localised-slip process," *Acta Metallurgica,* vol. 34, pp. 2639-2661, 1988.

[105] K. Morasch and D. Bahr, "The effects of hydrogen on deformation and cross slip in a BCC titanium alloy," *Scripta Materialia,* vol. 45, no. 7, pp. 839-845, 2001.

[106] A. Troiano, "The role of hydrogen and other interstitials in the mechanical behavior of metals," *Transactions of the American Society for Metals,* vol. 52, pp. 54-80, 1960.

[107] R. Oriani, "Hydrogen embrittlement of steels," *Annual Review of Materials Science,* vol. 8, pp. 327-357, 1978.

[108] W. Gerberich, P. Marsh and J. Hoehn, "Hydrogen Effects on Materials," in *TMS*, Warrendale, PA, 1996.

[109] V. Olden, C. Thaulow, R. Johnsen and E. Ostby, "Cohesive zone modeling of hydrogen-induced stress cracking in 25% Cr duplex stainless steel," *Scripta Materialia,* vol. 57, no. 7, pp. 615-618, 2007.

[110] M. Djukic, V. Sijacki Zeravcic, G. Bakic, A. Sedmak and B. Raijcic, "Hydrogen embrittlement of low carbon structural steel," *Procedia Materials Science,* vol. 3, pp. 1167-1172, 2014.

[111] W. Brocks, R. Falkenberg and I. Scheider, "Coupling aspects in the simulation of hydrogen-induced stress-corrosion cracking," *Procedia IUTEM,* vol. 3, pp. 11-24, 2012.

[112] R. Matsumoto, S. Taketomi, S. Matsumoto and N. Miyazaki, "Atomistic simulations of hydrogen embrittlement," *International Journal of Hydrogen Energy,* vol. 34, pp. 9576-9584, 2009.

[113] W. Gerberich, D. Stauffer and P. Sofronis, "A coexistent view of hydrogen effects on mechanical behavior of crystals: HELP and HEDE," in *2008 International Hydrogen Conference - Effects of Hydrogen on Materials*, Jackson, WY, 2009.

[114] S. Lawrence, B. Somerday, N. Moody and D. Bahr, "Grain boundary contributions to hydrogen-affected plasticity in Ni-201," *Journal of Materials,* vol. 66, no. 8, pp. 1383-1389, 2014.

[115] N. Takano, K. Kidani, Y. Hattori and F. Terasaki, "Fracture surface of hydrogen embrittlement in iron single crystals," *Scripta Metallurgica et Materialia,* vol. 29, pp. 75-80, 1993.

[116] J. Hirth, "Effects of hydrogen on the properties of iron and steel," *Metallurgical Transactions A,* vol. 11, pp. 861-890, 1980.

[117] P. Sofronis and I. Robertson, "Viable mechanisms of hydrogen embrittlement - a review," in *AIP Conference Proceedings*, 2006.

[118] J. Song and W. Curtin, "A nanoscale mechanism of hydrogen embrittlement in metals," *Acta Materialia,* vol. 59, pp. 1557-1569, 2011.

[119] I. Robertson, P. Sofronis, A. Nagao, M. Martin, S. Wang, D. Gross and K. Nygren, "Hydrogen embrittlement understood," *Metallurgical and Materials Transactions A,* vol. 46, pp. 2323-2341, 2015.

[120] N. Iyer and H. Pickering, "A mechanistic analysis of hydrogen entry into metals during cathodic hydrogen charging," *Scripta Metallurgica,* vol. 22, pp. 911-916, 1988.

[121] M. Nagumo, Fundamentals of hydrogen embrittlement, Springer, 2016.

[122] D. Escobar, C. Minambres, L. Duprez, K. Verbeken and M. Verhaege, "Internal and surface damage of multiphase steels and pure iron after electrochemical hydrogen charging," *Corrosion Science,* vol. 53, no. 10, pp. 3166-3176, 2011.

[123] C. Bishop and M. Stern, "A method for prevention of hydrogen embrittlement of tantalum in aqueous media," *Corrosion,* vol. 17, pp. 85-91, 1961.

[124] Y. Ro, S. Agnew, G. Bray and R. Gangloff, "Environment-exposure-dependent fatigue crack growth kinetics for Al-Cu-Mg/Li," *Materials Science and Engineering A,* Vols. 468-470, pp. 88-97, 2007.

[125] A. Kimura and H. Birnbaum, "Plastic softening by hydrogen plasma charging in pure iron," *Scripta Metallurgica,* vol. 21, pp. 53-57, 1987.

[126] R. Oriani, "The diffusion and trapping of hydrogen in steel," *Acta Metallurgica,* vol. 18, no. 1, pp. 147-157, 1970.

[127] A. Fischer-Cripps, Nanoindentation, New York: Springer, 2011.

[128] R. Cooper, "TriboIndenter user manual," Hysitron Incorporated, Minneapolis, 2007.

[129] D. Tabor, "The physical meaning of indentation and scratch hardness," *British Journal of Applied Physics,* vol. 7, no. 5, pp. 159-166, 1956.

[130] D. Tabor, "A simple theory of static and dynamic hardness," *Proceedings of the Royal Society of London A,* vol. 192, no. 1029, pp. 247-274, 1948.

[131] B. Poon, D. Rittel and G. Ravichandran, "An analysis of nanoindentation in elasto-plastic solids," *International Journal of Solids and Structures,* vol. 45, no. 25-26, pp. 6399-6415, 2008.

[132] M. De Guzman, G. Neubauer, P. Flinn and W. Nix, "The role of indentation depth on the measured hardness of materials," in *MRS Proceedings*, 1993.

[133] N. Stelmashenko, M. Walls, L. Brown and Y. Milman, "Microindentations on W and Mo oriented single crystals: An STM study," *Acta Metallurgica et Materialia,* vol. 41, no. 10, pp. 2855-2865, 1993.

[134] W. Gerberich, N. Tymiak, J. Grunlan, M. Horstemeyer and M. Baskers, "Interpretations of indentation size effects," *Journal of Applied Mechanics,* vol. 69, pp. 433-442, 2002.

[135] R. Cooper for Hysitron Incorporated, "Triboindenter user manual version 8.1.1," 2007.

[136] D. Williams and C. Carter, Transmission Electron Microscopy, A Textbook for Materials Science, Springer US, 2009.

[137] M. Uchic, D. Dimiduk, J. Florando and W. Nix, "Sample dimensions influence strength and crystal plasticity," *Science,* vol. 305, no. 5686, pp. 986-989, 2004.

[138] J. Greer, "Effective use of focused ion beam in investigation of fundamental mechanical properties at the sub-micron scale," *NSTI-Nanotech,* vol. 4, pp. 61-64, 2007.

[139] W. Kang and M. Saif, "A novel method for in situ uniaxial tests at the micro/nano scale - part I: Theory," *Journal of Microelectromechanical systems,* vol. 19, no. 6, pp. 1309-1321, 2010.

[140] International Atomic Energy Agency, "Neutron generators for analytical purposes," Vienna, 2012.

[141] D. Gillich, A. Kovanen and Y. Danon, "Deuterated target comparison for pyroelectric crystal D-D nuclear fusion experiments," *Journal of Nuclear Materials,* vol. 405, pp. 181-185, 2010.

[142] Y. Klochko, M. Lototsky, V. Solovey and Y. Shmal'ko, "Metal-hydride systems for hydrogen isotopes processing in physical-technical installations," *Hydrogen Materials Science and Chemistry of Metal Hydrides,* pp. 193-215, 2002.

[143] C. Monin, A. Ballanger, E. Sciora, A. Steinbrunn and G. Pelcot, "Characterization of deuteride titanium targets used in neutron generators," *Nuclear Instruments and Methods in Physics Research, Section A: Accelerators, Spectrometers, Detectors, and Associated Equipment,* pp. 453-493, 2000.

[144] P. Irving and C. Beevers, "Some observations on the deformation characteristics of titanium hydride," *Journal of Materials Science,* vol. 7, pp. 23-30, 1972.

[145] D. Setoyama, J. Matsunaga, H. Muta, M. Uno and S. Yamanaka, "Mechanical properties of titanium hydride," *Journal of Alloys and Compounds,* vol. 381, pp. 215-220, 2004.

[146] J. Xu, H. Cheung and S. Shi, "Mechanical properties of titanium hydride," *Journal of Alloys and Compounds,* vol. 436, pp. 82-85, 2007.

[147] R. Beck and W. Mueller, "Zirconium hyrides and hafnium hydrides," in *Metal Hydrides*, W. Mueller, J. Blackledge and G. Libowitz, Eds., New York, Academic Press, 1968.

[148] K. Barraclough and C. Beevers, "Some observations on the deformation characteristics of bulk polycrystalline zirconium hydrides," *Journal of Materials Science,* vol. 4, pp. 518-525, 1969.

[149] F. Nilson, "Ueber scandium, ein neues erdmetall," *Berichte der Deutschen Chemischen Gensellschaft,* vol. 12, no. 1, pp. 554-557, 1879.

[150] K. Gschneider, G. Melson, D. Youngblood and H. Schock, Scandium Its Occurence, Chemistry, Physics, Metallurgy, Biology, and Technology, C. Horovitz, Ed., New York: Academic Press, 2012.

[151] O. Naukim, Y. Savitskiy and V. Terekhova, *Phase diagram and properties of alloys of the aluminum-scandium system,* 1966.

[152] J. Murray, "The Al-Sc system," *Journal of Phase Equilibria,* vol. 19, no. 4, pp. 380-385, 1998.

[153] B. Mordike and T. Ebert, "Magnesium: Properties-applications-potential," *Materials Science and Engineering: A,* vol. 302, no. 1, pp. 37-45, 2001.

[154] V. Yeremenkko, V. Khorujaya and P. Martsenyuk, "The scandium-iridium phase diagram," *Journal of Alloys and Compounds,* vol. 204, pp. 83-87, 1994.

[155] E. Fisher and D. Dever, "Anomalous effects of temperature and impurities on the elastic moduli of scandium single crystals," *Proc. 7th Rare Earth Research Conference,* vol. 1, pp. 237-250, 1968.

[156] D. Geiselman, "The metallurgy of scandium," *Journal of the Less-Common Metals,* vol. 4, pp. 362-375, 1962.

[157] H. Brown, P. Armstrong and C. Kempter, "Elastic properties of polycrystalline Sc, Re, Ru and Pt-21 Ir," *Journal of the Less-Common Metals,* vol. 11, pp. 135-140, 1966.

[158] F. Spedding, D. Cress and B. Beaudry, "The resistivity of scandium single crystals," *Journal of the Less-Common Metals,* vol. 23, pp. 263-270, 1970.

[159] Q. Wu, J. Liang, J. Liu, W. Bing, X. Long and S. Luo, "Characteristics of microstructure and mechanical properties of Sc films as a function of substrate temperature," *Applied Surface Science,* vol. 258, no. 19, pp. 7421-7424, 2012.

[160] C. Saw, B. Beaudry and C. Stassis, "Location of deuterium in alpha-scandium," *Physical Review B,* vol. 27, p. 7013, 1983.

[161] Z. Fisk and D. Johnson, "Isotope effect in resistivity of scandium hydride," *Physics Letters A,* vol. 53, pp. 39-40, 1975.

[162] J. Beuth, "Cracking of Thin Bonded Films in Residual Tension," *International Journal of Solids and Structures,* vol. 29, pp. 1657-1675, 1992.

[163] J. Hutchinson and Z. Suo, "Mixed mode cracking in layered materials," *Advanced Applied Mechanics,* vol. 29, pp. 63-191, 1991.

[164] M. Ohring, The Materials Science of Thin Films, London: Academic Press Limited, 1992, pp. 419-420.

[165] N. Moody, E. Hintsala, C. Teresi, D. Adams, D. Kammler, E. Reedy Jr, N. Yang, M. Kennedy and W. Gerberich, "Deformation and fracture in scandium deuteride films and pillars," in *TMS 2013 Presentation*, San Antonio, 2013.

[166] W. Sounder and P. Hidnert, "Measurements on the thermal expansion of fused silica," *Scientific Papers of the Bureau of Standards,* vol. 21, pp. 1-25, 1925.

[167] J. Greer, W. Oliver and W. Nix, "Size dependence of mechanical properties of gold at the micron scale in the absense of strain gradients," *Acta Materialia,* vol. 53, pp. 1821-1830, 2005.

[168] D. Singh, N. Chawla, G. Tang and Y.-L. Shen, "Micropillar compression of AlSiC nanolaminates," *Acta Materialia,* vol. 58, no. 20, pp. 6628-6636, 2010.

[169] H. Fei, A. Abraham, N. Chawla and H. Jiang, "Evaluation of micro-pillar compression tests for accurate determination of elastic-plastic constitutive relations," *Journal of Applied Mechanics,* vol. 79, no. 6, p. 061011, 2012.

[170] S. Korte and W. Clegg, "Discussion of the dependence of the effect of size on the yield stress in hard materials studied by microcompression onf MgO," *Philosophical Magazine,* vol. 91, no. 7-9, pp. 1150-1162, 2011.

[171] T. Parthasarthy, S. Rao, D. Dimiduk, M. Uchic and D. Trinkle, "Contribution to size effect of yield strength from the stochastics of dislocation source lengths in finite samples," *Scripta Materialia,* vol. 56, no. 4, pp. 313-316, 2007.

[172] G. Cross, A. Schirmeisen, P. Grutter and U. Durig, "Plasticity, healing, and shakedown in sharp-asperity nanoindentation," *Nature Materials,* vol. 5, pp. 370-376, 2006.

[173] P. Schultz and C. Snow, "Mechanical properties of metal dihydrides," *Modelling Simulation in Materials Science and Engineering,* vol. 24, p. 035005, 2016.

[174] H.-J. Chang, J. Seguardo, J. Molina-Aldareguia, R. Soler and J. LLorca, "A 3D dislocation dynamics analysis of the size effect on the strength of [111] LiF micropillars at 300K and 600K," *Modelling and Simulation in Materials Science and Engineering,* vol. 24, p. 035009, 2016.

[175] W. Nix and S.-W. Lee, "Micro-pillar plasticity controlled by dislocation nucleation at surfaces," *Philosophical Magazine,* vol. 91, no. 7-9, pp. 1084-1096, 2011.

[176] H. Espinosa, S. Berbenni, M. Panico and K. Schwarz, "An interpretation of size-scale plasticity in geometrically confined systems," *Proceedings of the National Academy of Science,* vol. 102, no. 47, pp. 16933-16938, 2005.

[177] Z. Shan, R. Mishra, S. Syed Asif, O. Warren and A. Minor, "Mechanical annealing and source-limited deformation in submicrometre-diameter Ni crystals," *Nature Materials,* vol. 7, pp. 115-119, 2007.

[178] E. Camposilvan and M. Anglada, "Micropillar compression inside zirconia degraded layer," *Journal of the European Ceramic Society,* vol. 35, no. 14, pp. 4051-4058, 2015.

[179] E. Hoek, "Brittle fracture of rock," in *Rock Mechanics in Engineering Practice*, K. Stagg and O. Zienkiewicz, Eds., London, J. Wiley, 1968, pp. 99-124.

[180] NIST/SEMATECH, e-Handbook of Statistical Methods, NIST, 2013.

[181] W. Nelson, Applied Life Data Analysis, New York: Wiley-Blackwell, 2004.

[182] E. Tsalouchou, M. Cattell, J. Knowles, P. Pittayachawan and A. McDonald, "Fatigue and fracture properties of yttria partially stabilized zirconia crown systems," *Dental Materials,* vol. 24, pp. 308-318, 2008.

[183] R. Oakes Jr., "Specimen type and size effects on lithium hydride tensile strength distributions," Oak Ridge Y-12 Plant, Oak Ridge, TN, 1991.

[184] H. Tada, P. Paris and G. Irwin, in *The Stress Analysis of Cracks Handbook, 3rd edition*, ASME Press, 2000, pp. 410-414.

[185] M. Al-Chalabi and C. Huang, "Stress distribution within circular cylinders in compression," *International Journal of Rock Mechanics and Mining Sciences & Geomechanics Abstracts,* vol. 11, no. 2, pp. 45-56, 1974.

[186] S. Peng, "Stresses within elastic circular cylinders loaded uniaxially and triaxially," *International Journal of Rock Mechanics and Mining Sciences,* vol. 8, pp. 399-432, 1971.

[187] D. Broek, Elementary Engineering Fracture Mechanics, 4th ed., London: Kluwer Academic, 1991, p. 166.

[188] J. Corbett, P. Deak, C. Ortiz-Rodriguez and L. Snyder, "Embrittlement of materials: Si(H) as a model system," *Journal of Nuclear Materials,* vol. 169, pp. 179-184, 1989.

[189] B. Wilcox and G. Smith, "Intercrystalline fracture in hydrogen-charged nickel," *Acta Metallurgica,* vol. 13, no. 3, pp. 331-343, 1965.

[190] T. Boniszewski and G. Smith, "The influence of hydrogen on the plastic deformation, ductility, and fracture of nickel in tension," *Acta Metallurgica,* vol. 11, pp. 165-178, 1963.

[191] H. Izumi, R. Mukaiyama, N. Shishido and S. Kamiya, "Effect of hydrogen on the mechanical properties of silicon crystal surface," in *ASME 2013 International*

Technical Conference and Exhibition on Packaging and Integration of Electronic and Photonic Microsystems, Burlingame, CA, 2013.

[192] T. Zhang and P. Haasen, "The influence of ionized hydrogen on the brittle-to-ductile transition in silicon," *Philosophical Magazine A,* vol. 60, pp. 15-38, 1989.

[193] I. Yonenaga, "An overview of plasticity in Si crystals governed by dislocation motion," *Engineering Fracture Mechanics,* vol. 147, pp. 468-479, 2015.

[194] N. Kheradmand, J. Dake, A. Barnoush and H. Vehoff, "Novel methods for micromechanical examination of hydrogen and grain boundary effects on dislocations," *Philosophical Magazine,* vol. 92, no. 25-27, pp. 3216-3230, 2012.

[195] D. Dimiduk, M. Uchic and T. Parthasarathy, "Size-affected single-slip behavior of pure nickel microcrystals," *Acta Materialia,* vol. 53, no. 15, pp. 4065-4077, 2005.

[196] S. Bruemmer, R. Jones, M. Thomas and D. Baer, "Influence of sulfur, phosphorus, and antimony segregation on the intergranular hydrogen embrittlement of nickel," *Metallurgical Transactions A,* vol. 14, pp. 223-232, 1983.

[197] R. Latanision and H. Opperhauser, "The intergrangular embrittlement of nickel by hydrogen: the effect of grain boundary segregation," *Metallurgical Transactions,* vol. 5, pp. 483-492, 1974.

[198] J. Angelo, N. Moody and M. Baskes, "Trapping of hydrogen to lattice defects in nickel," *Modelling and Simulations in Materials Science and Engineering,* vol. 3, pp. 289-307, 1995.

[199] A. Tehranchi and W. Curtin, "Atomistic study of hydrogen embrittlement of grain boundaries in nickel: I. Fracture," *Journal of the Mechanics and Physics of Solids,* vol. 101, pp. 150-165, 2017.

[200] W. Van Arsdell and S. Brown, "Subcritical crack growth in silicon MEMS," *IEEE Journal of Microelectromechanical Systems,* vol. 8, no. 3, pp. 319-327, 1999.

[201] L. Pizzagalli and P. Beauchamp, "Dislocation motion in silicon: the shuffle-glide controversy revisited," *Philosophical Magazine Letters,* vol. 88, no. 6, pp. 421-427, 2008.

[202] J. Rabier, P. Cordier, T. Tondellier, J. Demenet and H. Garem, "Dislocation microstructures in Si plastically deformed at RT," *Journal of Physics: Condensed Matter,* vol. 12, pp. 10059-10064, 2000.

[203] J. Godet, P. Hirel, P. Brochard and L. Pizzagalli, "Dislocation nucleations from surface step in silicon: The glide set versus the shuffle set," *Physica Status Solidi A,* vol. 206, no. 8, pp. 1885-1891, 2009.

[204] L. Hansen, K. Stokbro, B. Lundqvist and K. Jacobsen, "Dynamics of partial dislocations in silicon," *Materials Science and Engineering B,* vol. 37, pp. 185-188, 1996.

[205] S. Kulkarni and W. Williams, "Dislocation velocities and electronic doping in silicon," *Journal of Applied Physics,* vol. 47, pp. 4318-4324, 1976.

[206] J. Rabier, P. Veyssiere and J. Demenet, "Plastic deformation of silicon at low temperature and the influence of doping," *Journal de Physique Colloques,* vol. 44, no. C4, pp. 243-253, 1983.

[207] E. Hintsala, Analytical and Experimental Nanomechanical Approaches to Understanding the Ductile-to-Brittle Transition, Ph.D. thesis, Dept. Mater. Sci., Univ. Minnesota, Minneapolis, MN, 2015.

[208] A. Sarkar and J. Chaktravartty, "Activation volume and density of mobile dislocations in plastically deforming Zr-1%Sn-1%Nb-0.1%Fe alloy," *Metallurgical and Materials Transactions A,* vol. 46, no. 12, pp. 5638-5643, 2015.

[209] L. Lu, T. Zhu, Y. Shen, M. Dao, K. Lu and S. Suresh, "Stress relaxation and the structure size-dependence of plastic deformation in nanotwinned copper," *Acta Materialia,* vol. 57, pp. 5165-5173, 2009.

[210] Y. Wang, A. Hamza and E. Ma, "Activation volume and density of mobile dislocations in plastically deforming nanocrystalline Ni," *Applied Physics Letters,* vol. 86, p. 241917, 2005.

[211] D. Caillard and J. Martin, Thermally Activated Mechanisms in Crystal Plasticity, New York: Elsevier, 2003.

[212] A. Elmustafa and D. Stone, "Nanoindentaiton and the indentaiton size effect: kinetics of deformation and strain gradient plasticity," *Journal of the Mechanics and Physics of Solids,* vol. 51, pp. 357-381, 2003.

[213] C. Huang, W. Hu and Q. Wang, "Strain-rate sensitivity, activation volume and mobile dislocation exhaustion rate in nanocrystalline Cu-11.1 at%Al alloy with low stacking fault energy," *Materials Science and Engineering A,* vol. 611, pp. 274-279, 2014.

[214] A. Orlova, J. Bonneville and P. Spatig, "Analogy between creep cycles and stress relaxation series for activation volume measurement," *Materials Science and Engineering A,* vol. 191, pp. 85-89, 1995.

[215] R. Othman, "A modified Eyring equation for modeling yield and flow stresses of metals at strain rates ranging from 10^-5 to 5*10^4 s^-1," *Advances in Materials Science and Engineering,* vol. 2015, p. 539625, 2015.

[216] J. Lim, H. Donahue and S. Kim, "Strain rate, temperature, and microstructure-dependence yield stress of poly(ethylene terephthalate)," *Macromolecular Chemistry and Physics,* vol. 204, no. 4., pp. 653-660, 2003.

[217] A. Clark, Advances in Cryogenic Engineering Materials, New York: Springer, 2013.

[218] V. Maier, K. Durst, J. Mueller, B. Backes, H. Hoppel and M. Goken, "Nanoindentation strain-rate jump tests for determining the local strain-rate sensitivity in nanocrystalline Ni and ultrafine-grained Al," *Journal of Materials Research,* vol. 26, no. 11, pp. 1421-1430, 2011.

[219] B. Lucas and W. Oliver, "Indentation power-law creep of hight purity indium," *Metallurgical and Materials Transactions A,* vol. 30, no. 3, pp. 601-610, 1999.

[220] J. Volkl and G. Alefeld, "Diffusion of hydrogen in metals," in *Hydrogen in Metals I*, New York, Springer-Verlag, 1978, pp. 321-348.

[221] Y. Ebisuzaki, W. Kass and M. O'Keeffe, "Diffusion and solubility of hydrogen in single crystals of nickel and nickel-vanadium alloy," *Journal of Chemical Physics,* vol. 46, no. 4, pp. 1378-1381, 1967.

[222] S. Pearton, J. Corbett and J. Borenstein, "Hydrogen diffusion in crystalline semiconductors," *Physica B,* vol. 170, pp. 85-97, 1991.

[223] C. Seager, R. Anderson and J. Panitz, "The diffusion of hydrogen in silicon and mechanisms for "unintentional" hydrogenation during ion beam processing," *Journal of Materials Research,* vol. 2, no. 1, pp. 96-106, 1987.

[224] Y. Kamiura, M. Yoneta and F. Hashimoto, "Hydrogen diffusivities below room temperature in silicon evaluated from the photoinduced dissociation of hydrogen-carbon complexes," *Applied Physics Letters,* vol. 59, no. 24, pp. 3165-3167, 1991.

[225] S. Bedard and L. Lewis, "Diffusion of hydrogen in crystalline silicon," *Physical Review B,* vol. 61, p. 9898, 2000.

[226] C. Nichols, D. Clarke and C. Van de Walle, "Properties of hydrogen in crystalline silicon under compression and tension," *Physical Review Letters,* vol. 63, no. 10, pp. 1090-1093, 1989.

[227] R. Asaro and S. Suresh, "Mechanistic models for the activation volume and rate sensitivity in metals with nanocrystalline grains and nano-scale twins," *Acta Materialia,* vol. 53, pp. 3369-3382, 2005.

[228] A. Almasri and G. Voiadjis, "Nano-indentation in FCC metals: experimental study," *Acta Mechanica,* vol. 209, pp. 1-9, 2010.

[229] O. Kum, "Orientation effects of elastic-plastic deformation at surfaces: nanoindentation of nickel single crystals," *Molecular Simulation,* vol. 31, no. 2-3, pp. 115-121, 2005.

[230] S.-P. Ju, C.-T. Wang, C.-H. Chien, J. Huang and S.-R. Jian, "The nanoindentation responses of nickel surfaces with different crystal orientations," *Molecular Simulation,* vol. 33, no. 11, pp. 905-917, 2007.

[231] H. Ledbetter and R. Reed, "Elastic properties of metals and alloys, I. iron, nickel, and iron-nickel alloys," *Journal of Physical and Chemical Reference Data,* vol. 2, pp. 531-617, 1973.

[232] W. Mankins and S. Lamb, "Nickel and nickel alloys," in *ASM Handbook*, ASM International, 1990, pp. 428-445.

[233] R. Arsenault, "Self-fracture of hydrogen-charged niobium," *Metallurgical Transactions A,* vol. 13, pp. 320-321, 1982.

[234] Z. Bazant, "Is no-tension design of concrete or rock structures always safe? - fracture analysis," *Journal of Structural Engineering,* vol. 122, no. 1, pp. 2-10, 1996.

[235] F. Torre, P. Spatig, R. Schaublin and M. Victoria, "Deformation behaviour and microstructure of nanocrystalline electrodeposited and high pressure torsioned nickel," *Acta Materialia,* vol. 53, no. 8, pp. 2337-2349, 2005.

[236] R. Rohde and C. Pitt, "Dislocation velocities in nickel single crystals," *Journal of Applied Physics,* vol. 38, pp. 876-879, 1967.

[237] B. Wilcox and G. Smith, "The Portvin-Le Chatelier effect in hydrogen charged nickel," *Acta Metallurgica,* vol. 12, pp. 371-376, 1964.

[238] M. Hopcroft, W. Nix and T. Kenny, "What is the Young's modulus of silicon," *Journal of Microelectromechnical Systems,* vol. 19, pp. 229-238, 2010.

[239] G. Pharr, W. Oliver and D. Clarke, "The mechanical behavior of silicon during small-scale indentation," *Journal of Electronic Materials,* vol. 19, pp. 881-887, 1990.

[240] Y. Katz, "External surfaces affected by free hydrogen in metastable austenitic stainless steels," *WIT Transactions on Engineering Sciences,* vol. 62, pp. 153-167, 2009.

[241] A. Gouldstone, H.-J. Koh, K.-Y. Zeng, A. Giannakopoulos and S. Suresh, "Discrete and continuous deformation during nanoindentation of thin films," *Acta Materialia,* vol. 48, no. 9, pp. 2277-2295, 2000.

[242] S. Syed Asif, K. Wahl and R. Colton, "The influence of oxide and adsorbates on the nanomechanical response of silicon surfaces," *Journal of Materials Research,* vol. 15, no. 2, pp. 546-553, 1999.

[243] S. Rashkeev, D. Fleetwood, R. Schrimpf and S. Pantelides, "Dual behavior of H+ at Si-SiO2 interfaces: Mobility versus trapping," *Applied Physics Letters,* vol. 81, no. 10, pp. 1839-1841, 2002.

[244] A. Korsunsky, M. Sebastiani and E. Bemporad, "Residual stress evaluation at the micrometer scale: Analysis of thin coatings by FIB milling and digital image correlation," *Surface and Coatings Technology,* vol. 205, no. 7, pp. 2393-2403, 2010.

[245] K. Kang, N. Yao, M. He and A. Evans, "A method for in situ measurement of the residual stress in thin films by using the focused ion beam," *Thin Solid Films,* vol. 443, no. 1-2, pp. 71-77, 2003.

[246] M. Rist, S. Jones and T. Slade, "Microcracking and shear fracture in ice," *Annals of Glaciology,* vol. 19, pp. 131-137, 1994.

[247] S.-I. Karato and P. Wu, "Rheology of the upper mantle, a synthesis," *Science,* vol. 260, no. 5109, pp. 771-778, 1993.

[248] W. Spitzig, "Effect of hydrostatic pressure on plastic-flow properties of iron single crystals," *Acta Metallurgica,* vol. 27, pp. 523-534, 1978.

[249] C. Sammis, J. Smith and G. Shubert, "A critical assessment of estimation methods for activation volume," *Journal of Geophysical Research,* vol. 88, no. B11, pp. 10707-10718, 1981.

[250] N. Johnson, F. Ponce, R. Street and R. Nemanich, "Defects in single-crystal silicon induced by hydrogenation," *Physical Review B,* vol. 35, no. 8, pp. 4166-4170, 1987.

[251] D. Caillard and J. Martin, Experimental characterization of dislocation mechanisms, New York: Pergamon, 2003, pp. 13-53.

[252] M. Cordill, N. Moody and W. Gerberich, "The role of dislocation walls for nanoindentation to shallow depths," *International Journal of Plasticity,* vol. 25, pp. 281-301, 2009.

[253] F. Campbell, Elements of Metallurgy and Engineering Alloys, Materials Park, OH: ASM International, 2008.

[254] P. Yang and J.-M. Tarascon, "Towards systems materials engineering," *Nature Materials,* vol. 11, pp. 560-563, 2012.

[255] C. Passchier and R. Trouw, Microtectonics, Berlin: Springer-Verlag, 2005.

Appendix 1: List of Publications

A. Mittal, D.-B. Zhang, C. Teresi, T. Dumitrica, and A.K. Mkhoyan, Routes to Identification of Intrinsic Twist in Helical MoS2 Nanotubes by Electron Diffraction and Annular Dark-Field Scanning Transmission Electron Microscopy Imaging, Physical Review B, 2011 84, 153401.

E. Hintsala, C. Teresi, A.J. Wagner, K.A. Mkhoyan, and W. Gerberich, Fracture transitions in iron: Strain rate and environmental effects, Journal of Materials Research, 2014, 29(14), pp. 1513-1521.

E. Hintsala, C. Teresi, and W.W. Gerberich, Linking nanoscales and dislocation shielding to the ductile-brittle transition of silicon, Metallurgical and Materials Transactions A, 2016, 47, pp.5839-5843.

C.S. Teresi, E. Hintsala, E.D. Reedy, Jr., D.P. Adams, D.R. Kammler, N.Y. Yang, N.R. Moody, and W.W. Gerberich, Size effects on deformation and fracture of scandium deuteride films, 2017, in submission.

C.S. Teresi and W.W. Gerberich, Silicon activation volumes for fracture as affected by hydrogen, 2017, in preparation.

Appendix 2: List of Presentations

C.S. Teresi, E. Hintsala, and W.W. Gerberich. Apparent activation volume of silicon: nanoindentation and micropillar compression, The Minerals, Metals, and Materials Society National Meeting, Nashville, TN, February 14-18, 2016.

C.S. Teresi, C. San Marchi, N. Moody, and W.W. Gerberich. Dislocation impact(s) on hydrogen embrittlement, International Hydrogen Conference, Moran, WY, September 11-14, 2016.

C. Teresi, E. Hintsala, D.P. Adams, N.Y. Yan, D. Kammler, M. Kennedy, N.R. Moody, and W.W. Gerberich, Size effects on deformation and fracture of scandium deuteride films, International Hydrogen Conference, Moran, WY, September 11-14, 2016.

C.S. Teresi, W.W. Gerberich, Silicon activation volumes for plasticity, Society of Experimental Mechanics, Indianapolis, IN, June 11-15, 2017.

Appendix 3: Copyright Permissions

Chapter 2: This chapter was partially reproduced with permission of Springer from Metallurgical and Materials Transactions A, Linking Nanoscales and Dislocation Shielding to the Ductile-Brittle Transition of Silicon, 47(12), 2016, pp. 5839-5843, E. Hintsala, C. Teresi, and W.W. Gerberich, Copyright 2016 Springer.

Figure 2.1 was reproduced was reproduced with permission of Springer from Microtectonics, Deformation Mechanisms, 2005, p. 33, C.W. Passchier and R.A.J. Trouw, Copyright 2005 Springer.

Figure 2.2 was reprinted with permission from Elsevier from Introduction to Dislocations, Fifth Edition, D. Hull and D.J. Bacon, Strength of Crystalline Solids, p. 214, Copyright 1984 Elsevier.

Figure 2.5 was reproduced with permission of Springer from Nanoindentation, Analysis Methods, 2004, p. 49, A.C. Fischer-Cripps, Copyright 2004 Springer.

Chapter 3: Figure 4.1 was reproduced with permission of Taylor and Francis from Philosophical Magazine Letters, Dislocation motion in silicon: the shuffle-glide controversy revisited, 88(6), 2008, p. 422, L. Pizzagalli and P. Beauchamp, Copyright 2008 Taylor and Francis.